Measurement of the electron energy distribution at AWAKE

Fearghus Robert Keeble
UCL

Submitted to UCL in fulfilment of the requirements for the award of the degree of
Doctor of Philosophy

Declaration

I, Fearghus Robert Keeble confirm that the work presented in this thesis is my own. Where information has been derived from other sources, I confirm that this has been indicated in the thesis.

Fearghus Keeble _____

Abstract

Much of the experimental data underpinning the Standard Model of particle physics has been collected at particle accelerators. The exponential increase in the energy of these machines has recently begun to slow, as the cost and scale of the projects reach historic levels. New accelerating technologies may offer a way to reverse this trend and provide smaller scale or higher energy accelerators.

One such novel acceleration method is proton-driven plasma wakefield acceleration and the AWAKE experiment at CERN has been conceived to provide proof of this new acceleration principle. A 400 GeV proton bunch is used to drive a wakefield in a 10 m column of plasma. Low energy electrons are injected into this wake and accelerated to high energies. This accelerated electron bunch is diagnosed with a magnetic spectrometer.

This spectrometer has been designed, installed and calibrated in order to provide measurements of the energy and charge of the accelerated electron bunches at AWAKE.

Impact statement

High energy accelerators have driven advances in particle physics for much of the last century, accruing numerous Nobel prizes and developing a special place in the public consciousness in the process. These machines are becoming ever larger and ever more costly, leading to growing uncertainty about their future. The work presented in this thesis focuses on proton-driven plasma wakefield acceleration, a novel technology which may be employed to reduce the size and cost of future colliders.

The central work of the thesis is characterised in two publications. One, published in Nuclear Instruments and Methods A (J. Bauche *et al.*, *NIM* A940, 103–108, 2019), describes the design and calibration of a magnetic spectrometer used to measure accelerated electron bunches at AWAKE, a proof-of-principle proton-driven plasma wakefield acceleration experiment. The work on this spectrometer was a collaboration between UCL, CERN and ESO. The other, published in Nature (AWAKE Collaboration, E. Adli *et al.*, *Nature* 561, 363–367, 2018) details the first electron acceleration results from AWAKE. This paper generated international interest from both the scientific and mainstream media. It is hoped that the success of AWAKE will lead to frontier colliders which would be infeasible without this new technology.

More broadly, results from AWAKE will influence the wider plasma wakefield acceleration community. Plasma wakefield acceleration is being investigated for use in compact synchrotron radiation sources and medical and defence applications. Consequently, the results presented here are expected to impact a wide variety of fields.

Acknowledgements

I would like to thank Matthew for his supervision and advice. I'd also like to acknowledge the help, influence and friendship of my colleagues and collaborators at UCL, CERN, ESO and Oxford.

In memory of P. J. K., who would have loved this

Contents

List of figures

List of tables

Chapter 1.

Introduction

The Standard Model (SM) of particle physics [1, 2] is arguably the most thoroughly tested scientific theory in history. The development, appraisal and success of this theory has only been possible thanks to the exponential increase in beam energies at particle accelerators over the latter half of the 20^{th} century. The most recent validation of the SM, the 2012 discovery of the Higgs boson by ATLAS (A Toroidal LHC Apparatus) and CMS (Compact Muon Solenoid) [3, 4], was achieved with the largest machine ever built: the LHC (Large Hadron Collider) [5].

This discovery marks the beginning, rather than the end, of Higgs physics, with only three [6–11] of the Higgs' hypothesised Yukawa couplings directly measured and its unique self-coupling yet to be observed [2]. To this end, and others, the LHC programme will continue into the late 2030s [12] but proposals for future frontier colliders are already numerous [13–16]. These proposals have two key commonalities: historic size and cost.

The scale of the proposed colliders, both linear and circular, may be motivated with physical reasoning. In circular colliders, charged particles of energy E are bent by magnetic fields of strength B according to the relation

$$E \propto B\rho \,, \tag{1.1}$$

where ρ is the bending radius of the particle. Therefore, energetic particles cannot be bent around arbitrarily small circles without an unfeasibly powerful magnet. An additional constraint on circular colliders comes from synchrotron radiation [17], which is emitted by accelerating particles. A particle traversing a circular collider is under a constant

state of acceleration and loses energy as

$$\frac{dE}{dt} \propto -\frac{\gamma^4}{\rho^2}\,, \tag{1.2}$$

where t is time and γ is the particle's Lorentz factor. These particles have an energy ϵ added by accelerating structures on each revolution. At some stage, the energy lost due to synchrotron radiation will equal the energy added by these structures, at which point the collider has reached its maximum possible energy. This maximum energy scales as

$$E_{\text{max}} \propto (\rho\epsilon)^{\frac{1}{4}}\,, \tag{1.3}$$

making a large increase in energy difficult without a much larger increase in the size or power consumption of the accelerator. The small mass of the electron compared to the proton makes this effect much more acute at lepton colliders than it is at hadron colliders.

The attritional effect of synchrotron radiation on electrons and positrons has motivated linear collider proposals [15, 16]. Linear colliders only minimally bend their particles and are instead limited by the strength of their accelerating structures. At modern colliders these structures are radio-frequency (RF) cavities which use time-varying electric fields to accelerate particles. The electric fields in non-cryogenic RF cavities are typically limited by the power which can be provided to them and the two linear collider manifestos tackle this problem in different ways. The international linear collider (ILC) proposes the use of superconducting RF cavities which have low energy losses. The compact linear collider (CLIC) instead advocates for the use of a drive beam to power normal-conducting cavities. The CLIC proposal offers higher accelerating gradients (approximately $100\,\text{MV}\,\text{m}^{-1}$) than the ILC (approximately $35\,\text{MV}\,\text{m}^{-1}$) because CLIC's non-cryogenic cavities are less affected by a more fundamental limitation of RF structures; cavity 'breakdown' [18]. This occurs when the electric field becomes sufficiently strong as to ionise electrons in the cavity's metallic walls, damaging the structure. Mitigation of breakdown is an area of active research [19, 20] but to achieve a true paradigm shift in frontier collider design, such as an order of magnitude decrease in the size of accelerating structures, attention has turned to circumvention of the problem instead. One such approach is to embrace the idea of cavity ionisation to an extreme degree and employ a plasma as the accelerating structure.

1.1. Plasma wakefield acceleration

The notion of particle acceleration using plasma has a long history, dating at least as far back as Veksler in 1956 [21]. Present interest, however, can largely be traced to 1979 when Tajima and Dawson proposed that plasma oscillations initiated by a high intensity laser pulse could be used to efficiently accelerate particles [22]. This oscillating structure is now commonly referred to as a plasma wakefield, the electric fields in which can exceed those in RF cavities by several orders of magnitude. With the advent of modern laser technology this proposal was quickly realised [23–25] and in 2004 a trio of seminal papers demonstrated the production of near-monoenergetic electron bunches through this so-called laser wakefield acceleration (LWFA) [26–28].

The concept of laser-driven wakefields was quickly followed by beam-driven plasma wakefield acceleration [29, 30]. In this proposal a high energy electron bunch passes through a plasma and the plasma electrons are repelled from its axis of propagation, leaving a region of positively charged ions, which move on much longer time scales to the electrons due to their mass. The positive charge of this region in turn acts on the expelled electrons, setting up an oscillating structure in the wake of the particle bunch. From an energy gain point of view, beam-driven experiments have proved the most successful, with the energy doubling of a 42 GeV electron beam in 85 cm of plasma at the Stanford Linear Accelerator Center [31] being a prime example.

The frequency of the plasma's oscillation, in both the laser-driven and beam-driven cases, is known as the plasma electron frequency (or plasma frequency) ω_{pe} and is given by

$$\omega_{\mathrm{pe}} = \sqrt{\frac{e^2 n_{\mathrm{pe}}}{\varepsilon_0 m_e}}\,, \tag{1.4}$$

where e is the electron's charge, n_{pe} is the plasma electron density, m_e is the electron mass and ε_0 is the vacuum permittivity. The characteristic strength of the electric fields in a plasma is given by the so-called 'wave-breaking' field [32, 33]

$$\mathscr{E}_{\mathrm{wb}} = \frac{m_e c\, \omega_{\mathrm{pe}}}{e}\,, \tag{1.5}$$

where c is the speed of light. Therefore, $\mathrm{GV\,m^{-1}}$ accelerating gradients can be obtained with plasma densities of $\mathcal{O}(10^{14}\,\mathrm{cm^{-3}})$ and higher. At the plasma density of $2.7 \times 10^{17}\,\mathrm{cm^{-3}}$ used in Ref. [31] the wave-breaking field corresponds to approximately

$50\,\mathrm{GV\,m^{-1}}$, dwarfing the proposed RF cavity gradients of the ILC and CLIC discussed above.

Accelerating gradient, however, is not the only parameter by which colliders may be compared. The physics reach of a collider is determined as much by its luminosity as it is by its energy, and in this respect wakefield acceleration, at present, falls down. Indeed, the high energies of contemporary and future colliders drive the need for increased luminosity, in order to counteract the fact that annihilation cross sections, in general, scale with the inverse square of the centre-of-mass energy. Luminosity is directly proportional to both the repetition frequency of the collider and the charge of the colliding beams. The high intensity laser pulses used to produce electron GeV bunches in LWFA have a repetition rate of 1–10 Hz [34], which falls considerably short of the rates proposed for the ILC and CLIC. Furthermore, in both laser-driven and electron beam-driven acceleration the driver energy constrains the total energy of the bunches produced in the wakefield. An ILC electron bunch, for example, with 2×10^{10} particles at 250 GeV has a total energy of 0.8 kJ. This is well beyond the energies achievable by both high intensity laser systems and available electron drive bunches, meaning that either the bunch charge or bunch energy will be limited. This shortcoming motivates the idea of staged acceleration [35,36] which presents a significant technical challenge, though research in this area is already producing promising results [37]. A compelling alternative exists, however; the use of a proton driver.

1.2. Proton-driven plasma wakefield acceleration

The total energy of an LHC proton bunch is approximately 130 kJ; more than sufficient to produce an ILC-type electron bunch given an appropriate transformer. In proton-driven plasma wakefield acceleration [38] this transformer is the plasma and acceleration of a witness beam to very high energies can occur in a single stage. A prerequisite for this technique to be effective, however, is a short proton bunch. Short in this case means shorter than the plasma wavelength $\lambda_{\mathrm{pe}} = 2\pi c/\omega_{\mathrm{pe}}$. A plasma density of $\mathcal{O}(10^{14}\,\mathrm{cm^{-3}})$, as quoted above, corresponds to a plasma wavelength of $\mathcal{O}(1\,\mathrm{mm})$; considerably shorter than bunches at the LHC, for example, which have a root mean square (r.m.s.) length of about 8 cm. Long proton bunches of this kind cannot naturally drive strong wakefields and in Ref. [38] a bunch compression scheme was envisaged which reduced the length of

the proton bunch to 100 μm at the expense of increasing the relative energy spread from 10^{-4} to approximately 10^{-1}.

Proton bunch compression of this kind is difficult, however, likely requiring 100 s of metres of space for beam optics [39]. To overcome this limitation, the use of proton bunch self-modulation was proposed [40, 41]. This concept, which is inspired by laser pulse modulation in LWFA [42], proposes exploiting the interaction of the nascent plasma wakefield with the long proton bunch to modulate it into a series of microbunches. Protons in the bunch are periodically focused to and defocused from the axis by the action of the wakefield. The focused protons, the microbunches, will naturally be spaced according to the plasma frequency and resonantly drive the wakefield to increasingly high amplitudes as the modulation progresses. Self modulation is not the only particle–plasma interaction which can affect the proton bunch, however, and other effects such as the so-called 'hosing instability' [43, 44] can have a destructive effect on the bunch before self-modulation is achieved. The hosing instability results in the breaking up of the drive beam and is initiated by transverse asymmetries in spatial or momentum distributions of the beam or plasma. These effects can be negated by initiating the wakefield with sufficiently strong initial perturbation. This can be achieved with a high intensity laser pulse [45] or a proton bunch with a sharp density ramp [46]. Bunch shaping in this manner is difficult but an effective sharp bunch profile can be achieved by copropagating the ionisation front, which forms the plasma, with an appropriate part of the proton bunch. That is, the first part of the proton bunch propagates through a neutral gas while the fraction behind the laser pulse propagates through a plasma, seeding a strong initial wakefield, becoming self-modulated and driving the wakefield to higher amplitudes in the process. This method of seeding the wakefield has been shown in simulation to be sufficient to suppress hosing instabilities and allow the self-modulation to saturate [47], opening the door to an experimental verification of proton-driven plasma wakefield acceleration.

1.3. Thesis outline

This thesis details the work carried out by the author as a member of the AWAKE (Advanced Wakefield Experiment) collaboration between September 2015 and March 2019. The work centred around the development, installation and calibration of a magnetic spectrometer and the analysis of the first physics results produced with it. The structure of the remainder of the thesis is as follows:

Chapter 2 presents an overview of the AWAKE experiment, some of its previous physics results and its place within the wider CERN infrastructure.

Chapter 3 details the physics underlying the action of a magnetic spectrometer and describes the steps taken to characterise the spectrometer at AWAKE.

Chapter 4 presents the full design of the AWAKE electron spectrometer.

Chapter 5 describes the steps taken to calibrate and characterise the spectrometer.

Chapter 6 presents the first electron acceleration results from AWAKE.

Chapter 7 examines a proposed application of proton-driven plasma wakefield acceleration to high energy physics.

Chapter 8 concludes the thesis, summarising the work and presenting an outlook for future progress.

Chapter 2.

The AWAKE experiment at CERN

This thesis presents electron acceleration results from AWAKE, a proof-of-principle proton-driven plasma wakefield experiment at CERN. This chapter provides an overview of the experiment. Section 2.1 presents AWAKE's place within the CERN accelerator complex. Section 2.2 provides an overview of the design and operation of the experiment. Some key AWAKE results are discussed in Section 2.3 and an overview of the experimental setup for the results presented in this thesis is described in Section 2.4.

2.1. AWAKE at CERN

Plasma wakefields at AWAKE are driven by 400 GeV proton bunches from the Super Proton Synchotron (SPS). An overview of the CERN accelerator complex, including AWAKE and the SPS, is shown in Figure 2.1. Proton bunch production begins when hydrogen gas is ionised using an electric field. The protons from this gas are accelerated to 50 MeV using LINAC 2. The Proton Synchrotron Booster and the Proton Synchrotron then accelerate the protons to 1.4 GeV and 25 GeV, respectively [5]. Protons are transferred from the PS to the SPS where they are accelerated to 400 GeV for AWAKE.

The AWAKE experiment occupies a tunnel to the east of the SPS originally built for the CERN Neutrinos to Gran Sasso (CNGS) experiment. The broad layout of the experiment is shown in Figure 2.2. Protons are extracted via the TT40 and TT41 transfer lines and arrive at AWAKE. The protons copropagate with an ionising laser pulse which creates a plasma in a 10 m column of rubidium vapour. The protons drive a strong wakefield in the plasma, which in turn modulates the bunch longitudinally into a series of high density microbunches. These microbunches act resonantly, increasing the strength of

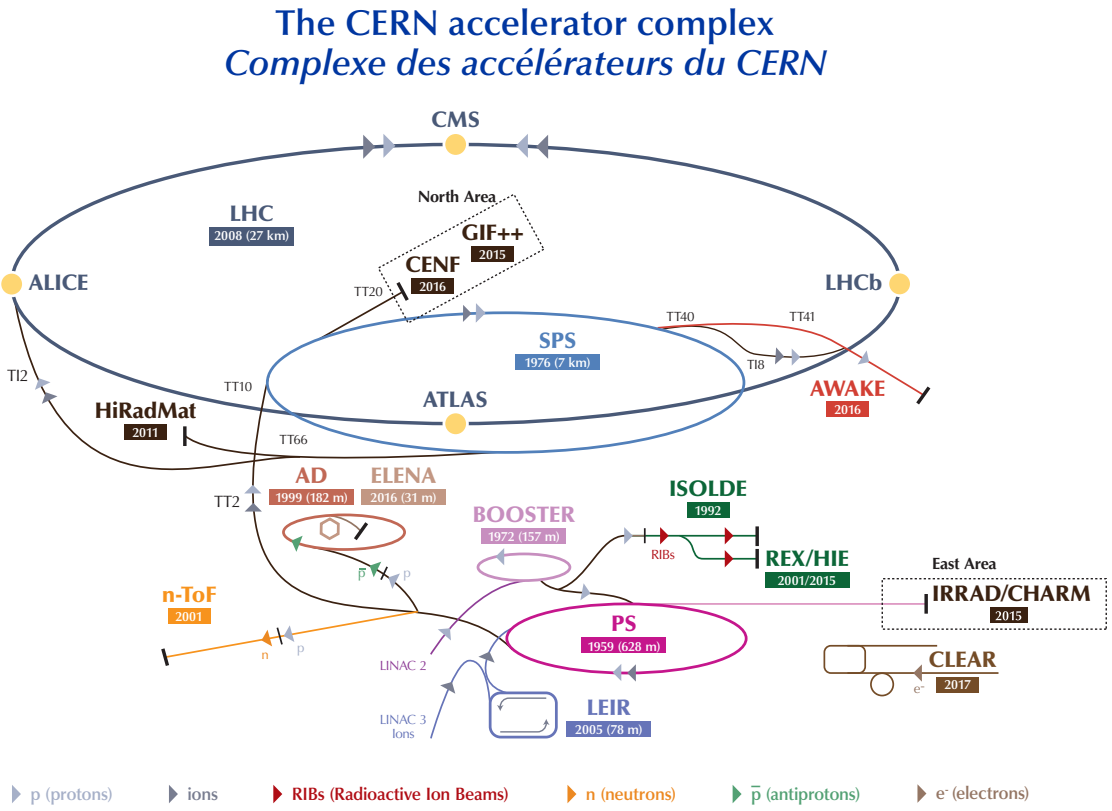

Figure 2.1.: Overview of the CERN accelerator complex, August 2018 [48]. The AWAKE experiment occupies a tunnel to the east of the SPS.

the wakefield. An electron bunch is injected into this wakefield, trapped and accelerated to high energies. The protons are dumped into the CNGS target while the electrons are dispersed and dumped into the air as part of their diagnosis. Proton bunch extraction occurs approximately once every 30 seconds and the bunches have a typical population of 3×10^{11} protons.

2.2. The AWAKE experiment

AWAKE is a three beam experiment, with each acceleration event using proton and electron bunches as well as a laser pulse. These three beamlines, as well as the various

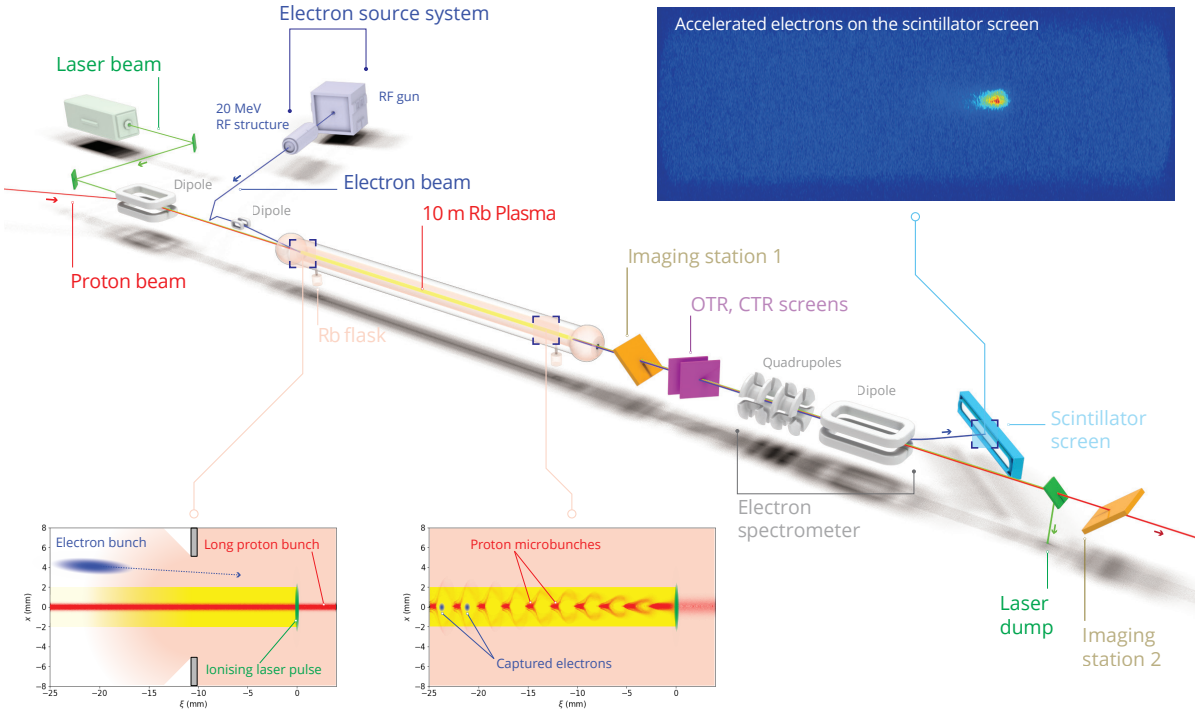

Figure 2.2.: The layout of the AWAKE experiment. The proton bunch and laser pulse propagate from left to right across the image, through a 10 m column of rubidium vapour. This laser pulse (green, bottom images) singly ionises the rubidium (Rb) to form a plasma (yellow) which then interacts with the proton bunch (red, bottom left image). This interaction modulates the long proton bunch into a series of microbunches (bottom right image) which drive a strong wakefield in the plasma. Electrons (blue), propagate a short distance behind the laser pulse and are injected into the wakefield by crossing at an angle. Some of these electrons are captured in the wakefield and accelerated to high energies.

Parameter	Baseline	Range
Proton energy	400 GeV	-
Proton energy spread	0.035%	-
Protons per bunch	3×10^{11}	$1.0–3.5 \times 10^{11}$
Proton bunch radius	0.2 mm	-
Proton bunch length	400 ps	-
Proton bunch normalised emittance	3.5×10^{-6} m rad	-
Electron energy	16 MeV	10–20 MeV
Electron energy spread	0.5%	-
Electron bunch charge	200 pC	100–1000 pC
Electron bunch radius	0.25 mm	0.25–1 mm
Electron bunch length	4 ps	0.3–10 ps
Electron bunch normalised emittance	2×10^{-6} m rad	$0.5–5 \times 10^{-6}$ m rad
Laser pulse central wavelength	780 nm	-
Laser pulse bandwidth	5 nm	-
Laser pulse length	120 fs	-
Laser pulse energy	450 mJ	-
Laser pulse size at waist	1 mm	-
Plasma electron density	7×10^{14} cm^{-3}	$1–10 \times 10^{14}$ cm^{-3}
Plasma electron frequency	237 GHz	90–284 GHz
Plasma electron wavelength	1.3 mm	3.3–1.1 mm

Table 2.1.: AWAKE baseline beam and plasma parameters [50–52].

diagnostics within the AWAKE tunnels, are shown in Figure 2.3. A number of relevant beam and plasma parameters for AWAKE are listed in Table 2.1.

The ionising laser pulse is produced by a Ti:Sapphire based laser system in TSG40 [53]. The compressed pulse length is 120 fs with an energy that can be varied from a few mJ up to 450 mJ and a central wavelength of 780 nm. This laser pulse is merged with the proton beam via TT42 using a mirror positioned close to the axis of the proton beam. The merging point is 22 m upstream of the plasma cell entrance and the beam width (full width at half-maximum, FWHM) is approximately 10 mm at this point, with the exact value depending on the focusing scheme. The pulse is focused down to a width of approximately 1 mm at its waist, the location of which can be varied to anywhere within the 10 m length of the plasma cell. The long distance between the merging mirror and

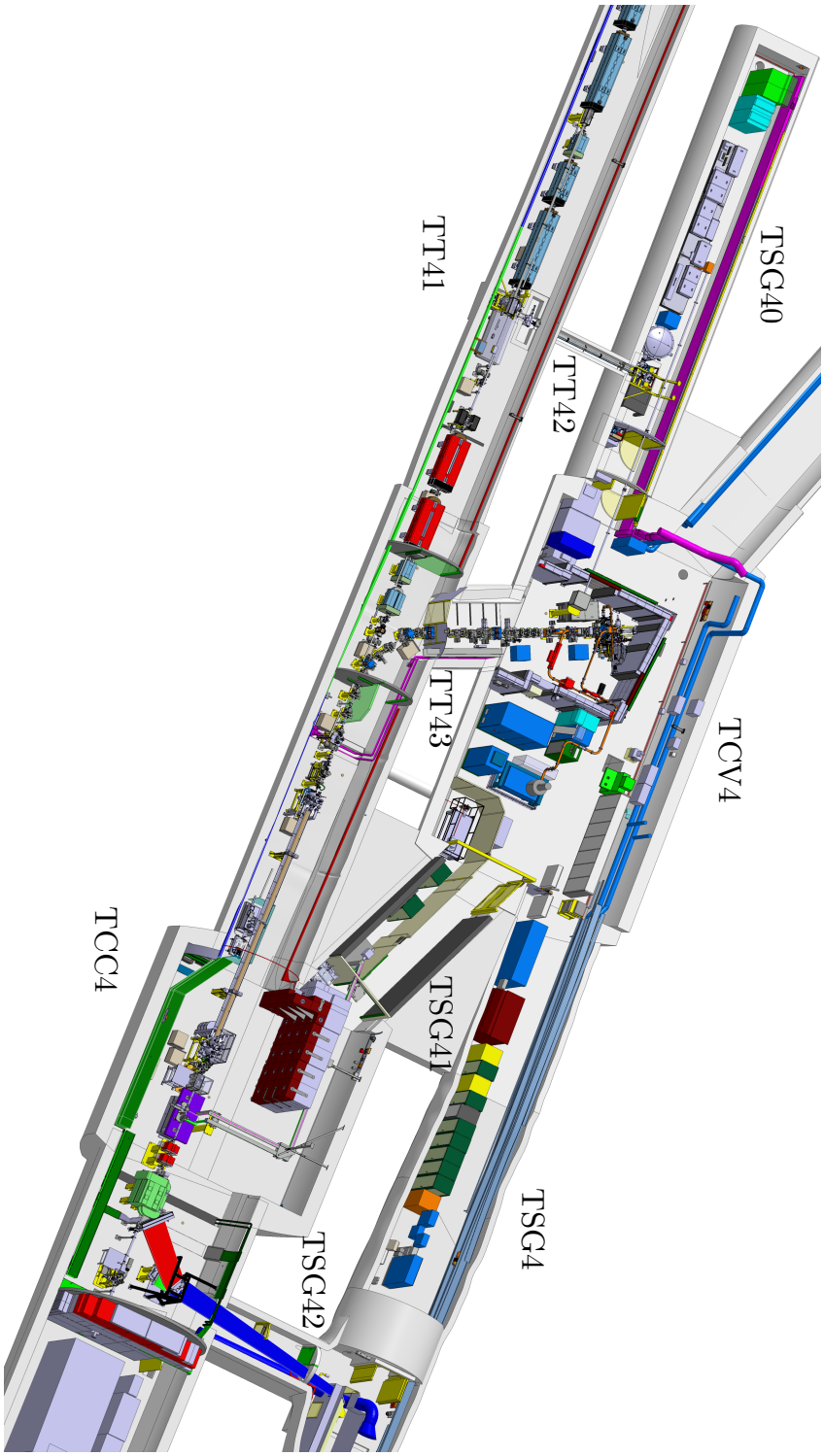

Figure 2.3.: Model of the AWAKE tunnels [49]. Protons are extracted from the SPS and arrive at AWAKE via TT41 (left side for landscape view). The protons pass through the TCC4 (lower right) and are dumped into a target. Low energy electron bunches are generated in TCV4 (centre) and propagate to TCC4 via TT43 and TT41. The laser pulses which ionise the plasma and produce the electron bunch are both generated by the AWAKE Ti:Sapphire laser in TSG40. The ionisation pulse is merged with the SPS proton beam via TT42 and co-propagates along the TT41 beamline.

the plasma cell contributes to a significant shot-to-shot spatial jitter in the laser pulse. The effect of this is mitigated, however, by the large transverse size of the laser pulse compared to the proton bunch.

The electron bunch also originates in TSG40 [54], in that it is produced using a frequency tripled UV pulse from the AWAKE laser. This pulse is transported to TCV4 where it is incident upon a Cs_2Te photocathode, producing a low energy electron bunch. This electron bunch is accelerated to 5–6 MeV through a 2.5 cell RF cavity. To reduce radiation in the area this electron source and its beamline are behind shielding walls. Outside the walls is a kylstron which powers the initial RF cavity and a 1 m long 30 cell RF booster, which further accelerates the electrons to their nominal injection energy of 15–20 MeV. After the booster, a series of quadrupoles and correcting magnets transport the bunch up the sloped TT43 tunnel and merge it with the common beamline in TT41. Alternatively, before TT43 the bunch can be sent to a Faraday cup to measure its charge. Electron bunches at AWAKE have a typical charge of $\mathcal{O}(100\,\mathrm{pC})$, which can be tuned by varying the intensity of the UV pulse. A bunch emittance measurement is possible before the booster using a pepper pot system with an insertable masked screen [55].

The AWAKE vapour source [56] is located in TCC4. The vapour source consists of a 10 m long 40 mm diameter vacuum tube terminated at each end by a large expansion volume. The system is filled with rubidium (Rb) vapour from two heated flasks near each end of the tube. The vacuum tube is surrounded by a 70 mm diameter heat exchanger which circulates an inert fluid (Galden HT 270) to ensure a uniform vapour temperature with $\delta T/T < 0.25\%$ [50]. Rubidium has a low ionisation potential of 4.2 eV for its first electron making it easier to ionise than elements which are gaseous at room temperature. This low first ionisation potential combined with the relatively high potential for the second electron (27.3 eV) ensures that the first electron will be fully ionised by the laser pulse while negligible secondary ionisation will occur, giving a plasma electron density equal to the Rb density. Control of the Rb temperature is, therefore, equal to control of the plasma density. A further advantage of using Rb vapour is the relatively high mass of the atoms, which helps to minimise the ion motion that could otherwise have a destructive effect on the wakefield [57]. The AWAKE plasma densities (see Table 2.1) are generated with Rb vapour held between 150°C and 230°C. The positioning of the Rb flasks near the ends of vacuum tube ensure that there is no net flow along the main length of the tube, which is also important to ensure temperature uniformity. Once the vacuum tube is filled, the flow of Rb occurs only over the short (few centimetres) path from the flasks to the expansion volumes, where it condenses onto the walls which are

held below 39°C (the condensation temperature of Rb). To prevent rapid loss of Rb, the flow to the expansion volume is limited by 10 mm diameter apertures at each end of the vacuum tube. The expansion volumes are separated from the main beamline by mechanical shutters. These shutters are closed when frequent extraction events are not occurring, reducing the condensation of Rb onto the vacuum elements upstream and downstream of the vapour source.

The Rb density is continuously monitored by a diagnostic incorporating two Mach-Zehnder interferometers [58]. Coherent white light from one arm of each interferometer propagates across the transverse axis of the vapour source's vacuum tube, through viewports close to each of the Rb flasks. Rubidium atoms have two transition lines in the optical range at 780.03 nm and 794.76 nm and these generate a change in the index of refraction for light in the vicinity of these wavelengths, the magnitude of which is dependent on the density of the Rb vapour. This change in refractive index affects the interference pattern observed on two spectrographs (one for each viewport) and the Rb density may be inferred from this disturbance. The measurement of the Rb is taken as having a one-to-one equivalence to the plasma electron density since the atoms are singly ionised (see above). The two interferometers can be used to measure the density difference from one end of the plasma cell to the other, which can be set by changing the relative temperatures of the Rb flasks. Plasma density gradients have been shown in simulations to increase the maximum energy attained by accelerated electrons [59].

2.3. Self-modulation results from AWAKE

Prior to the experimental results presented in this thesis, AWAKE achieved the first of its experimental goals [60]; to establish self-modulation of the proton bunch via a plasma wakefield. The modulation was verified by direct [61] and indirect [62] detection methods.

Direct evidence of self-modulation is established with a streak camera diagnostic [63]. The experimental setup for the camera is shown in Figure 2.4. The streak camera creates a time resolved image [64] of the modulated proton bunch using optical transition radiation (OTR) [65]. This radiation is emitted due to the change in the permittivity at the boundary between the vacuum and the silicon foil. The radiation mimics the temporal structure of the microbunches, arriving at the streak camera as a series of pulses. In the camera these pulses are converted into electrons via a photocathode. The electrons then pass through a time-varying electric field, which deflects the electrons

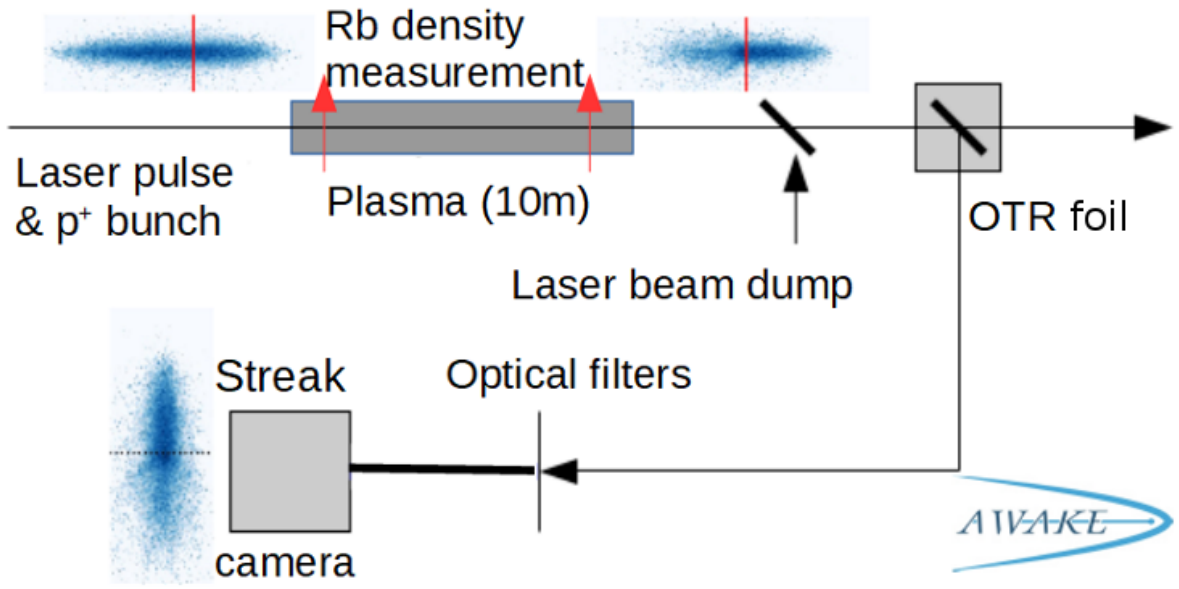

Figure 2.4.: Setup of the streak camera used to measure self-modulation at AWAKE [61]. The proton bunch (blue) propagates through the rubidium vapour. The laser pulse (red) ionises the vapour forming a plasma which affects the rear half of the proton bunch, modulating it into a series of microbunches. After the plasma the laser pulse is dumped and the protons pass through a 0.28 mm silicon wafer (foil) generating optical transition radiation (OTR). This light is imaged using a streak camera which creates a time resolved image. Optical filtering is used to improve the image quality.

along a given axis, converting the temporal spread of the pulses to a spatial spread. The electrons are then incident upon a phosphor screen, emitting light which is captured by a charge-coupled device (CCD). The result is a longitudinal and transverse beam profile, integrated over one of the transverse axes.

Streak camera images at low and high densities are shown in Figure 2.5. The horizontal projections of the central regions show a clear modulation pattern with a characteristic frequency. This frequency is evident in the spectrum obtained by a discrete Fourier transform (DFT) of each projection. The peaks in the interpolated DFTs in Figure 2.5 occur at frequencies of 138 ± 4 GHz and 238 ± 4 GHz, which are in agreement with the plasma frequencies inferred from the Rb densities: 141 GHz and 237 GHz respectively.

Indirect evidence of self-modulation is established with beam TVs (BTVs, labelled 'imaging station's in Figure 2.2) [66]. A BTV consists of a camera imaging a scintillating screen which is inserted into the beamline. BTVs effectively provide a measurement of the transverse distribution of the bunch integrated over its longitudinal (or temporal) axis. As discussed in Chapter 1, one of the effects of self-modulation is to reduce the

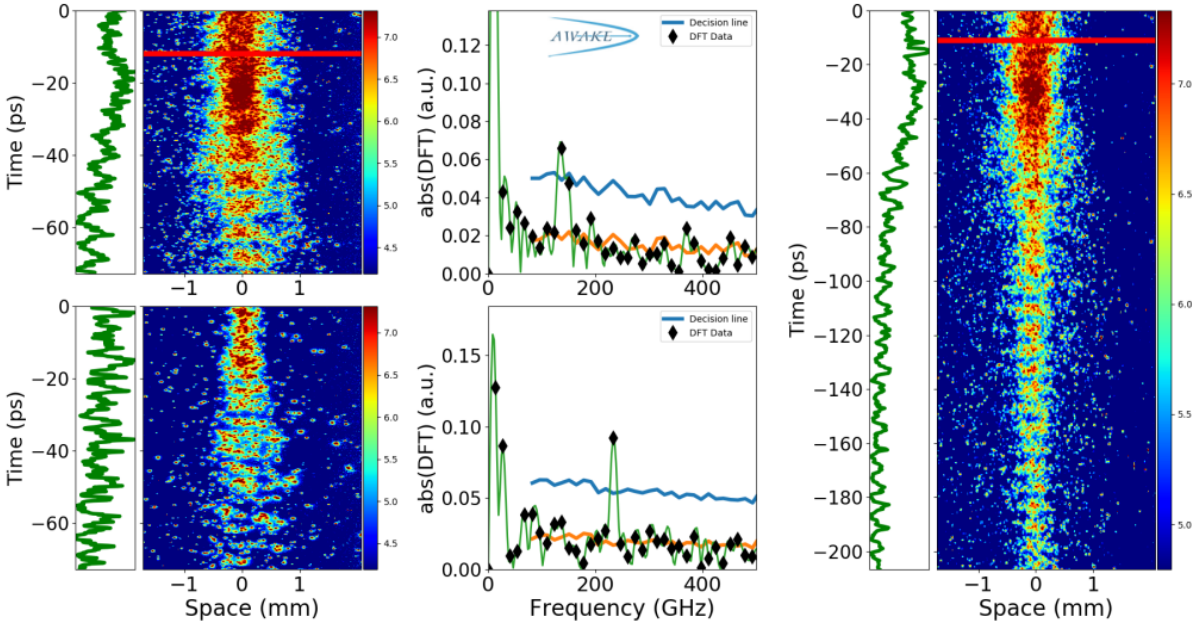

Figure 2.5.: Streak camera image of proton bunch self-modulation at AWAKE [61]. The modulation is shown at a low plasma density (top left, $n_{\mathrm{pe}} = 2.5 \times 10^{14}\,\mathrm{cm}^{-3}$) and a high plasma density (bottom left, $n_{\mathrm{pe}} = 7 \times 10^{14}\,\mathrm{cm}^{-3}$). The horizontal projections of the central portions (−0.4–0.6 mm) of the images are shown on the left side of each streak image. In the low density image, the horizontal red line indicates the position of the ionising laser pulse while the high density image shows the bunch approximately 10 ps after the laser pulse. The Fourier spectra of the image profiles are shown (black dots) in the two central plots. The green line in each plot gives the interpolated spectrum while the orange and blue lines respectively show a background image spectra and the cutoff level for determining whether self-modulation has occurred. In each case the peak in the spectrum occurs at the plasma frequency. The image on the right shows a longer time window at low density ($n_{\mathrm{pe}} = 2.2 \times 10^{14}\,\mathrm{cm}^{-3}$), where the full trail of microbunches is clear.

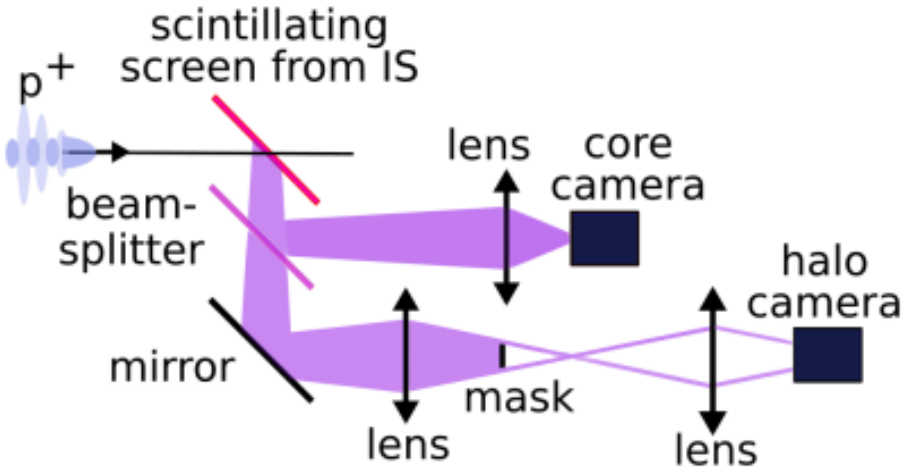

Figure 2.6.: Setup of a BTV (imaging station, IS) used to detect evidence of self-modulation [66]. The halo camera blocks the part of the image containing the beams core to provide sufficient dynamic range to properly measure the proton halo.

overall proton density on axis by 'blowing out' the non-microbunched protons transversely. This change in the bunch's transverse distribution can be measured by the two BTVs downstream of the plasma cell. The two screen measurement can be used to infer the transverse defocusing strength of the wakefield. The linear response of the BTV's camera and scintillating screens necessitates a special setup to measure the transverse tails of the bunch (the 'halo'), which would otherwise provide an insufficient signal relative to the bunch's core. This setup, shown in Figure 2.6, incorporates a beam splitter and image mask to provide a simultaneous measurement of the bunch's halo and core.

Images and results acquired with this setup are show in Figure 2.7. The figure shows core and halo images from events with and without an ionising laser pulse. The blowout of the protons is particularly clear on then halo camera. Projections of the images show that the modulated bunch has a reduced density in the core but increased density outside this region.

The projections in Figure 2.7 are used to estimate the maximum radius of the defocused protons. This radius is in turn used to estimate the average amplitude of the transverse fields in the plasma. Given well motivated assumptions about the point at which the protons exit the wakefield transversely, these fields are found to be in excess of $300\,\mathrm{MV\,m^{-1}}$ at an Rb density of $7.7 \times 10^{14}\,\mathrm{cm^{-3}}$ [66].

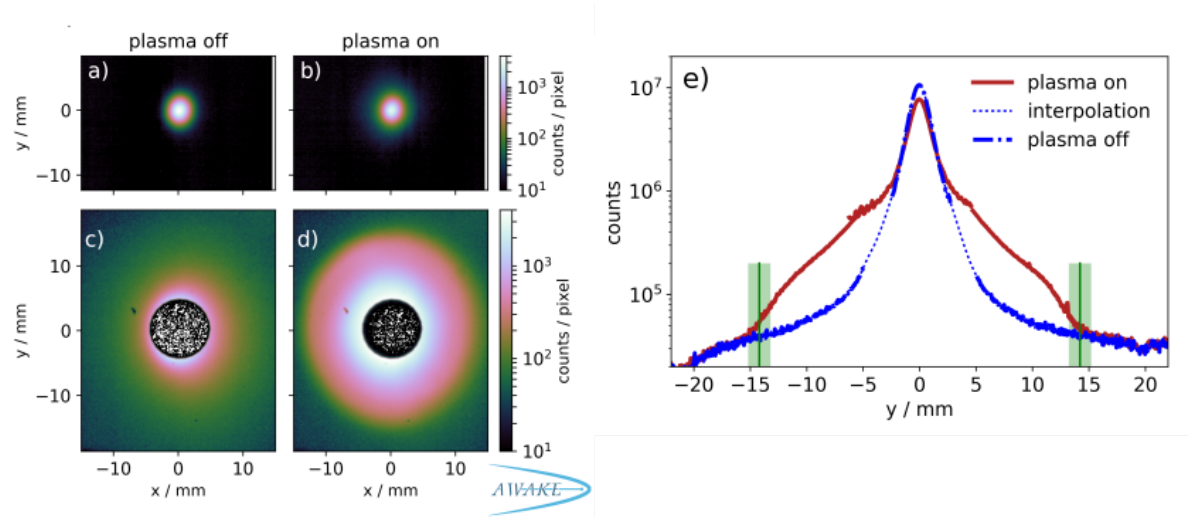

Figure 2.7.: Core and halo camera results with and without a plasma wakefield [66]. The events both occur at a rubidium vapour density of $7.7 \times 10^{14}\,\mathrm{cm}^{-3}$. Projections of the images are given in the plot on the right. The green bars indicate the maximum radius of the defocused protons.

2.4. Electron acceleration at AWAKE

This thesis details the first electron acceleration results from AWAKE. The experimental parameters used for these results differ from some of the baseline parameters discussed above. This section elaborates on the experimental setup for the May 2018 run when acceleration was first detected [67]. The corresponding acceleration results are presented in Chapter 6.

Electron bunches for injection are produced with a bunch charge of $656 \pm 14\,\mathrm{pC}$ and accelerated to $18.84 \pm 0.05\,\mathrm{MeV}$. These electron bunches trail the ionising laser pulse by a delay of 200 ps and enter the vapour source with a small vertical offset with respect to the proton bunch. The bunch's trajectory is angled downwards, crossing the axis of the protons approximately 2 m into the vapour source at an angle of 1.2–2 mrad. This so-called 'off-axis injection' has been shown in simulations to result in better electron capture and acceleration in the wakefield compared to collinear injection [52]. The electron bunch is focused close to the entrance aperture of the vapour source (the exact position varies over the dataset) and has a normalised emittance of $11\text{–}14 \times 10^{-6}\,\mathrm{m\,rad}$; considerably higher than the baseline value. This emittance was reduced after the May run through further commissioning and characterisation of the electron line.

During electron acceleration events, all beam instrumentation screens upstream of the spectrometer (OTR, CTR, BTVs) are removed from the beamline, as the proton bunch generates a significant radiation background when interacting with these elements. The ionising laser pulse is dumped downstream of the spectrometer and the self-modulation halo is monitored using the downstream BTV. The quality of the self-modulation is established using the streak camera before electron injection acceleration events begin.

All the experimental parameters are subject to variation during running. In some cases this variation is negligible (such as the proton bunch energy) and in other cases it is not (such as the proton bunch population). In addition to this, a number of parameters are deliberately varied over the dataset, including but not limited to: the focal point of the electron bunch, the ionising laser pulse energy, the electron bunch trajectory, the plasma density and the electron bunch delay. All these parameters are recorded and cuts may be made on event data to mitigate the possible effects of the variations. Treatment of the intentional and natural variation of the AWAKE parameters is discussed in connection with the plasma density gradient analysis of Section 6.2.3.

Chapter 3.

Spectrometry

Central to measuring the energy distribution of the accelerated electrons is defining the spectrometer's position–energy conversion function. This function relates the position of the electrons in the plane of the scintillator to their energy. It depends on the strength and size of the bending dipole and on the position of the scintillator relative to this dipole. In Section 3.1 and Section 3.2 this function will be derived analytically under the assumption of a uniform field contained entirely within the magnet's pole. The results of a set of BDSIM [68] simulations using magnetic field maps corresponding to the real magnet used in the spectrometer are presented in Section 3.3. The two results will be compared and combined to approximate the position–energy relationship for special cases of interest where no field map is available.

3.1. The Lorentz force

The functioning of a magnetic spectrometer relies on the Lorentz force. For a singly negatively charged particle such as an electron this force is

$$\vec{F} = -e\vec{\mathscr{E}} - e\left(\vec{v} \times \vec{B}\right) , \tag{3.1}$$

where e is the fundamental charge, the vectors $\vec{\mathscr{E}}$ and $\vec{B}$ are the electric and magnetic field vectors, respectively, and $\vec{v}$ is the particle's velocity vector. Consider an ideal magnetic spectrometer in cartesian coordinates: there are no electric fields present $\vec{\mathscr{E}} = 0$, the electron propagates initially only along the beam line $\vec{v}(0) = v\hat{z}$ and the constant

magnetic field acts only along one axis $\vec{B} = -B\hat{y}$. Thus,

$$\begin{aligned}\vec{F} = \gamma m_e \frac{d\vec{v}}{dt} &= -e\left(\vec{v} \times \vec{B}\right) , \\ &= -eB(v_z(t)\hat{x} - v_x(t)\hat{z}) , \end{aligned} \tag{3.2}$$

where m_e is the electron mass and γ is the electron's Lorentz factor. The components are

$$\frac{dv_x}{dt} = -\frac{eB}{\gamma m_e} v_z , \tag{3.3}$$

$$\frac{dv_y}{dt} = 0 , \tag{3.4}$$

$$\frac{dv_z}{dt} = \frac{eB}{\gamma m_e} v_x , \tag{3.5}$$

and therefore

$$\frac{d^2 v_z}{dt^2} + \frac{e^2 B^2}{\gamma^2 m_e^2} v_z = 0 , \tag{3.6}$$

which is the equation for a harmonic oscillator with frequency $\dfrac{eB}{\gamma m_e}$ and has the solution

$$v_z(t) = v \cos\left(\frac{eB}{\gamma m_e} t\right) . \tag{3.7}$$

Thus, the solution to Eq. (3.3) is

$$v_x(t) = v \sin\left(\frac{eB}{\gamma m_e} t\right) , \tag{3.8}$$

while the solution to Eq. (3.4) is

$$v_y(t) = v_y(0) = 0 . \tag{3.9}$$

Integrating Eq. (3.7) and Eq. (3.8) and defining the electron's initial position as the origin,

$$x(t) = \frac{\gamma m_e v}{eB}\left(1 - \cos\left(\frac{eB}{\gamma m_e} t\right)\right) , \tag{3.10}$$

$$z(t) = \frac{\gamma m_e v}{eB} \sin\left(\frac{eB}{\gamma m_e} t\right) . \tag{3.11}$$

The relationship between x and z at any time t is

$$\left(x(t) - \frac{\gamma m_e v}{eB}\right)^2 + z(t)^2 = \left(\frac{\gamma m_e v}{eB}\right)^2 , \tag{3.12}$$

that is, the electron traverses a circle of radius

$$\rho = \frac{\gamma m_e v}{eB} = \frac{\beta E}{eB} , \tag{3.13}$$

with centre $(\rho, 0, 0)$. The solution for a proton of energy E is the same up to the exchange $m_e \to m_p$ and the fact that the circle is centred on $(-\rho, 0, 0)$ due to the proton's positive charge.

This solution applies provided that the magnetic field is constant for the entirety of the particle's circular path. When the magnetic field changes, the force acting on the particle changes and it follows a new trajectory.

3.2. Analytic modelling

Consider a point where the magnetic field vanishes, $\vec{B} = 0$. At this point, the force is $\vec{F} = 0$. A particle with no forces acting upon it will propagate along a straight line at a constant velocity. For a particle that previously obeyed Eq. (3.12) this straight line is the tangent to that circle. This is proved in Appendix A. Dropping the t parametrisation to consider the system geometrically, Eq. (3.12) may be written

$$(x - \rho)^2 + z^2 = \rho^2 . \tag{3.14}$$

Now consider a simplified dipole field

$$\vec{B} = \begin{cases} (0, -B, 0) & 0 \leq x < M_H,\ 0 \leq z < M_L \\ (0, 0, 0) & \text{otherwise} \end{cases} , \tag{3.15}$$

where M_H and M_L respectively describe the transverse and longitudinal dimensions of the dipole. For a rectangular dipole orientated along the beamline M_H and M_L are constants but more generally they may be expressed as functions of x and z.

Suppose that M_H and M_L are both well known. At $(M_H, 0, L)$, where L is an unknown point, Eq. (3.14) gives

$$(M_H - \rho)^2 + L^2 = \rho^2 \,. \tag{3.16}$$

Thus

$$L = \pm\sqrt{M_H(2\rho - M_H)} \,. \tag{3.17}$$

Likewise, for the point $(H, 0, M_L)$, where H is unknown

$$H = \rho \pm \sqrt{\rho^2 - M_L^2} \,. \tag{3.18}$$

The gradient of the circle Eq. (3.14) is

$$\frac{dx}{dz} = \mp \frac{z}{\sqrt{\rho^2 - z^2}} \,, \tag{3.19}$$

and the tangent line at $(M_H, 0, L)$ can therefore be expressed as

$$x = M_H \pm z\frac{\sqrt{M_H(2\rho - M_H)}}{\rho - M_H} - \frac{M_H(2\rho - M_H)}{\rho - M_H} \,, \tag{3.20}$$

and at $(H, 0, M_L)$ it can be given by

$$x = \rho \pm \frac{\rho^2 - zM_L}{\sqrt{\rho^2 - M_L^2}} \,. \tag{3.21}$$

An example setup with a rectangular dipole oriented along the beamline, with $0 < M_H < \rho$ and $0 < M_L < \rho$, is illustrated in Figure 3.1. In this case, the appropriate choices are the $(+)$ and $(-)$ solutions for Eq. (3.20) and Eq. (3.21) respectively. These may both be expressed as polynomials in ρ with Eq. (3.20) becoming

$$(M_H + x)^2\rho^2 - 2M_H\left(x(M_H + x) + z^2\right)\rho + M_H^2(x^2 + z^2) = 0 \,, \tag{3.22}$$

and Eq. (3.21) becoming

$$2x\rho^3 - (x^2 - M_L^2 + 2M_L z)\rho^2 - 2xM_L^2\rho + M_L^2(x^2 + z^2) = 0 \,, \tag{3.23}$$

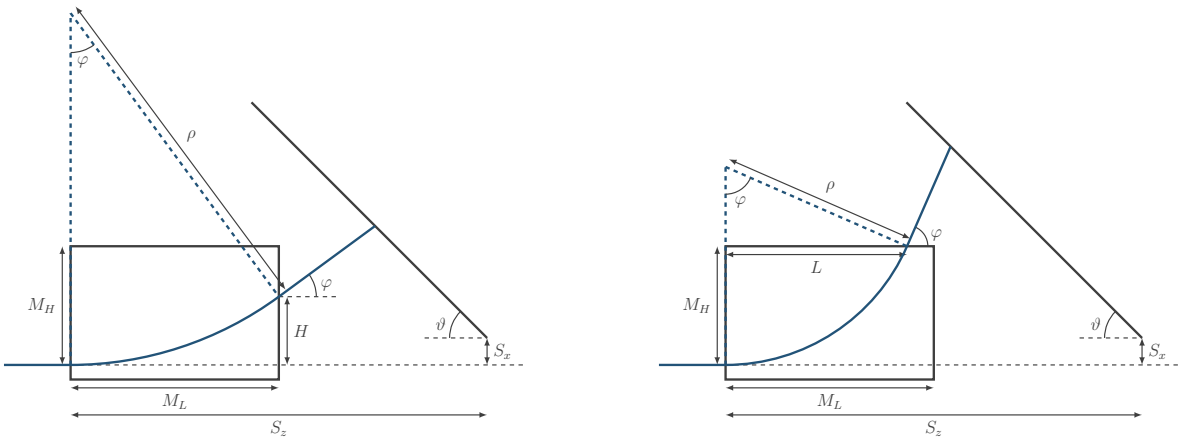

Figure 3.1.: Diagrams representing the spectrometer when an electron (blue) passes through the magnet. The diagram on the left corresponds to $\rho > \rho_c$ and the diagram on the right corresponds to $\rho < \rho_c$.

At the point $(M_H, 0, M_L)$ these expressions must yield the same solution, ρ_c, which is given by

$$\rho_c = \frac{M_H^2 + M_L^2}{2M_H} \,. \tag{3.24}$$

For the rectangular dipole in Figure 3.1 this corresponds to the top right corner. When $\rho \geq \rho_c$ the electron's path may be solved using Eq. (3.23) and when $\rho \leq \rho_c$ it may be solved using Eq. (3.22).

Consider the face of a detector of length S_L positioned in the x–z plane with one end at the point $(S_x, 0, S_z)$ oriented at angle $\pi - \vartheta$ to the z axis. This is illustrated in Figure 3.1. For simplicity a coordinate transform can be made, consisting of a counterclockwise rotation of $\frac{\pi}{2} - \vartheta$ in the x–z plane and a translation such that the origin is now at the point $(S_x, 0, S_z)$. That is

$$\begin{pmatrix} x \\ y \\ z \end{pmatrix} \rightarrow \begin{pmatrix} \cos\left(\frac{\pi}{2} - \vartheta\right) & 0 & -\sin\left(\frac{\pi}{2} - \vartheta\right) \\ 0 & 1 & 0 \\ \sin\left(\frac{\pi}{2} - \vartheta\right) & 0 & \cos\left(\frac{\pi}{2} - \vartheta\right) \end{pmatrix} \begin{pmatrix} x - S_x \\ y \\ z - S_z \end{pmatrix} = \begin{pmatrix} x' \\ y' \\ z' \end{pmatrix} \,. \tag{3.25}$$

With these coordinates, the face of the detector lies along the line $z' = 0$. A 'detector' coordinate ξ can be defined such that

$$\xi \equiv x'|_{z'=0} = \frac{S_z - z}{\cos\vartheta} = \frac{x - S_x}{\sin\vartheta} \,, \tag{3.26}$$

where $\xi \in [0, S_L]$ is the distance from the origin $(S_x, 0, S_z)$ of any point on the face of the detector. Substituting for ξ in Eq. (3.22) and Eq. (3.23) gives

$$0 = (M_H + S_x + \xi \sin\vartheta)^2\rho^2 - 2M_H\left((S_x + \xi\sin\vartheta)(M_H + S_x + \xi\sin\vartheta) + (S_z - \xi\cos\vartheta)^2\right)\rho + M_H^2\left((S_x + \xi\sin\vartheta)^2 + (S_z - \xi\cos\vartheta)^2\right), \tag{3.27}$$

and

$$0 = 2(S_x + \xi\sin\vartheta)\rho^3 - \left((S_x + \xi\sin\vartheta)^2 - M_L^2 + 2M_L(S_z - \xi\cos\vartheta)\right)\rho^2 - 2(S_x + \xi\sin\vartheta)M_L^2\rho + M_L^2((S_x + \xi\sin\vartheta)^2 + (S_z - \xi\cos\vartheta)^2). \tag{3.28}$$

Substituting for Eq. (3.24) in both of these polynomials, the ξ value corresponding to ρ_c is found to be

$$\xi_c = \frac{M_H(M_H^2 + M_L^2) - (M_H^2 - M_L^2)S_x - 2M_H M_L S_z}{(M_H^2 - M_L^2)\sin\vartheta - 2M_H M_L\cos\vartheta}. \tag{3.29}$$

The solution to Eq. (3.27) which satisfies $\rho(\xi_c) = \rho_c$ is

$$\rho_H(\xi) = \frac{M_H}{M_H + S_x + \xi\sin\vartheta}\left[S_x + \xi\sin\vartheta + \frac{(S_z - \xi\cos\vartheta)^2\left(1 + \sqrt{1 + \frac{(S_x+\xi\sin\vartheta)^2 - M_H^2}{(S_z-\xi\cos\vartheta)^2}}\right)}{M_H + S_x + \xi\sin\vartheta}\right], \tag{3.30}$$

and the corresponding solution to Eq. (3.28) may be expressed as

$$\rho_L(\xi) = \frac{1}{3a_3}\left[-a_2 + \frac{2^{\frac{1}{3}}(a_2^2 - 3a_3a_1)}{\left(-2a_2^3 + 9a_3a_2a_1 - 27a_3^2a_0 + \sqrt{(2a_2^3 - 9a_3a_2a_1 + 27a_3^2a_0)^2 - 4(a_2^2 - 3a_3a_1)^3}\right)^{\frac{1}{3}}} + \frac{\left(-2a_2^3 + 9a_3a_2a_1 - 27a_3^2a_0 + \sqrt{(2a_2^3 - 9a_3a_2a_1 + 27a_3^2a_0)^2 - 4(a_2^2 - 3a_3a_1)^3}\right)^{\frac{1}{3}}}{2^{\frac{1}{3}}}\right], \tag{3.31}$$

where the a_i are the coefficients of ρ^i in Eq. (3.28). This can also be expressed more succinctly as

$$\rho_L(\xi) = \frac{1}{3a_3}\left[-a_2 + 2\sqrt{a_2^2 - 3a_3a_1}\cos\left(\frac{1}{3}\arccos\frac{-2a_2^3 + 9a_3a_2a_1 - 27a_3^2a_0}{2(a_2^2 - 3a_3a_1)^{\frac{3}{2}}}\right)\right]. \tag{3.32}$$

Assuming that the electrons incident upon the detector are relativistic[1], such that $\beta \simeq 1$, their energy can be now be expressed as

$$E(\xi) = \begin{cases} eB\rho_L(\xi) & 0 \leq \xi \leq \xi_c \\ eB\rho_H(\xi) & \xi_c < \xi \leq S_L \end{cases} . \tag{3.33}$$

3.2.1. Nominal parameters

The parameter values for the spectrometer at AWAKE are given in Table 3.1. The detector in this case is a scintillating screen and the physical parameters defining the position of the screen relative to the magnet, S_x, S_z and ϑ, have been measured by the CERN survey team [69]. The parameters M_H, M_L are taken as having no uncertainties since the purpose of the analytic model is to consider a uniform field confined within a well defined region.

The length of the scintillator is $S_L = 0.997\,\text{m}$. With the AWAKE parameters Eq. (3.29) gives $\xi_c = 0.5611 \pm 0.0015\,\text{m}$, approximately the middle of the scintillator. The variance has been calculated as

$$\sigma_{\xi_c}^2 = \left(\frac{\partial \xi_c}{\partial \vartheta}\sigma_\vartheta\right)^2 + \left(\frac{\partial \xi_c}{\partial S_x}\sigma_{S_x}\right)^2 + \left(\frac{\partial \xi_c}{\partial S_z}\sigma_{S_z}\right)^2 . \tag{3.34}$$

This is reasonable because there is little correlation between the measurements[2] of any of the parameters and ξ_c is well described by its first order Taylor expansion in the neighbourhood[3] of the parameter values [70].

Figure 3.2 shows ρ_H and ρ_L for these parameters and the values can be seen to meet at ξ_c. The transition is not smooth, however, as can be seen in Figure 3.3d. This is because there is no requirement that

$$\left.\frac{\partial \rho_H}{\partial \xi}\right|_{\xi_c} = \left.\frac{\partial \rho_L}{\partial \xi}\right|_{\xi_c} , \tag{3.35}$$

and in general this will not be the case.

[1] At AWAKE, electrons entering the spectrometer have a minimum energy of approximately 18 MeV, corresponding to $\beta = 0.9996$.

[2] The survey is conducted in such a way as to minimise the correlations.

[3] The size of the 'neighbourhood' depends on the value of σ.

Parameter	Value
S_z	$1.676 \pm 0.001\,\mathrm{m}$
S_x	$0.0620 \pm 0.0005\,\mathrm{m}$
ϑ	$44.80 \pm 0.01^\circ$
M_H	$0.285\,\mathrm{m}$
M_L	$1\,\mathrm{m}$

Table 3.1.: Measured values for each of the parameters defined in Figure 3.1.

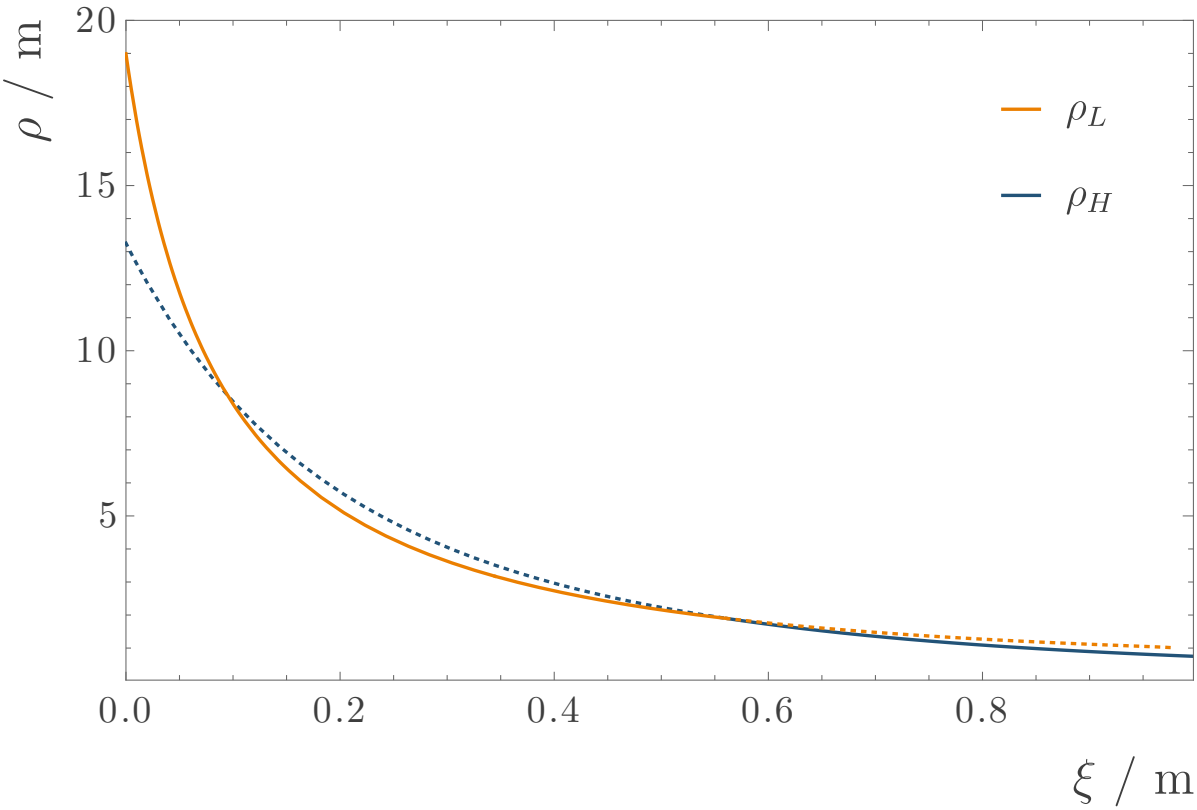

Figure 3.2.: The analytic solutions to the radius of curvature ρ of electrons in the AWAKE spectrometer as a function of their position on the scintillator ξ. The solutions are shown with solid lines in their respective domains ($\xi \in [0, \xi_c]$ for ρ_L and $\xi \in (\xi_c, S_L]$ for ρ_H) and dotted lines outside them.

The ϑ derivative of ρ is shown in Figure 3.3a. The definition of $\xi = 0$ as the point of rotation of the screen (see Figure 3.1) means that there is no sensitivity to ϑ at this point. The other position where the derivative falls to 0 is at $\xi = 0.84\,\mathrm{m}$, this is where the electron is normally incident on the scintillator.

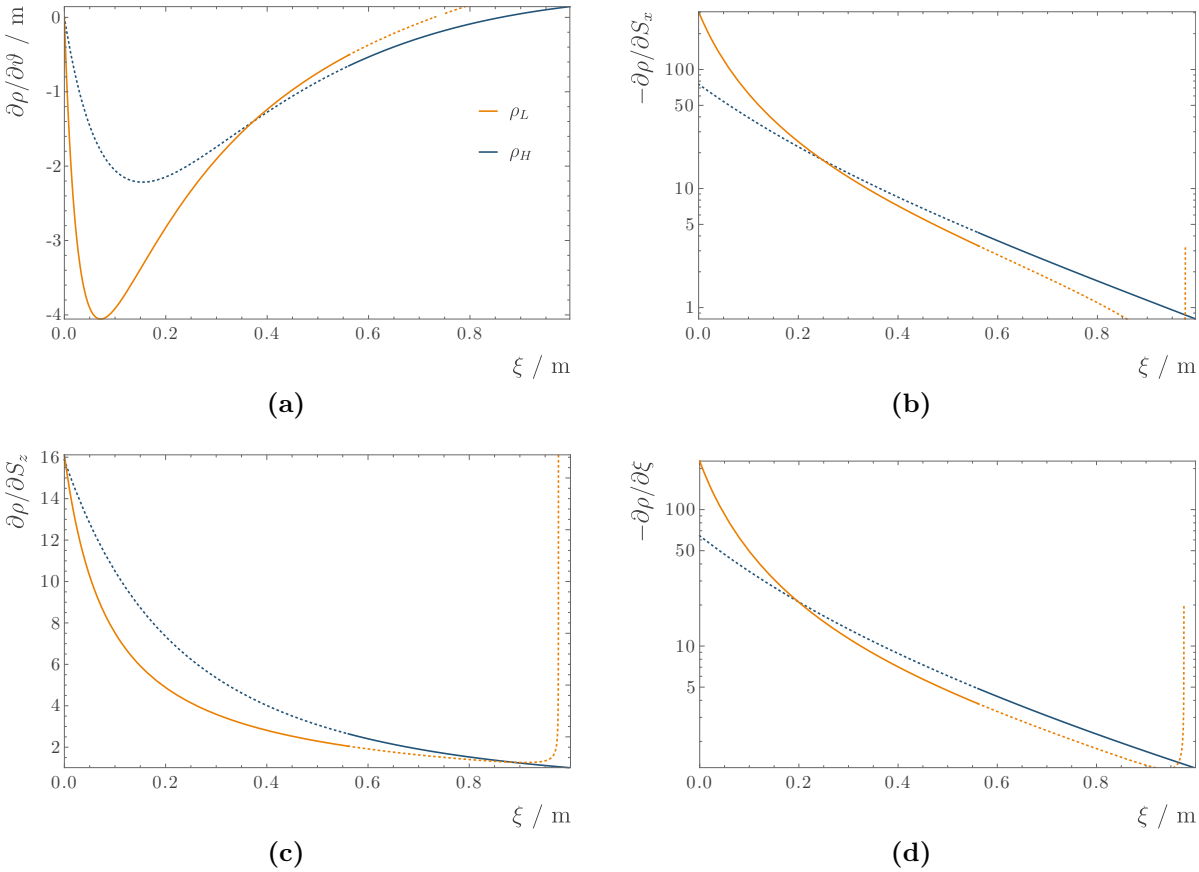

Figure 3.3.: Derivatives of the two ρ functions shown in Figure 3.2.

3.3. BDSIM model

Beam Delivery Simulation BDSIM is a C++ code simulating particle transport and particle–matter interactions (through Geant4). The input beam used below is for an energy range from 10 MeV to 10 GeV in steps of 0.1 MeV. This energy spacing has sufficient resolution for analysing experimental results at AWAKE but in order to compare the field maps with the analytic functions the points are interpolated using a third order polynomial.

3.3.1. Field maps

A number of field maps for the dipole used at AWAKE have been provided by the CERN magnets group [71]. These field maps have been generated using OPERA, a finite element program, and compared to measurements for the magnet. The maps contain the full details of the magnet's fringe fields and the extension beyond the dipole. Simulations have been performed for each field map with S_x, S_z and ϑ varied by their uncertainties on each (a total of 8 simulations per field map). The simulated E–ξ lines and uncertainties for each field map are shown in Figure 3.4. The uncertainty is conservatively given as the maximum deviation from the central value as a function of ξ. That is

$$\sigma_E(\xi) = \max\{|E(S_x \pm \sigma_{S_x}, S_z \pm \sigma_{S_z}, \vartheta \pm \sigma_\vartheta, \xi) - E(S_x, S_z, \vartheta, \xi)|\} \,. \tag{3.36}$$

This is not, however, the only source of uncertainty in the energy. A comparison of the simulated and measured values of the magnetic field by the magnet group indicates a difference of up to 2% at any given point. Furthermore, the optical system imaging the scintillator has a finite resolution[4] of $\sigma_\xi \simeq 2\,\text{mm}$ (discussed in Section 5.3). Therefore the total variance in the E–ξ conversion is given by

$$\sigma^2_{E,\text{tot}}(\xi) = \sigma^2_E(\xi) + \left(\frac{E(\xi)}{50}\right)^2 + \left(\frac{\partial E(\xi)}{\partial \xi}\sigma_\xi\right)^2 \,. \tag{3.37}$$

For completeness, the ξ derivatives of each field map are given in Figure 3.5.

[4] The width of the scintillator, the emission profile of the scintillator photons and the scattering of the electrons by the vacuum window all provide negligible contributions compared to this.

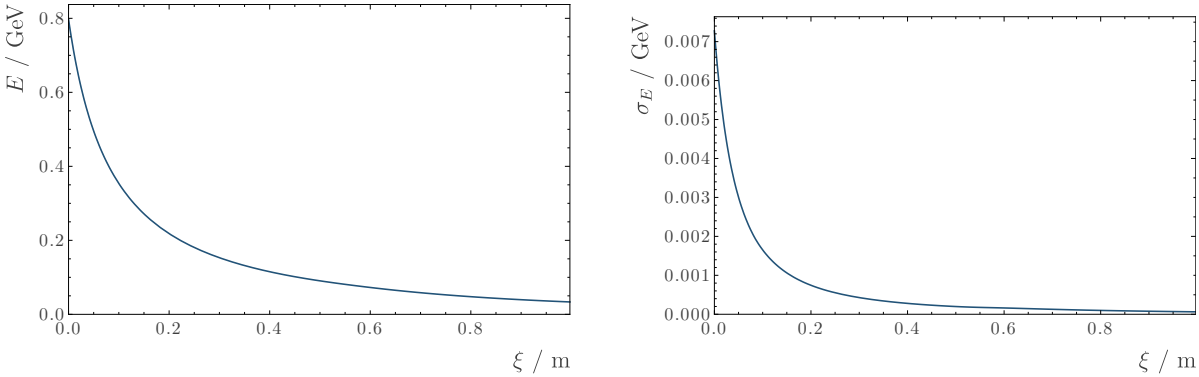

(a) 40 A

(b) 40 A

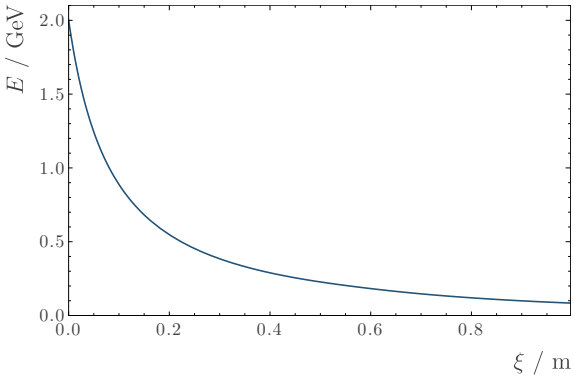

(c) 100 A

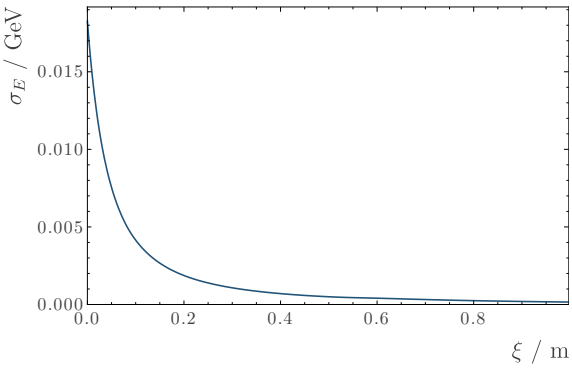

(d) 100 A

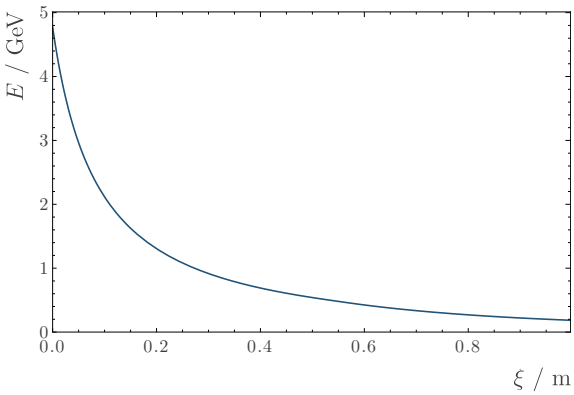

(e) 240 A

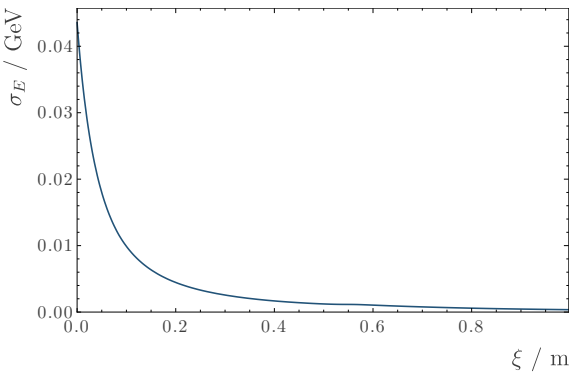

(f) 240 A

Figure 3.4.: Simulated E–ξ relationship and its uncertainty for each of the field maps.

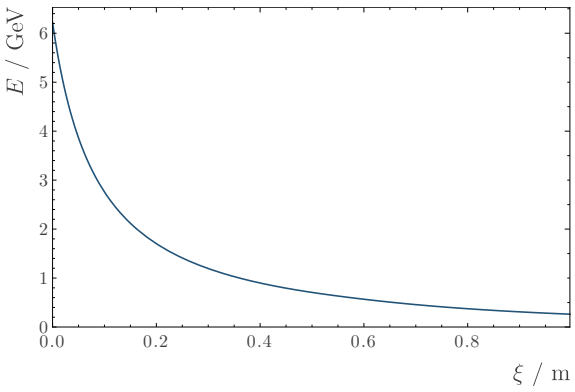

(g) 320 A

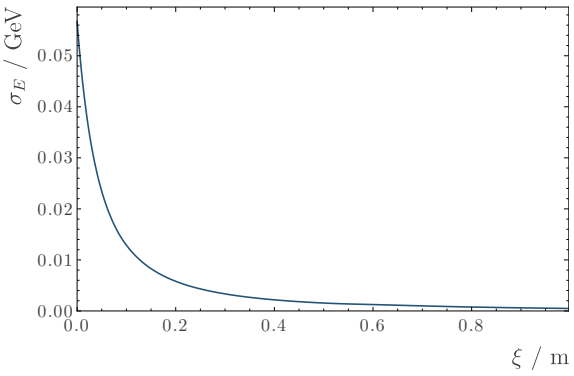

(h) 320 A

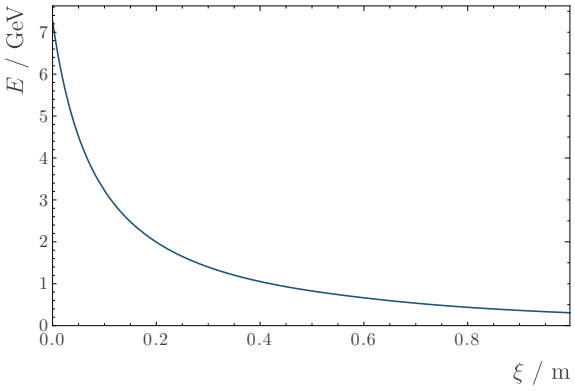

(i) 400 A

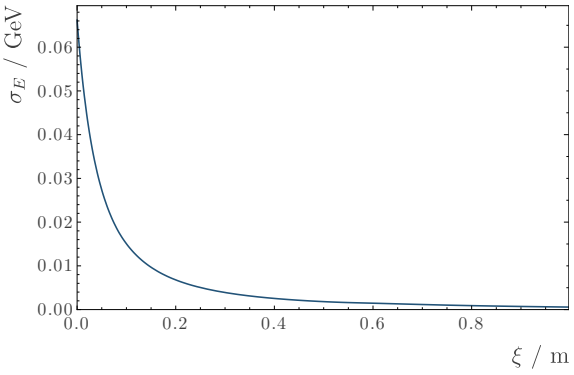

(j) 400 A

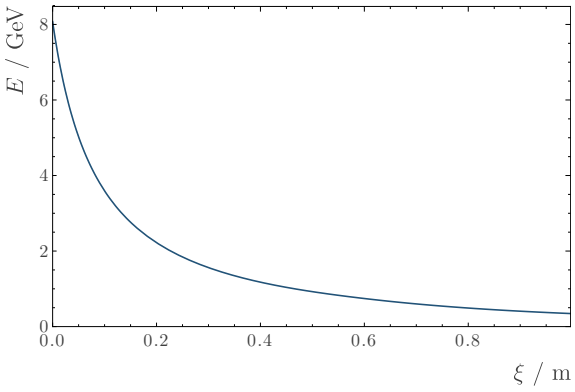

(k) 540 A

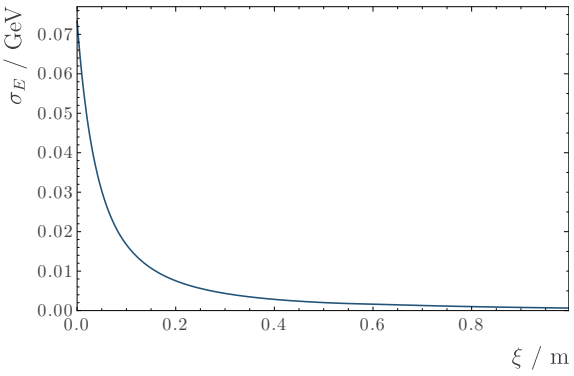

(l) 540 A

Figure 3.4.: Simulated E–ξ relationship and its uncertainty for each of the field maps (continued).

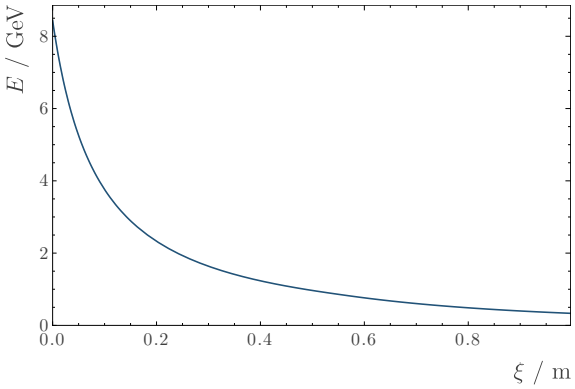

(m) 650 A

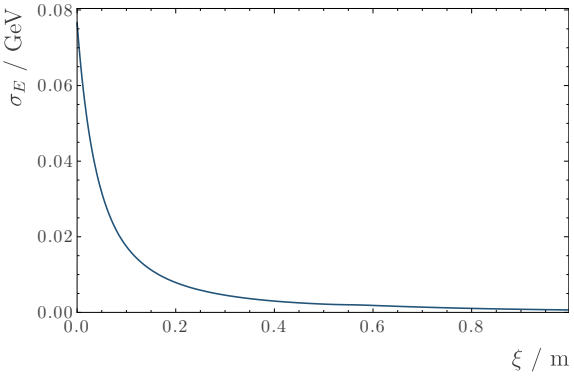

(n) 650 A

Figure 3.4.: Simulated E–ξ relationship and its uncertainty for each of the field maps (continued).

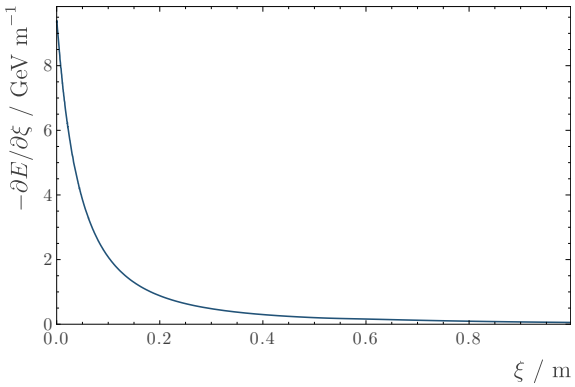

(a) 40 A

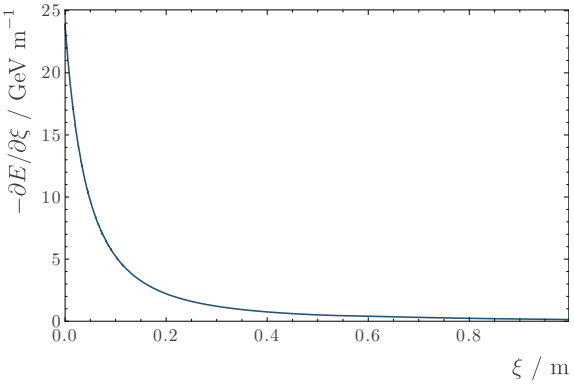

(b) 100 A

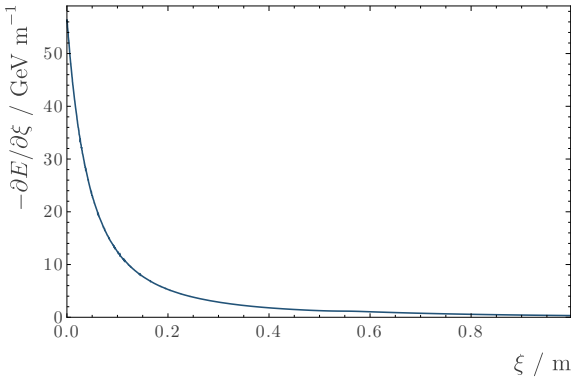

(c) 240 A

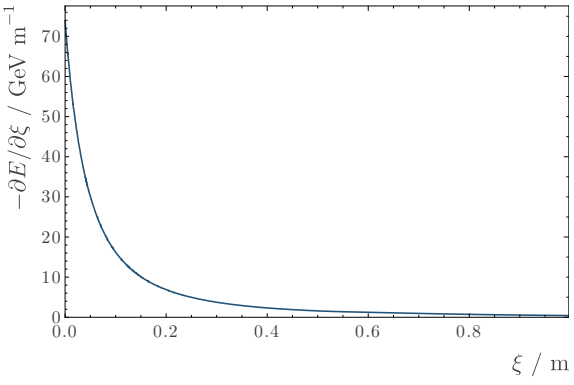

(d) 320 A

Figure 3.5.: Numerical derivatives of the simulated E–ξ functions for each of the field maps.

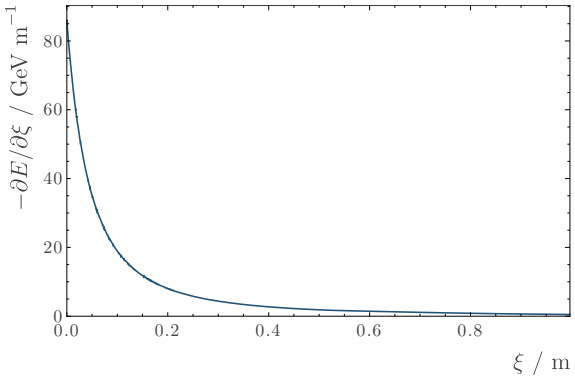

(e) 400 A

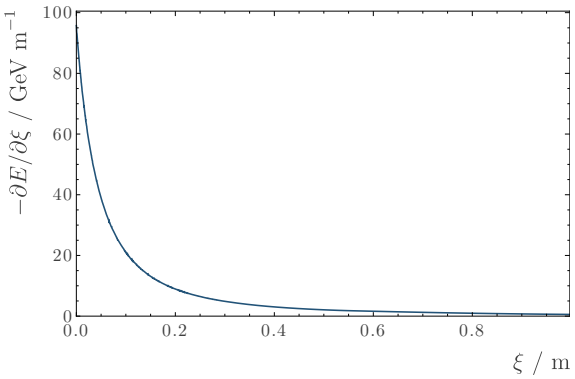

(f) 540 A

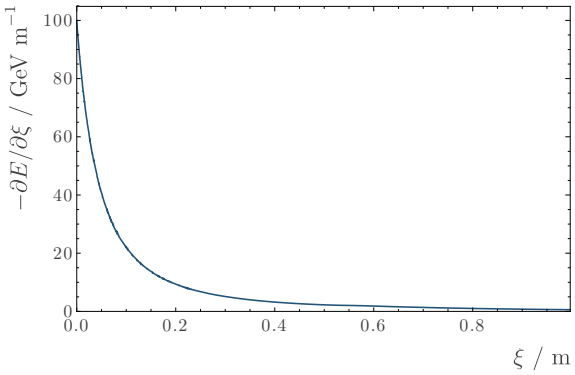

(g) 650 A

Figure 3.5.: Numerical derivatives of the simulated E–ξ functions for each of the field maps (continued).

3.3.2. Matching models

In some cases, the spectrometer magnet must be used with currents which do not have a simulated field map. An example of this is for measurements of the input electron beam, which has an energy of approximately 18 MeV. This cannot be measured with the 40 A magnetic field which has $E(S_L) \sim 90\,\text{MeV}$. For this energy, the magnet is run at its minimum possible current of 18 A. In this case Eq. (3.33) may be used[5]. In order to estimate the appropriate value of B to use, a linear function of dipole current I against B_{fit} is fit, where B_{fit} is the value of B which minimises

$$\int_0^{\xi_c} \frac{\left(eB\rho_L(\xi) - E_X(\xi)\right)^2}{\sigma^2_{E_X}(\xi)} d\xi + \int_{\xi_c}^{S_L} \frac{\left(eB\rho_H(\xi) - E_X(\xi)\right)^2}{\sigma^2_{E_X}(\xi)} d\xi \,, \tag{3.38}$$

for each simulated field map X. A 2% uncertainty is given to each value, in analogy with the field map uncertainties. The lowest four values of B_{fit} are fit against I and the result is shown in Figure 3.6. These correspond to the values for the 40 A, 100 A, 240 A and 320 A field maps. Comparisons of three of the E–ξ simulation results with the values of Eq. (3.33) using B_{fit} are shown in Figure 3.7. In this case, the uncertainty band on E_X is σ_{E_X} and the uncertainty band on the analytic function is from the uncertainty in B.

While the overall approximation is broadly accurate on the level of 2–3% the fits generally get worse for $\xi > \xi_c$. This is largely due to fringe fields of the magnet. The extent of the simulated fringe field in $+z$ and $+x$ is similar, approximately 0.3 m [72], however, the length of the particle's trajectory through the pole of the magnet, $\ell_\varphi = \rho\varphi$ decreases for $\xi > \xi_c$. This is shown in Figure 3.8, with $\varphi = \arcsin \frac{M_L}{\rho_L}$ for $\xi \leq \xi_c$ and $\varphi = \arccos \frac{\rho_H - M_H}{\rho_H}$ for $\xi > \xi_c$. Decreasing ℓ_φ means that the magnet's fringe field plays a more significant role, the particles are bent more by the magnetic field, and the approximation of a confined uniform field gets worse.

Figure 3.9 shows the analytic E–ξ relation for an 18 A dipole field with $B = 0.06354 \pm 0.00072\,\text{T}$. The total variance is given by

$$\begin{aligned}\sigma^2_{18\,\text{A}}(\xi) = &\left(\frac{\partial E(\xi)}{\partial S_x}\sigma_{S_x}\right)^2 + \left(\frac{\partial E(\xi)}{\partial S_z}\sigma_{S_z}\right)^2 + \left(\frac{\partial E(\xi)}{\partial \vartheta}\sigma_\vartheta\right)^2 \\ &+ \left(\frac{\partial E(\xi)}{\partial \xi}\sigma_\xi\right)^2 + \left(\frac{\partial E(\xi)}{\partial B}\sigma_B\right)^2 .\end{aligned} \tag{3.39}$$

[5] An alternative approach would be to attempt to rescale the 40 A field map's strength.

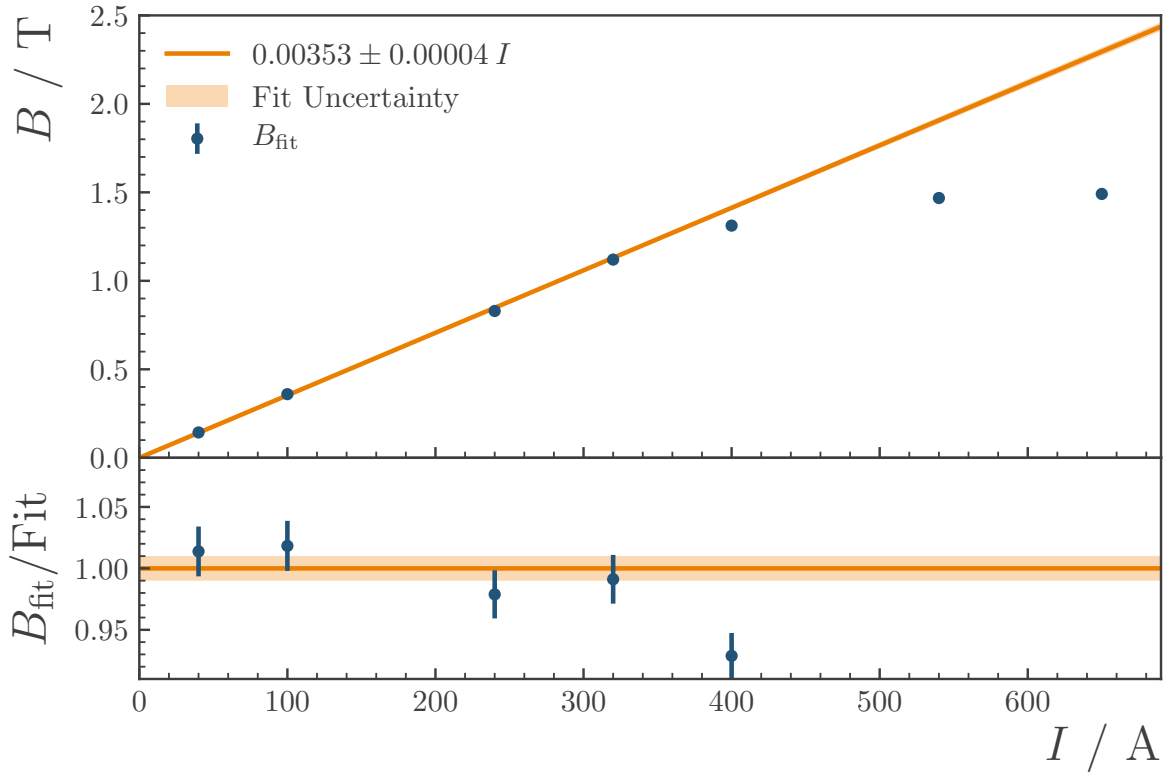

Figure 3.6.: A fit against current of the four values of B_{fit} corresponding to the lowest strength field maps.

With this model an 18 MeV electron beam would be measured at $\xi = 0.871 \pm 0.006$ m. Since this value is greater than ξ_c it may be poorly approximated, as described above. An alternative approach is to set B by minimising only the second term in Eq. (3.38), since this is the relevant region. This results in $B = 0.0655 \pm 0.0009$ T which gives $\xi = 0.8872 \pm 0.0075$ m for an 18 MeV beam. Measurements of the AWAKE injection electron beam show its mean position to be $\xi = 0.890 \pm 0.004$ m, in good agreement with the latter prediction.

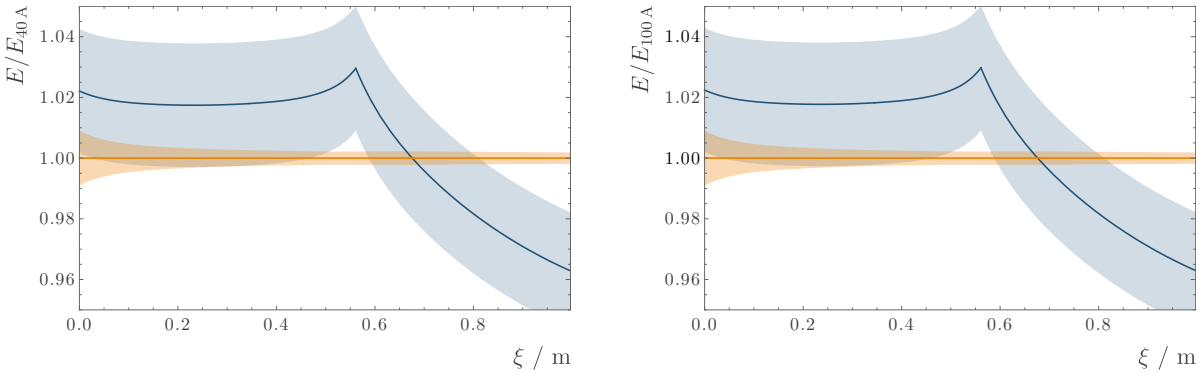

(a) 40 A

(b) 100 A

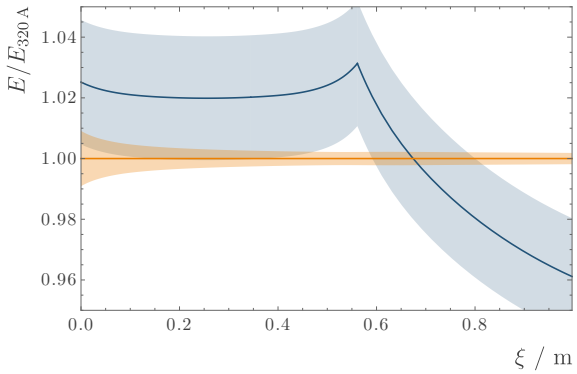

(c) 320 A

Figure 3.7.: Comparisons of three of the simulated field maps (orange) to the analytic model using a B value found by minimising Eq. (3.38) (blue). The orange band is σ_E as defined in Eq. (3.36) and the blue band is due to the 2% uncertainty given to B.

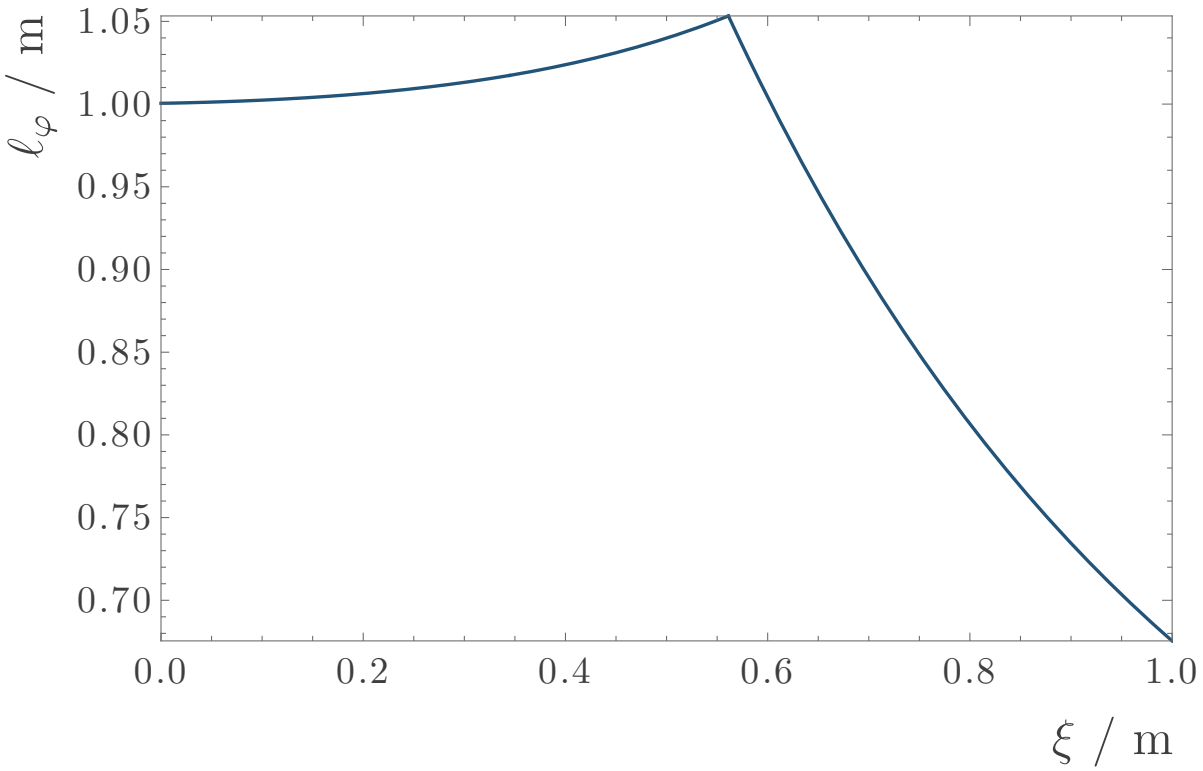

Figure 3.8.: The path length through the magnet $\ell_\varphi = \rho\varphi$ in the analytic model.

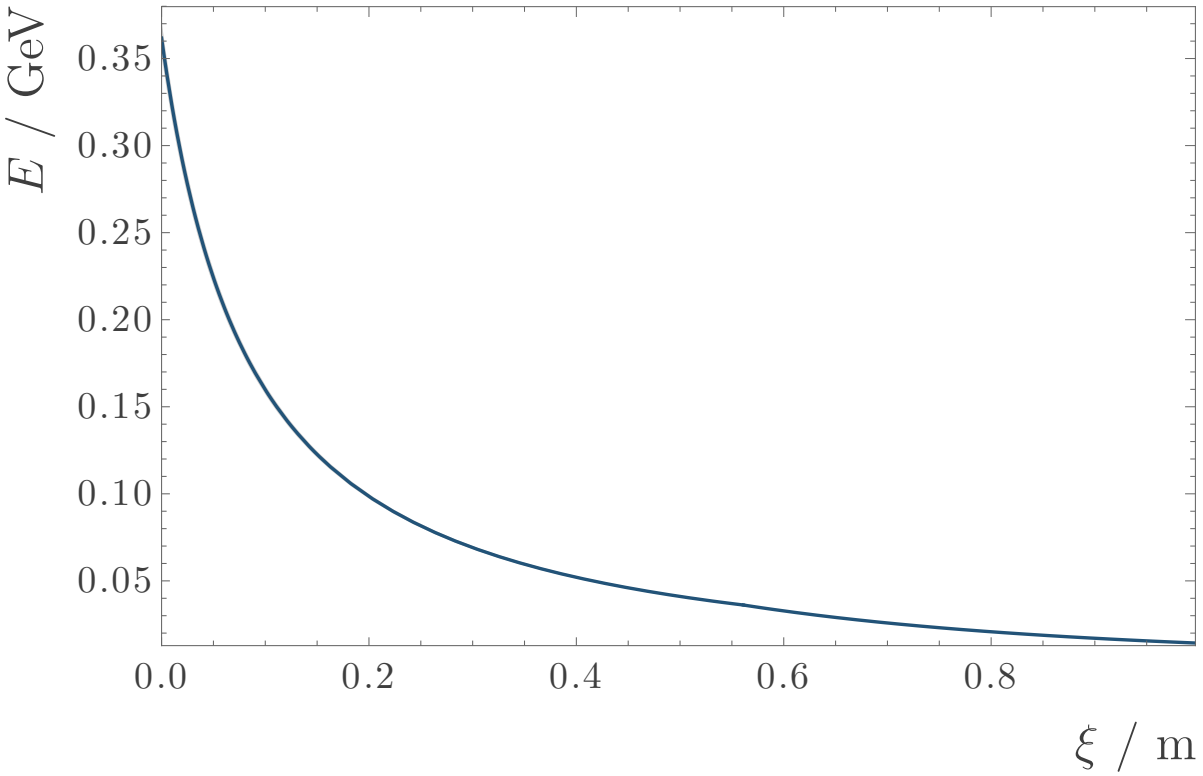

Figure 3.9.: Analytic model for an 18 A dipole field, using the B value from a fit to the B_{fit} values.

Chapter 4.

Spectrometer design

This chapter presents the design of the magnetic spectrometer used to measure accelerated electrons at AWAKE. First, an overview of the spectrometer's design is given in Section 4.1. The components of the spectrometer on or close to the beamline, including the magnets and the vacuum system, are presented in Section 4.2. The spectrometer's multicomponent optical line is detailed in Section 4.3 and the data acquisition and control framework is outlined in Section 4.4.

4.1. Design overview

The spectrometer has been designed to fulfil the following requirements:

- Separate the accelerated electrons from the drive bunch protons.
- Introduce a dispersion, a transverse spatial distribution that is a function of energy, into the accelerated bunch.
- Measure the spatial intensity distribution of the accelerated electrons to allow the mean energy, energy spread and bunch charge to be calculated.
- Provide sufficient acceptance to prevent significant loss of accelerated electrons before the energy measurement.
- Provide sufficient dynamic range to allow measurement of a range of electron energies from 0–5 GeV.
- Measure the energy profile of the electron bunch with sufficient resolution to demonstrate proton-driven plasma wakefield acceleration of witness bunch electrons.

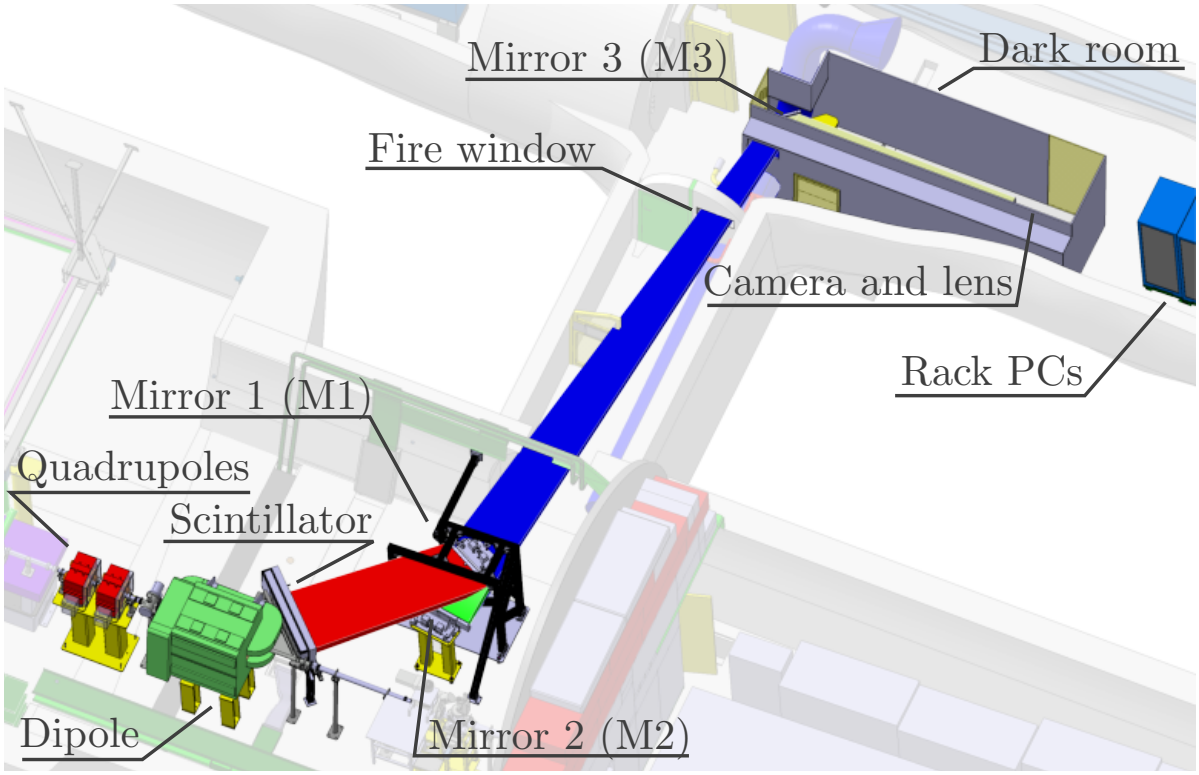

Figure 4.1.: Spectromer components at AWAKE. The key components of the spectrometer are labelled. The calibration lamp (not labelled) sits on a rail in front of the scintillator. The coloured blocks (red, green, blue, yellow) indicate the unobstructed light paths from the scintillator to the camera via M1, M2 and M3.

The layout of the spectrometer within the AWAKE tunnels is shown in Figure 4.1. The spectrometer begins with a quadrupole doublet, the first of which has an upstream face 4.631 m downstream of the plasma cell exit. The upstream face of the second quadrupole is a further 0.495 m downstream and the upstream face of the dipole is 1.290 m beyond that. The dipole is a C-shaped horizontal bend magnet and the spectrometer's triangular vacuum chamber sits inside the cavity between its poles. The vacuum chamber is terminated by a thin window which allows high energy electrons to pass through it. On the exterior surface of this window is a scintillating phosphor screen which emits photons where particles deposit energy within it. A portion of these scintillator photons are reflected to an adjacent tunnel via three large mirrors. The first mirror (M1) is held at the height of the scintillator and reflects the light down and backwards to the second mirror (M2), which sends the photons through a connecting tunnel to the third mirror (M3). The optical line terminates with a long focal length lens attached to an intensified CCD camera. The final part of the optical line is shielded from outside sources by a darkroom within the tunnel.

Parameter	Value
Total length	0.320 m
Iron length	0.285 m
Total width	0.500 m
Total height	0.500 m
Peak current	362 A
Peak field gradient	18.1 T m^{-1}

Table 4.1.: Parameters of the spectrometer quadrupoles.

4.2. Beamline components

4.2.1. Quadrupole doublet

The spectrometer utilises an electromagnetic quadrupole doublet to focus accelerated beams onto the scintillator. The quadrupoles have been designed and fabricated by CERN and the key parameters are given in Table 4.1 [71]. The quadrupoles focus in different axes and are separated by a drift of 0.175 m (downstream face to upstream face). The beam pipe running through the doublet has a diameter of 70 mm.

The first quadrupole focuses in the horizontal plane while the second quadrupole focuses in the vertical. The quadrupoles are powered using a single unit meaning that by default they have the same strength and therefore focal length. This creates an issue, since the quadrupoles are at different positions along the beamline and, hence, focus to a different location. To ensure that both the quadrupoles focus onto the scintillator the strength of the first quadrupole was reduced by 6% using a resistive circuit. This change of 6% is an approximation since the path length of the electrons through the system and, hence, the appropriate focal length varies with energy and magnetic field strength (cf. Figure 3.8). Consequently, no single resistance value can provide a perfect focal spot everywhere on the scintillator and the change of -6% represents a compromise, providing reasonable focusing across the surface [73–75]. This change to the quadrupole strength was made after the first AWAKE dataset (May 2018).

4.2.2. Dipole

The spectrometer's dipole is shown installed at AWAKE in Figure 4.2. The magnet's iron pole is 1 m long and 0.32 m wide, with the centre of the beamline offset by 35 mm (the beam pipe's radius) from one side of the pole. The magnet operates at currents between 18 A and 650 A with corresponding field strengths of approximately 0.07 T and 1.5 T, as discussed in Section 3.3.

4.2.3. Vacuum chamber

To reduce beam loss, the accelerated electrons are kept under vacuum while they are bent through the magnet. This is achieved using a large triangular vacuum chamber which sits in the cavity of the spectrometer's dipole. The vacuum in the beamline downstream of the plasma cell is designed to be 10^{-6} mbar. The downstream end of the chamber can be seen in Figure 4.2 and a technical drawing may be found in Ref. [76]. The majority of the chamber is within the aperture of the dipole, restricting its height to 80 mm. To prevent electron loss the inside of the chamber is kept free of struts and stiffeners. This restriction combined with the size of the chamber necessitates a thick wall to prevent buckling; 6 mm of stainless steel. Further stability is added by attaching the top and bottom of the chamber to the sides of the magnet.

4.2.4. Vacuum window

The vacuum chamber is terminated by a 2 mm thick vacuum window, through which the accelerated electrons pass. This window, with the scintillator attached to it, may be seen in Figure 4.2 and a technical drawing may be found in Ref. [77]. The window has a thick frame for bolting to the vacuum chamber and a thin section consisting of a 62 mm high, 997 mm wide obround. An obround was chosen because corners would create potential weak points in the window. This obround defines the shape of the scintillator, which is machined to match its dimensions. The window is fabricated using a single solid sheet of alumnium 6082-T6, avoiding the need for welding which could create weak points. The sheet's grain size is approximately 10–20 μm, giving at least 100 grains across the thickness of the window, ensuring it is leak-tight. The window is manufactured to a thickness tolerance of 0.05 mm and metrology tests confirm that this has been met across the surface.

Figure 4.2.: The spectrometer vacuum chamber and dipole magnet installed at AWAKE. The image is taken facing upstream, towards the SPS transfer line. The scintillator (white) may be seen on the exterior surface of the vacuum window at approximately 45° to the beam line.

4.2.5. Scintillator

A DRZ-High scintillating screen is used in the spectrometer. This is a terbium doped gadolinium oxysulfide (Gd_2O_2S:Tb) scintillator manufactured by Mitsubishi [78]. The scintillator's thickness is 507 μm [79] and its transverse dimensions have been machined to match the obround of the vacuum window. DRZ-High is a scintillator with high brightness but poorer resolution than comparable products (DRZ-Std, for example) and was chosen to ensure the best possible signal, maximising the chance of detection at the possible expense of larger uncertainties on the measured parameters.

The scintillator is attached to the exterior of the vacuum window using a 0.2 mm thick double sided adhesive tape. The adhesive is thin, minimising the drift between the vacuum window and the electrons, giving a small distance for the bunch to diverge and, therefore, a sharper signal. While a permanent adhesive layer may have reduced this distance further, replacement of the scintillator would have been difficult. As such, the adhesive tape was chosen for its versatility.

Terbium doped gadolinium oxysulfide scintillators have a sharp phosphor emission peak around 545 nm. The optical components along the spectrometer line have been optimised for this wavelength.

4.2.6. Calibration lamp

Adjacent to the scintillator is a motorised rail with a lamp fixed to it. This setup is shown in Figure 4.3. The lamp is a diffuse emitter of green light, mimicking the scintillator, and is used to calibrate various aspects of the optical system. The lamp is powered by a programmable power supply which sits in TSG4, to prevent radiation damage, and is connected via a long cable. The lamp's power and position can both be varied remotely. During experimental running the lamp is moved to the side of the scintillator, as in Figure 4.3, and powered off.

A mask, shown in Figure 4.4, is used to benchmark the resolution of the optical system and scanning the lamp across the plane of the scintillator gives a measure of the system's spatial uniformity. The full details of the various calibrations using the lamp will be discussed in Chapter 5.

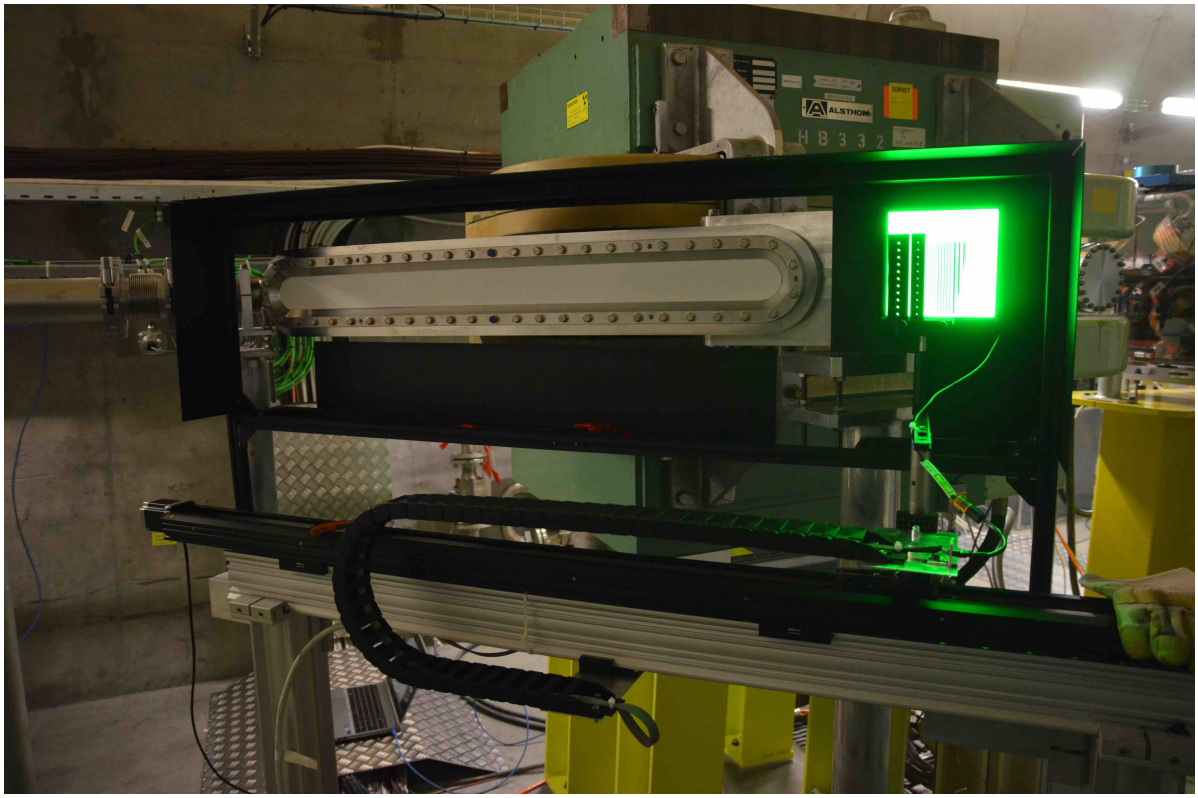

Figure 4.3.: Calibration lamp and control rail for the spectrometer. The lamp and scintillator are surrounded by matte black shielding to reduce reflection of ambient light.

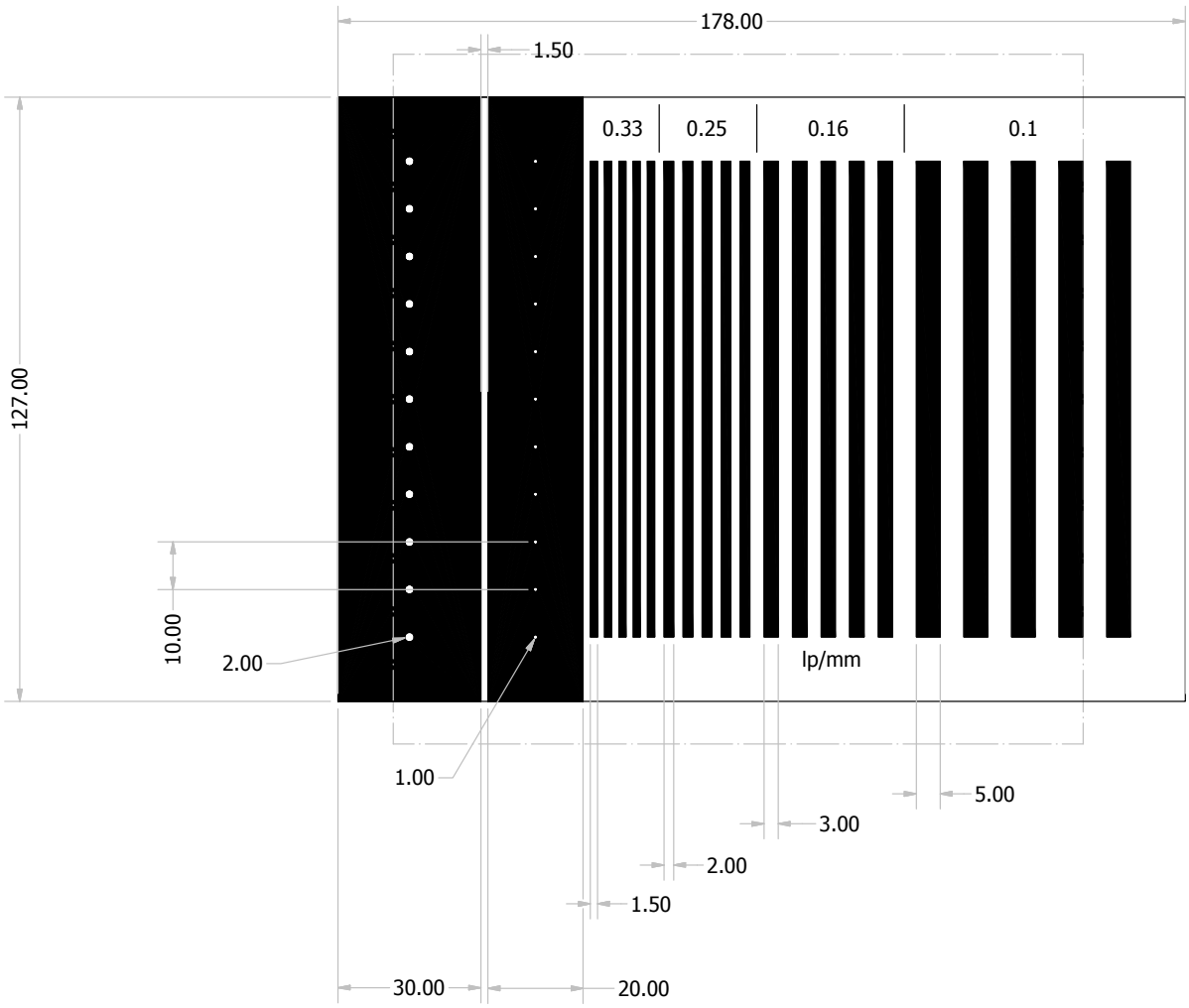

Figure 4.4.: Mask for the calibration lamp. The distances given are in millimetres.

4.3. Optical components

4.3.1. Camera and lens

The spectrometer uses an Andor iStar 340T, an intensified camera with a 2048×512 pixel CCD. The intensifier in the camera converts incoming photons into electrons using a photocathode. These electrons are accelerated towards the camera's microchannel plate (MCP) by an applied voltage. The MCP is a perforated glass disc with micron scale channels through it, across which a high voltage is applied, further accelerating the photocathode electrons. When the photoelectrons gain sufficient energy they free electrons from the MCP, which are in turn accelerated and free more electrons, creating an electron cloud. The electron cloud is then incident upon a scintillator within the intensifier, converting the electrons back to photons which are then incident upon the CCD. The multiplication of the photoelectrons and, hence, the multiplicity of the photons incident upon the CCD, is dependent on the voltage applied across the MCP which may be varied; this is the camera's so-called 'gain' setting. The activation of the intensifier is controlled by the camera's digital delay generator (DDG). The width and timing of the DDG's activation window, known as the 'gate', can be adjusted with a precision of 10 ps. The scintillator used in the spectrometer camera's image intensifier is P43, a Gd_2O_2S:Tb scintillator similar to that used for the accelerated electrons. The shape of the intensifier restricts the camera's active pixels to approximately 1850 in the horizontal axis; the exact active width number varies with vertical position on the CCD.

The camera's CCD is cooled to -30°C using an in-built Peltier device, the heat sink of which is water-cooled using a closed circuit liquid cooler. The cooler circulates a 2:1 mixture of distilled water and ethylene glycol at 12°C. This cooling reduces thermal noise in the images.

A unique challenge for the spectrometer is the high level of radiation generated by the SPS proton bunch passing through the AWAKE tunnel. If the camera were positioned close to the beamline this radiation would damage the camera[1] and lead to considerable image noise. To prevent this, the camera is located in an adjacent tunnel, as shown in Figure 4.1, and fitted with a long focal length lens to image the scintillator. The lens used is a Nikon AF-S NIKKOR 400 mm $f/2.8$E FL ED VR. The front of the lens is fitted with a 100 nm bandwidth filter centred on 550 nm to reduce the background from

[1] Several of the other diagnostic cameras close to the AWAKE beamline experienced regular failures due to radiation during experimental running.

Figure 4.5.: The spectrometer camera and lens in the darkroom. The lens is covered by a lens hood. The final mirror may be seen, out of focus, on the right side of the image.

ambient light while maintaining the scintillator signal. The low f-number and long focal length of the lens allow good light capture and resolution despite the long distance (17 m in the final alignment) between the camera and the scintillator.

The camera and lens are mounted on translation stages fixed to a flattened optical table, as shown in Figure 4.5. This table sits inside a darkroom, shown on the right side of Figure 4.1, which reduces light from sources other than the scintillator. Due to safety restrictions, many of the lights in the AWAKE tunnels cannot be switched off, including those in the area around the camera. These lights are much brighter than the typical glow of the scintillator and would introduce a significant background contribution to the images without the darkroom. Inside the darkroom there are no lights and it is sealed during experimental running to be fully light tight.

Mirror	Width / mm		Height / mm	
	Clear	Full	Clear	Full
M1	898.2	926.0	121.5	150.0
M2	819.5	926.0	126.4	150.0
M3	504.6	524.0	140.5	160.0

Table 4.2.: Clear apertures of the mirrors defined by simulation and full sizes of the acquired mirrors.

4.3.2. Mirrors

The parameters of the lens, the 17 m distance between the camera and the scintillator and the position of the mirrors (largely dictated by tunnel shapes) were used as inputs to a Zemax OpticStudio simulation to define the required clear aperture for each mirror. These values are given in Table 4.2 along with the actual size of the mirrors acquired. The decision to keep M1 and M2 the same size was practical since a single spare could be used to replace either M1 or M2.

In addition to the dimensions, the OpticStudio simulation defined the flatness of the mirrors. Preliminary tests of the camera and lens showed that directly imaging a target at a 17 m distance had a resolution limit of approximately 1.5 mm and, as such, this was the design specification chosen for the mirrors [80]. To achieve this the simulation gave a requirement for the mirror flatness of $\lambda/2$ within any 100 mm. That is, at any point the mirror should be flat to approximately 270 nm within a 100 mm radius. This flatness requirement is modest by the standards of traditional optics, where a flatness of $\lambda/10$ would be typical for laser mirrors. The surface area of the spectrometer mirrors, however, is approximately two orders of magnitude larger than a typical laser mirror, making this level of flatness much more difficult to achieve. The surface quality of the mirrors was also specified with a scratch-dig not exceeding 80-50. This means that any scratch on the mirror should not be wider than 80 μm and any dig into the surface should not have a diameter larger than 0.5 mm. Again, this is a modest requirement by general 'small' optics standards where a scratch-dig of 40-20 would be typical. The glass slabs for the mirrors are made from BK7 glass. The specified flatness and scratch-dig are achieved by polishing the glass. This generates a considerable amount of heat, bringing with it a risk of cracking the BK7. This risk has been mitigated by having the thickness the glass be 40 mm. These thick mirrors also have the advantage of being less affected by gravitational bending in the mounts. This is particularly relevant for the M1, which

hangs facing downwards with the mirror held in place by the three adjustment screws. A thin, heavy piece of glass held at only three points like this would curve, leading to a distorted wavefront and affecting the resolution of the system. With a 40 mm thickness, however, this effect is negligible [81].

Two of the glass slabs for the mirrors are shown in Figure 4.6. After inspection, these slabs were coated at CERN. The coating for the mirrors was determined through a combination of simulation and tests to provide uniform reflectance of light around the scintillator's emission wavelength [82]. The layers are:

- An initial 10 nm layer of chromium applied to the glass substrate to ensure good adhesion of the remaining layers.
- A 100 nm aluminium layer for reflectance. Aluminium provides excellent reflectance around 545 nm.
- A final 185 nm layer of quartz to enhance the reflectance and prevent oxidation of the aluminium layer.

The inclusion of the quartz layer also allows the mirrors to be cleaned with pure ethanol, which would not be possible with an aluminium exterior. The coating was applied by evaporation; using an electron gun in the case of the quartz and chromium layers and thermally for the aluminium layer. The layers give the mirrors a reflectance of approximately 92% around the scintillator's emission peak. The three coated mirrors may be seen installed at AWAKE in Figure 4.7.

4.3.3. Mirror mounts

The spectrometer mirrors are unique and consequently require bespoke mirror mounts, which may be seen in Figure 4.7. Technical drawings of the assembled mirror mounts may be found in Refs. [83–85]. Each of the mounts has four sets of adjustment screws. Three screws in the back of the main mirror frame finely control the tip and tilt of the mirrors. A second set of screws in the sides of the frame press against the mirror keeping it central within the frame and add stability. Around the base of the frame are a third set of screws which may be adjusted to rotate the entire frame. A final fourth set allow for large scale adjustments to the tip and tilt of the assembly. The brass screws in the front of the frame which press against the mirror's coated surface are not used for movement but are instead spring-loaded, to hold the mirror steady whilst also allowing

(a) Glass for M1/M2 **(b)** Glass for M3

Figure 4.6.: Uncoated glass for the mirrors.

(a) The mounts for M1 and M2 at AWAKE. The camera lens is visible near the centre of M1 (black circle) via its reflection through M2 and M3.

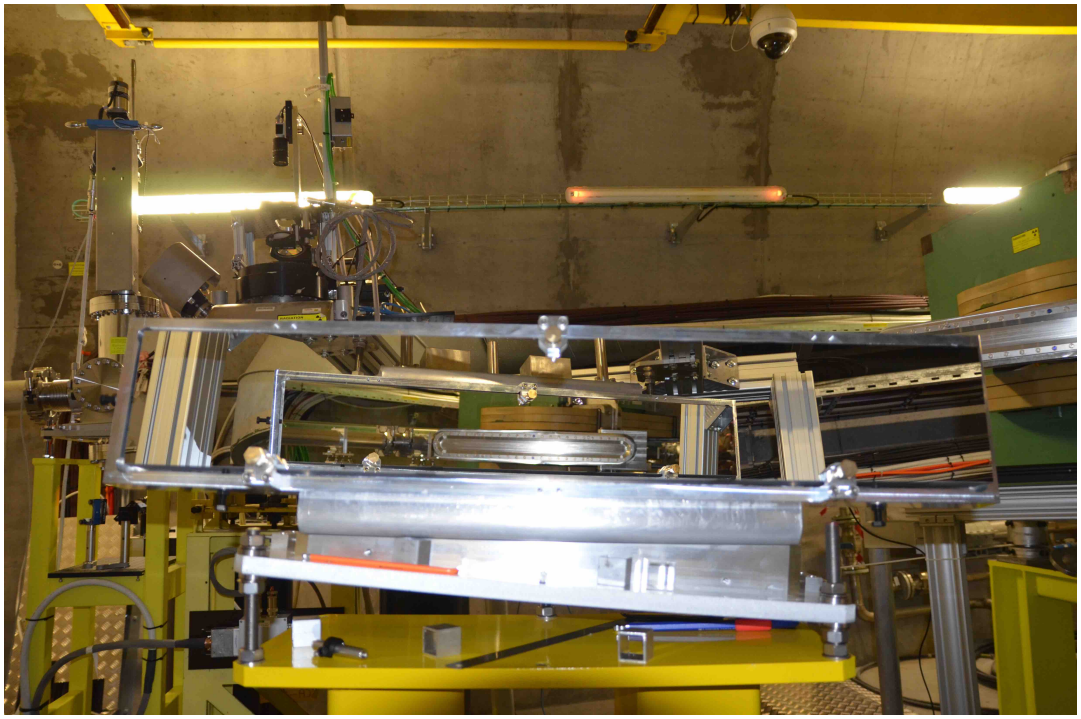

(b) M2 in its mount. The spectrometer vacuum window (before scintillator installation) is visible in the centre of M2 via M1.

Figure 4.7.: Spectrometer optics installed at AWAKE including the mirrors, adjustable mounts and fire window.

(c) M3 mounted inside the spectrometer darkroom.

(d) Fire window and protective housing with the side panel removed.

Figure 4.7.: Spectrometer optics installed at AWAKE including the mirrors, adjustable mounts and fire window (continued).

for adjustment. Maintaining a mirror's position over long periods of time is important to minimise the need to realign the line.

A key design feature of the mirror mounts is their sturdiness, such that they damp vibrations from the floor. This serves two purposes: it minimises drift in the mirrors over long time periods which necessitate realignments and it damps high frequency vibrations which could distort the wavefront of the signal and blur the images. The mirror most affected by vibrations is M1 due to the less rigid base and the fact that it hangs from the mount instead of sitting on it. Both of these features are necessary to allow the light path to go underneath the mirror and through TSG42 to M3. During the design of the mounts a measurement of the power spectral density (PSD) of vibrations from the ground at the locations of the mirrors was made. This PSD was combined with the transfer functions for the M1 mount, which were generated using ANSYS. The PSD and the transfer functions give the expected displacement of the mirror's centre of gravity. This analysis reveals that the motion of the mirrors is negligible at frequencies higher than 1 Hz [81]. This is important since the camera is typically exposed over time scales of at most $\mathcal{O}(1\,\mathrm{ms})$ and, as such, vibrational motion below approximately 100 Hz causes negligible distortion of the wavefront.

4.3.4. Fire window

The spectrometer's fourth large optic is a window, shown in Figure 4.7d, which covers a hole in the fire wall between TSG4 and TSG42. The fire window is between M2 and M3 on the optical line (see Figure 4.1) and is covered by an extension of the darkroom. This window, the need for which was realised late in the spectrometer's design process, is a $550 \times 200 \times 3\,\mathrm{mm}^3$ piece of BK7 glass. The transverse dimensions are dictated by the size of the image at the fire window's location and the thickness has been made as small as possible for a window of this size. The flatness of this thin window cannot be specified, however, as the heat generated during polishing would crack the glass. The uneven surface of the window causes wavefront distortion but it is unclear whether a thicker, flatter window would perform better [86]. To minimise any light loss due to the glass, the window is coated on the TSG42 side with a broadband antireflective coating giving the window a transmittance of >99.0% in the wavelength range $550 \pm 50\,\mathrm{nm}$. The effect of the fire window's necessary inclusion in the optical line will be discussed in Chapter 5.

4.4. Data acquisition and control

The camera's data acquisition (DAQ) and control are handled by a FESA (Front-End Software Architecture) [87] server. This server accesses functions from a library based on the Andor SDK to directly read and set parameters on the camera. Some examples of parameters which are acquired/set through the FESA server are:

- Target temperature.
- MCP Gain.
- Trigger threshold.
- DDG gate width.

When an image is acquired by the camera it is automatically held in the FESA server until a new image is taken. During AWAKE experimental running this image data is acquired by the AWAKE event builder, a DAQ software which takes readings from each FESA server associated with the experiment and stores them together in a single file. The size of these event files is 60 MB and approximately 1000 are taken during a typical day of running at AWAKE. The experiment receives a few weeks of beam time per year and produces 5–10 TB of event data annually.

Acquisition of an image with the camera may be initiated by an internal or external trigger. Internal triggering is typically used for calibration. During experimental running, an external trigger is provided by a pulse which is synchronous with proton extraction to AWAKE. External triggering is discussed further in Chapter 5.

The FESA server runs on a front end computer (FEC) in the racks close to the camera (Figure 4.1, far right). The racks also house a 500 MHz oscilloscope (Teledyne LeCroy WaveJet 354T) used to diagnose the camera and trigger signals. The camera produces three signals which are relevant to understand the state of the acquisition:

Arm A 5 V TTL signal to indicate when system is ready to accept external triggers.

Fire A 5 V TTL signal for the beginning and end of a CCD exposure.

Gate monitor An AC coupling giving the photocathode's On/Off switching.

For a given acquisition setting (exposure, gate width, gate delay) the position of these signals relative to the trigger is known and may be verified with the oscilloscope to ensure

correct functioning of the camera. These checks were performed before each AWAKE experimental run.

The low data rate at AWAKE of approximately one extraction event per 30 s means that the acquisition and readout for the camera are performed in negligible time. The camera can be internally triggered at the much higher rate of ~ 0.83 Hz without issues.

The power supply and the motorised rail for the calibration lamp are also both controlled by FESA servers. The former allows the voltage provided to the lamp to be set in the range 0–5 V. The latter provides millimetre level control of the lamp's position. Both FESA servers are hosted on FECs further down the TSG4 tunnel, beyond the right side of Figure 2.3 (landscape view).

Chapter 5.

Calibration of the spectrometer

This chapter summarises a variety of tests performed with the various components of the spectrometer to characterise their performance. The alignment of the optical line is detailed in Section 5.1. The camera's response at various width and gain values is assessed in Section 5.2. The real resolution of the optical line is determined and compared to its design specification in Section 5.3. The decay of the scintillator is analysed and a measurement of its charge response is presented in Section 5.4.

5.1. Alignment

The spectrometer's mirror mounts were installed and aligned in their design positions by the CERN survey team. The fine alignment of the optics was conducted using a reference laser. The laser was installed on a microrotation stage and aligned through two irises at 0°. The stage allows adjustments in steps of one arcminute. This setup was installed on the calibration lamp's mechanical rail and aligned such that the laser was normal to the vertical centre of the plane of the scintillator, the setup is shown in Figure 5.1. The height of M1 was adjusted until the laser at the horizontal centre of the scintillator was central on M1. The tip, tilt and rotation of the mirrors were then adjusted in order along the line until the laser line was centred on each mirror and the centre of the lens.

A camera image of the scintillator after the final alignment is shown in in Figure 5.2a. The image is offset slightly in the vertical due to the adjustment of the camera's position relative to the lens. This was done to move the scintillator away from a collection of damaged pixels near the vertical centre of the CCD. The dark spots in the image are reflections of ambient light from the brass screws on the fronts of the mirror mounts.

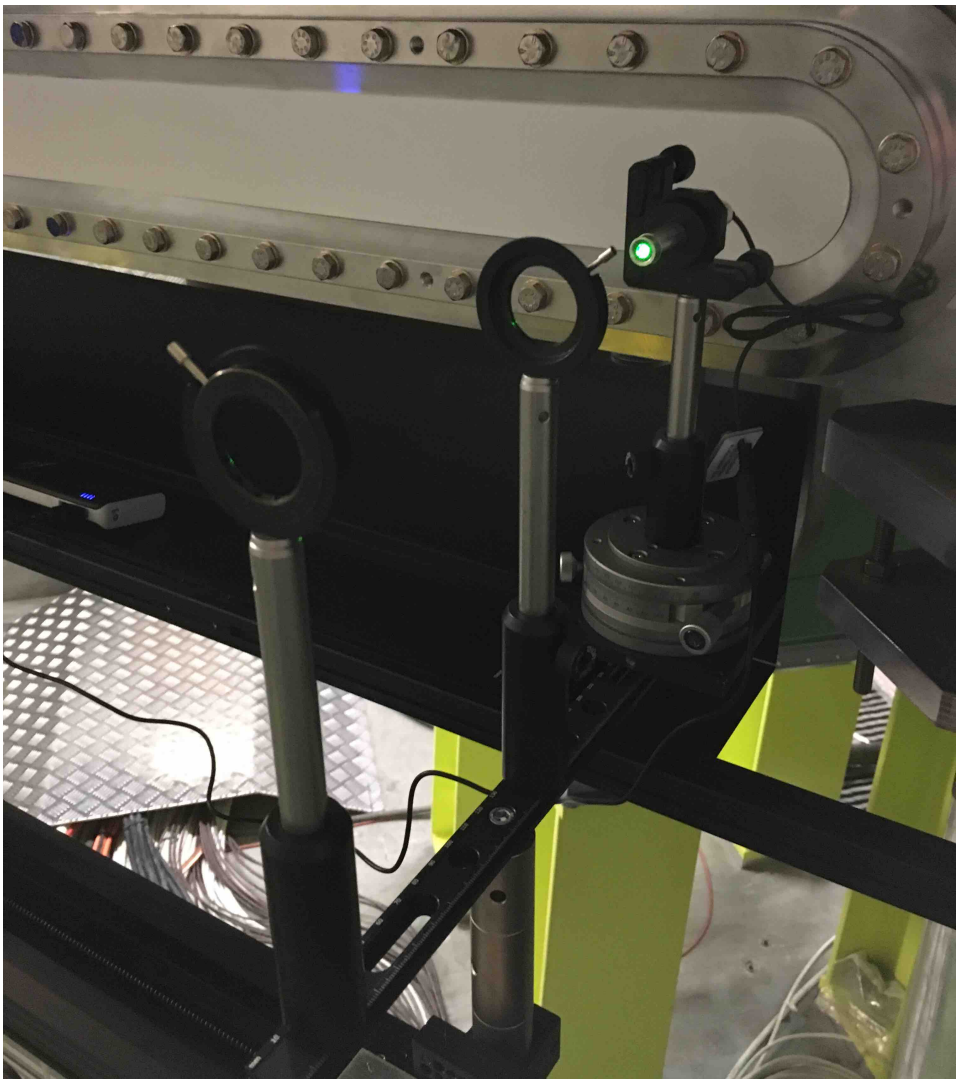

Figure 5.1.: Laser setup used in the alignment of the optical line. The laser is aligned normal to the plane of the scintillator and sits on a rotation stage with 0° passing through both irises. The setup is installed at the height of the scintillator's vertical centre.

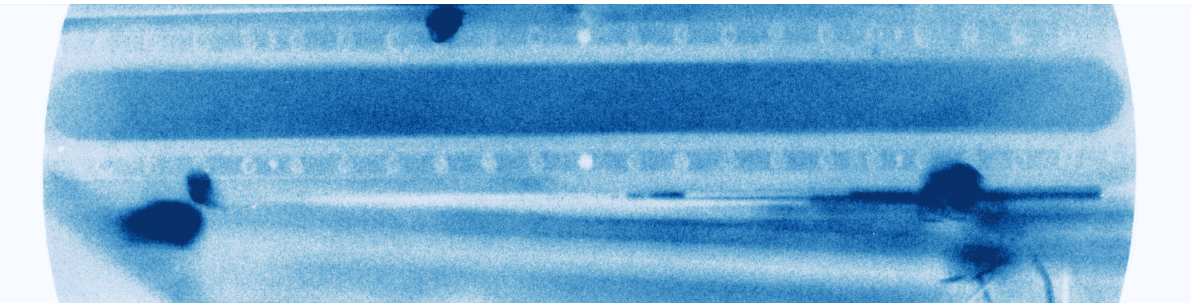

(a) Scintillator image

(b) Scintillator mask

Figure 5.2.: Image of the scintillator installed at AWAKE and the scintillator image mask defined for data analysis. The mask is defined for the image after rotation through -0.6°.

The horizontal axis of the scintillator is not flat with respect to the CCD, lying at an angle of 0.6°. This was corrected in analyses by rotating the image back by this amount. Spectrometer analyses rely only on the image of the scintillator and, as such, a mask, shown in Figure 5.2b, was defined to isolate this part of the image. This mask passes only pixels with the white obround, which has a width of 1850 pixels and a height of 120 pixels. Due to the image's finite resolution, determining the edges of the scintillator can only be done up to an accuracy of approximately 4 pixels, giving an uncertainty in the total width. This combines with the 0.5 mm machining uncertainty in the 997 mm width of the scintillator [88] to give an effective pixel length of 0.5389 ± 0.0012 mm.

5.2. Camera calibration

5.2.1. Image noise

The spectrometer's camera has a 16-bit pixel depth. When an image is acquired, the CCD count for each pixel receives contribution from external sources, that is, light

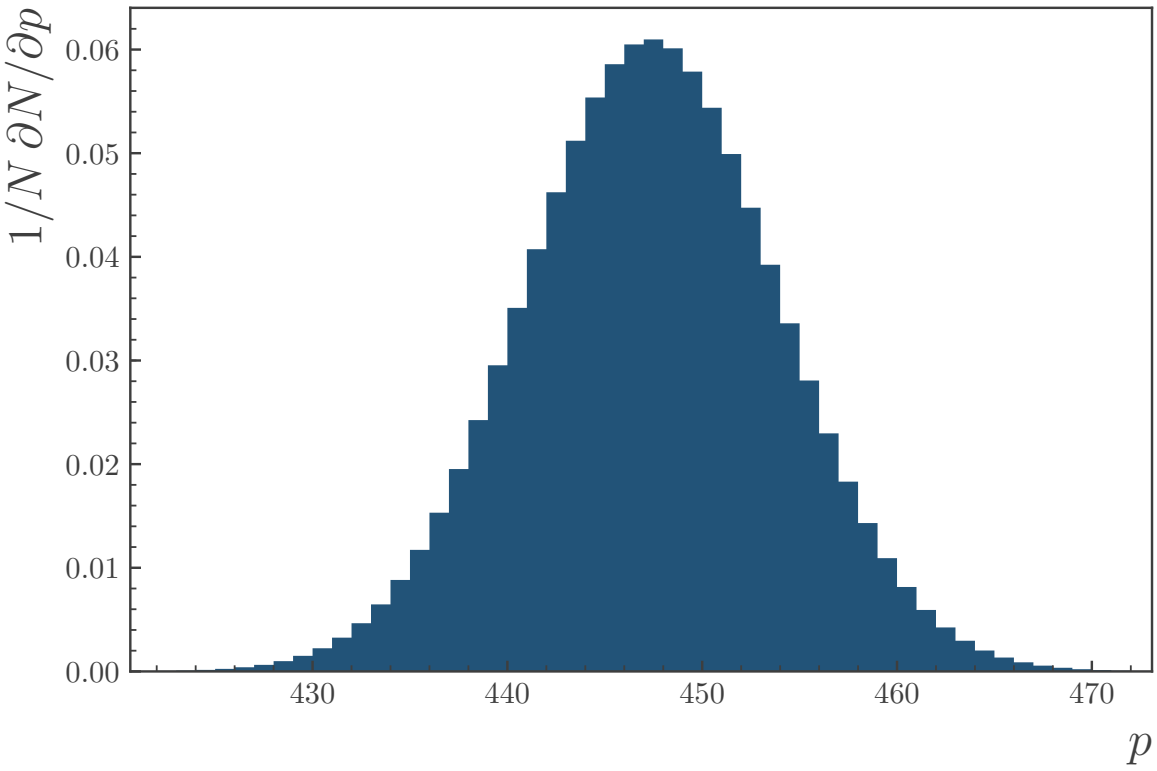

Figure 5.3.: Histogram of CCD pixel counts p in dark images at -30°C. The pixel counts are from the scintillator area in 515 images, a total of $\sim 10^8$ counts. The distribution is a Gaussian with a mean of 446.9 and a standard deviation of 6.6.

incident upon the camera, and internal sources such as thermal noise on the CCD. The latter may estimated by covering the camera and acquiring images with a gate width of 0 s. A histogram of the CCD counts p for the scintillator pixels (those within the mask in Figure 5.2b) is shown in Figure 5.3. The data comes from 515 images acquired at -30°C under the conditions described above. The histogram is well modelled by a Gaussian with a mean of 446.9 and a standard deviation of 6.6. The correlation between the pixel counts is negligible. All images taken with the camera have this contribution, independent of the acquisition settings, and as such it is subtracted in any analysis, with the appropriate uncertainty propagated.

5.2.2. Width corrections

The complex working of the intensifier in the spectrometer's camera has the effect of making the relationship between CCD counts and gate width non-linear. That is, extending the gate width by a factor of, for example, 10 whilst imaging a constant light

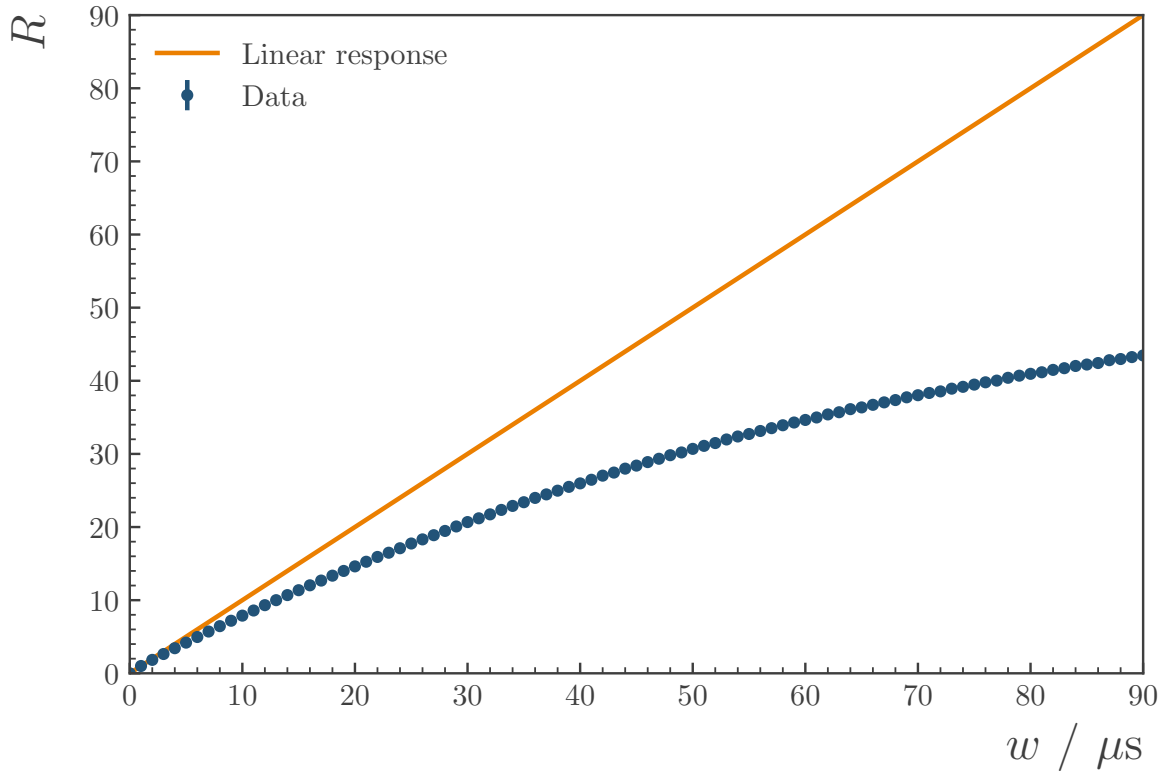

Figure 5.4.: Relative camera response R to a constant light source at different camera gate widths w. The image are background-subtracted and the responses are normalised to the 1 μs gate width response.

source does not increase the counts above the background by the same factor. This is illustrated in Figure 5.4, which shows the relative signal R against the gate width w, normalised to the 1 μs gate. These correction factors are relevant for the analysis in Section 5.4.2.

5.2.3. Gain corrections

A number of gain values for the camera have been provided by Andor and are listed in Table 5.1. For better precision at lower gain values the relationship is also measured in a similar manner to the width described above. The results are shown in Figure 5.5. The results include data from seven different width settings as no one width could be scanned over all the gains without saturating the CCD. The scans are corrected by overlapping the gain ranges and applying a correction. The measured values deviate slightly from the values provided by Andor at high gains ($g > 2000$) and, because of the uncertainty associated with these width corrections, Andor's values are used.

MCP gain	0	500	1000	1500	2000	2500	3000	3500	4000	4095
Relative gain	1	3	8	22	56	142	312	669	1333	1442

Table 5.1.: Relative gain at different MCP gain settings, provided by Andor.

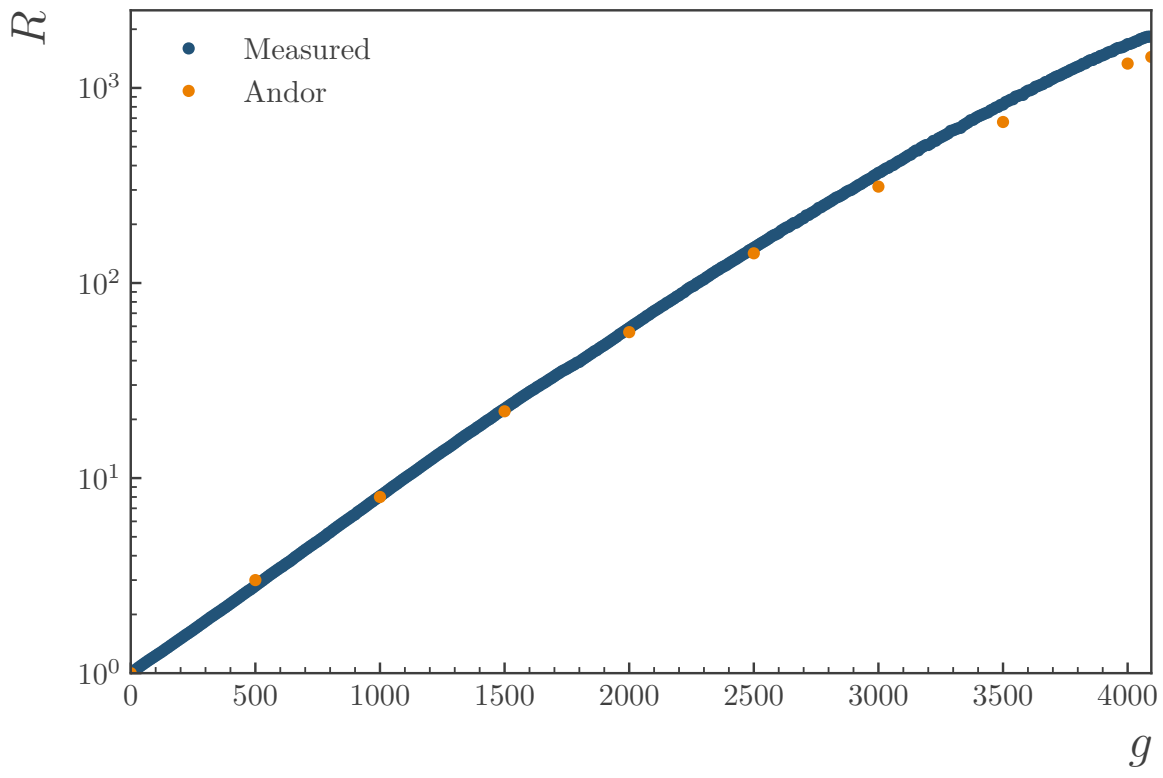

Figure 5.5.: Relative camera response R to a constant light source at different camera MCP gains g. The image are background-subtracted and the responses are normalised to the MCP setting of 0. The points from Table 5.1, labelled 'Andor', are shown in orange.

5.2.4. Triggering

Prior to July 2018, the spectrometer camera was triggered by a pulse generated by the SPS timing system, a set number of revolutions before extraction to AWAKE. This trigger was used in the May 2018 run but found to have a jitter of approximately 0.4 ms. Up to this uncertainty, the proton bunch was estimated to arrive 1.4 ms after the trigger. To maintain a consistent scintillator response and not risk missing the signal the DDG gate width was set to 4 ms and the delay relative to the trigger was set to 0.5 ms. After the May run, the trigger was replaced by one linked to the AWAKE laser timing system, which provided a much more precise response. To the nearest microsecond, this trigger arrived 101.036 ms before the proton bunch, and the delay and gate width were set to 101.2 ms and 0.5 ms respectively.

5.3. Optical line calibration

5.3.1. Image resolution

An image of the spectrometer's calibration lamp without the calibration mask is shown in Figure 5.6. The lamp, which should be uniform on the percent level per design specifications, has a strong horizontal variation, shown clearly by the vertical projection of the image. The centre of the lamp is approximately 65% as bright as the edges. A much weaker brightness variation in the vertical axis can be seen in the horizontal projection, with the lower half of the lamp slightly brighter than the upper half.

This variation in the lamp's brightness must be accounted for in the resolution analysis. Consider the series of bars in the calibration mask shown in Figure 4.4. Perfectly resolving a square impulse such as the bars requires sensitivity to an infinite number of spatial frequencies (cf. the Fourier transform of a square wave). As the higher frequency components are lost by, for example, distortion of the light's wavefront, the square impulse blurs out. Examples of this blurring effect can be seen in Figure 5.7 which shows images of a section of the optical mask in various setups. The images are background subtracted and the vertical projections are shown below the bars. The blurring may be defined [89] by calculating the modulation for each bar

$$\text{Modulation} \equiv \frac{\mathcal{I}_{\max} - \mathcal{I}_{\min}}{\mathcal{I}_{\max} + \mathcal{I}_{\min}}\,, \tag{5.1}$$

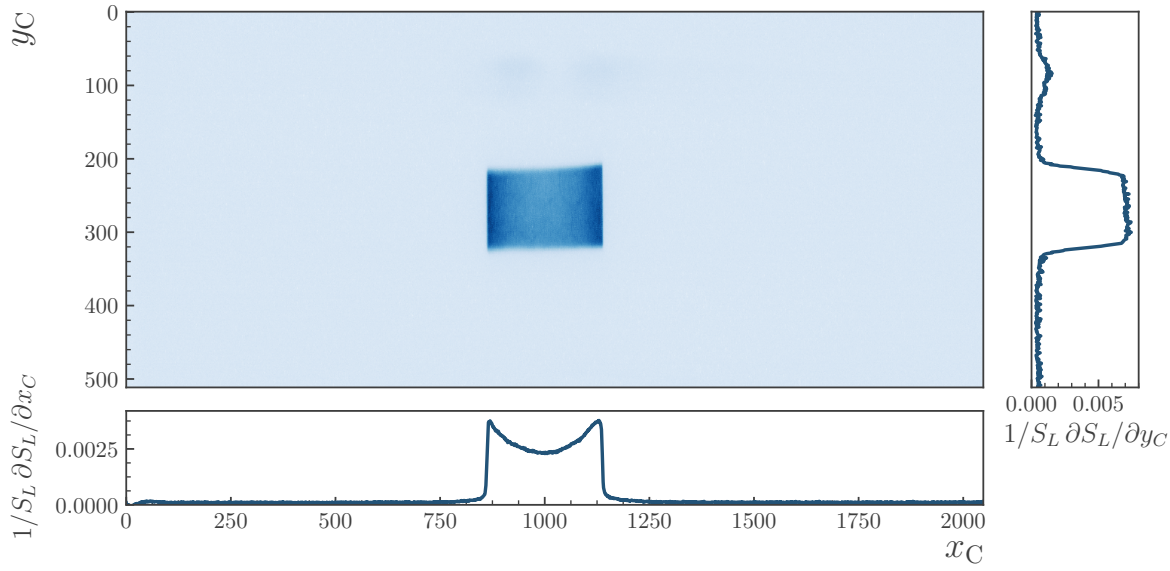

Figure 5.6.: Image and projections of the unmasked calibration lamp light S_L.

where $\mathcal{I}_{\max}$ and $\mathcal{I}_{\min}$ are, respectively, the maximum and minimum projection values for each bar in the mask. The locations of the maxima and minima are indicated by dotted grey lines in the lower plots in Figure 5.7. The modulation transfer function (MTF) is defined as the ratio of this modulation to the modulation at zero spatial frequency. Specifically, this is Eq. (5.1) with the maximum brightness of the lamp as $\mathcal{I}_{\max}$ and the background, which is zero for well subtracted images, as $\mathcal{I}_{\min}$. As discussed above, the maximum brightness varies across the lamp, complicating the calculation. The maximum is estimated using an unmasked part of the lamp and is shown by the blue line in the projections in Figure 5.7. The minimum is estimated using a well masked part of the lamp.

The images in Figure 5.7 correspond to four specific setups:

Focused, fire window out The lens is focused to maximise the sharpness of the bars in calibration mask and the fire window is not installed.

Unfocused, fire window out The lens is not properly focused and the fire window is not installed.

Focused, fire window in The lens is focused to maximise the sharpness of the bars in the calibration mask and the fire window is installed in the fire wall.

Alternative focus, fire window in The lens is focused close to the maximum sharpness of the bars in the calibration mask and the fire window is installed in the fire wall.

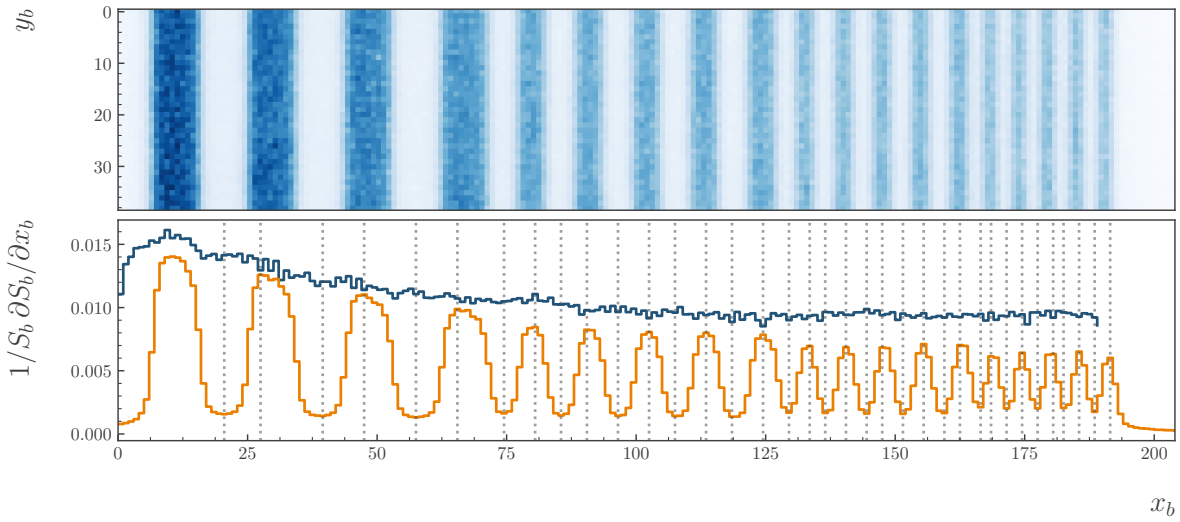

(a) Focused, fire window out

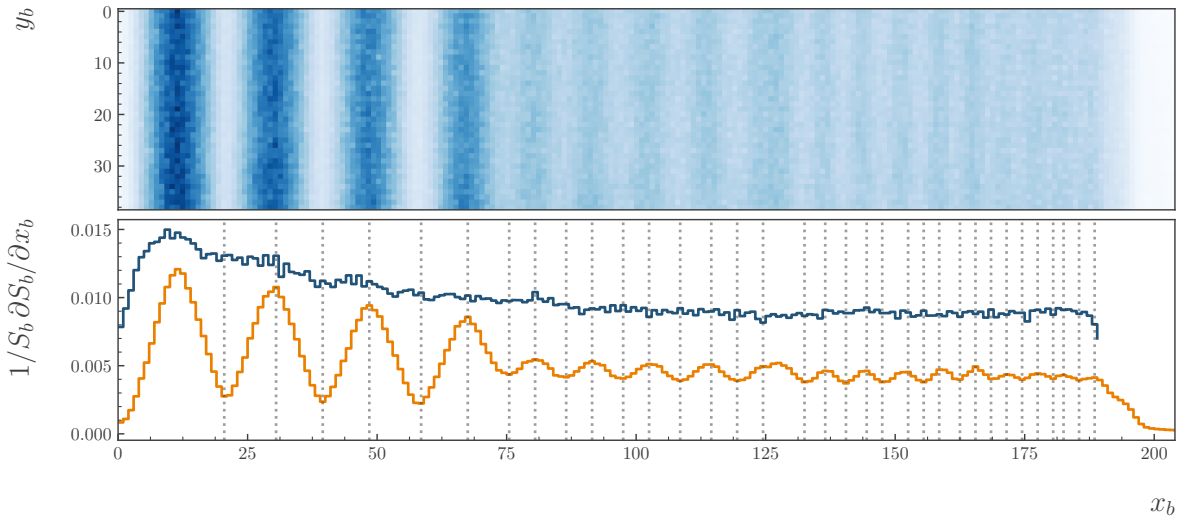

(b) Unfocused, fire window out

Figure 5.7.: Calibration mask images and projections for different optical setups. The top plot for each setup shows a background-subtracted image of part of the calibration mask. The bottom plot shows the vertical projection (orange) and an estimate of the lamp's true brightness (blue) both normalised to a sum over the whole image, S_b. The minima and maxima for each line pair are indicated by dashed grey lines.

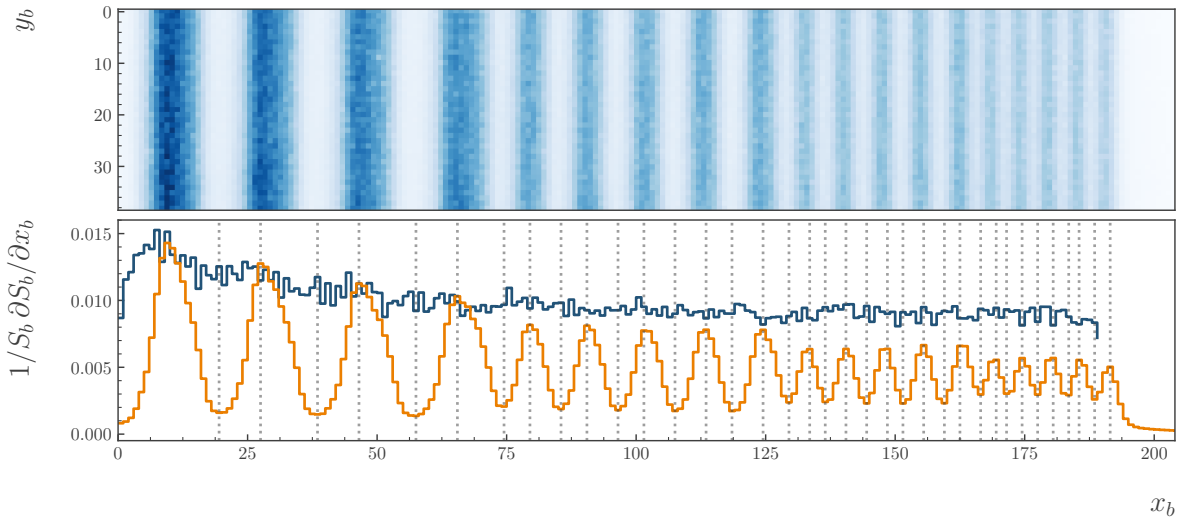

(c) Focused, fire window in

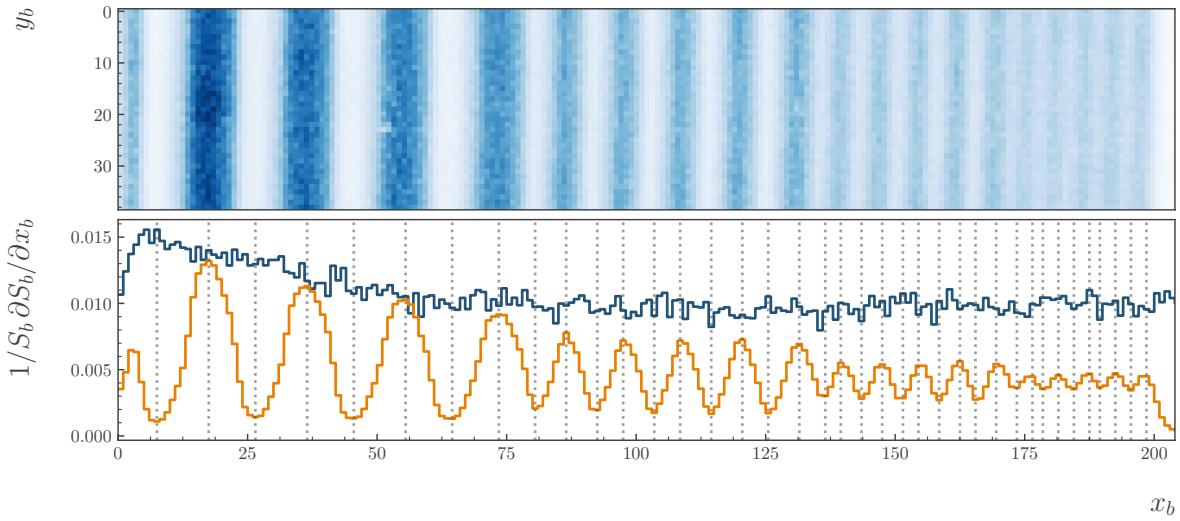

(d) Alternative focus, fire window in

Figure 5.7.: Calibration mask images and projections for different optical setups (continued). The top plot for each setup shows a background-subtracted image of part of the calibration mask. The bottom plot shows the vertical projection (orange) and an estimate of the lamp's true brightness (blue) both normalised to a sum over the whole image, S_b. The minima and maxima for each line pair are indicated by dashed grey lines.

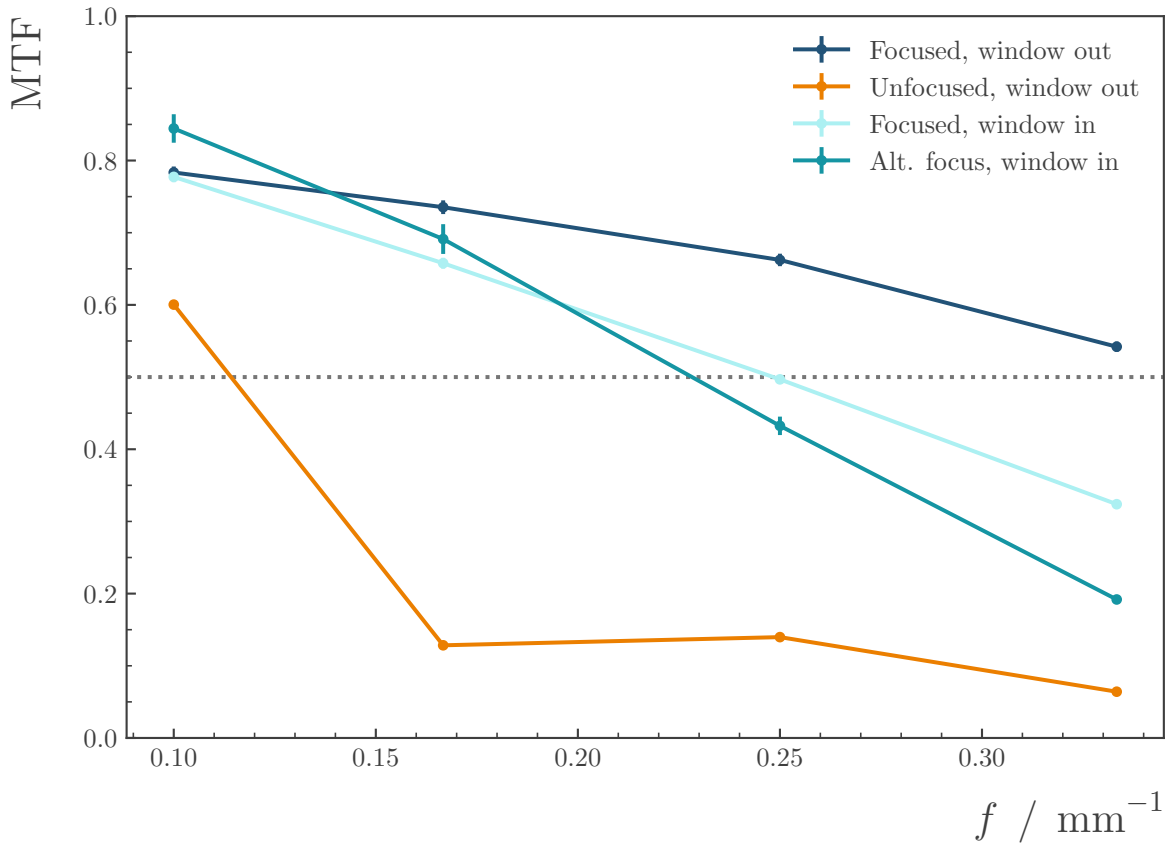

Figure 5.8.: Modulation transfer function (MTF) for each optical setup in Figure 5.7. The spatial frequency f is in line pairs per millimetre, such that, for example, the 5 mm bars in the mask correspond to $f = 0.1\,\mathrm{mm}^{-1}$.

Additionally, the calibration mask was installed in a different position on the surface of the lamp, as can be seen by comparing Figure 5.7c and Figure 5.7d.

The MTFs for these configurations are shown in Figure 5.8. The error bars given are a combination in quadrature of the statistical uncertainty (there are multiple bars for each spatial frequency) and the systematic uncertainty in the estimation of the background and the bright part of the lamp. When correctly focused, the optical line without the fire window installed achieves its design goal of 1.5 mm resolution with an MTF > 0.5 at this spatial frequency ($0.33\,\mathrm{mm}^{-1}$). The inclusion of the fire window degrades this, with the MTF falling below 0.5 close to $0.25\,\mathrm{mm}^{-1}$, giving a resolution of approximately 2 mm. The alternative focus shows an example of how adjusting the lens can improve resolution at some spatial frequencies whilst degrading it at others. The MTF for the unfocused optics is predictably poor, emphasising the importance of keeping the system well focused.

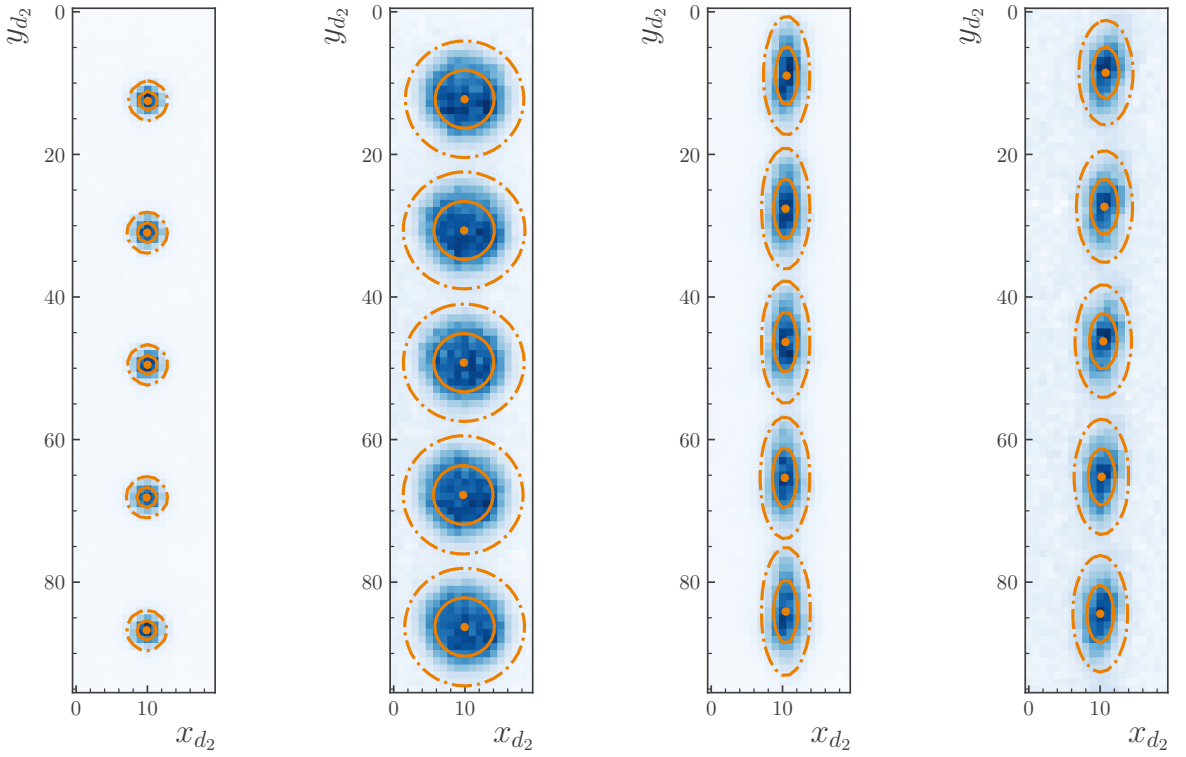

(a) Focused, fire window out

(b) Unfocused, fire window out

(c) Focused, fire window in

(d) Alternative focus, fire window in

Figure 5.9.: Calibration mask 2 mm dots for a variety of focusing conditions. The dots are fitted together with a sum of five 2D Gaussians, the mean (orange point), 1σ (solid) and 2σ (dot-dashed) lines are shown for each. The fire window's effect on the resolution, particularly in the vertical axis, is clear.

The vertical bars in the mask give only the resolution in the horizontal axis. While this is the more relevant axis, since it directly affects the spectrometer's energy resolution, the resolution in the vertical is relevant to future studies of the electron bunch emittance using the spectrometer's quadrupoles [90]. This can be examined using the dots in the calibration mask (Figure 4.4, left side), which are series of 1 mm and 2 mm holes in the vertical direction. The blurring effect of the optical line smears the image of the dots into two dimensional Gaussian intensity profiles about the dots' centres. This is shown in Figure 5.9 which shows the image of the 2 mm dots, fitted with Gaussian intensity distributions, for each of the optical setups described above. The horizontal projections of these images are shown in Figure 5.10. It's clear in these projections that the fit gives a good description of the dots' widths. The corresponding images and projections for the 1 mm dots are shown in Figure 5.11 and Figure 5.12.

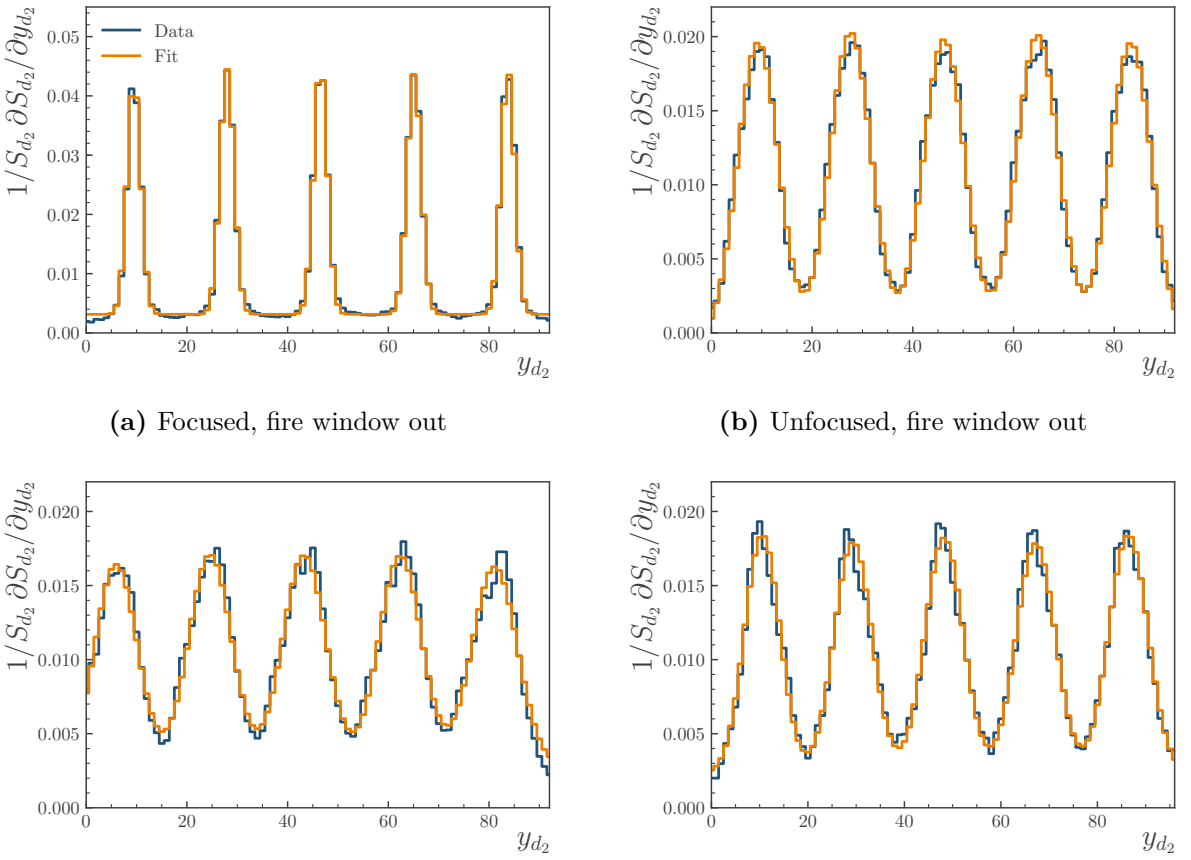

(a) Focused, fire window out

(b) Unfocused, fire window out

(c) Focused, fire window in

(d) Alternative focus, fire window in

Figure 5.10.: Horizontal projections of the 2 mm dots on the calibration mask. The projections of both the data and the fit from Figure 5.9 are shown. The fits describes the data well. For each projection S_{d_2} is defined as the sum over the corresponding image in Figure 5.9.

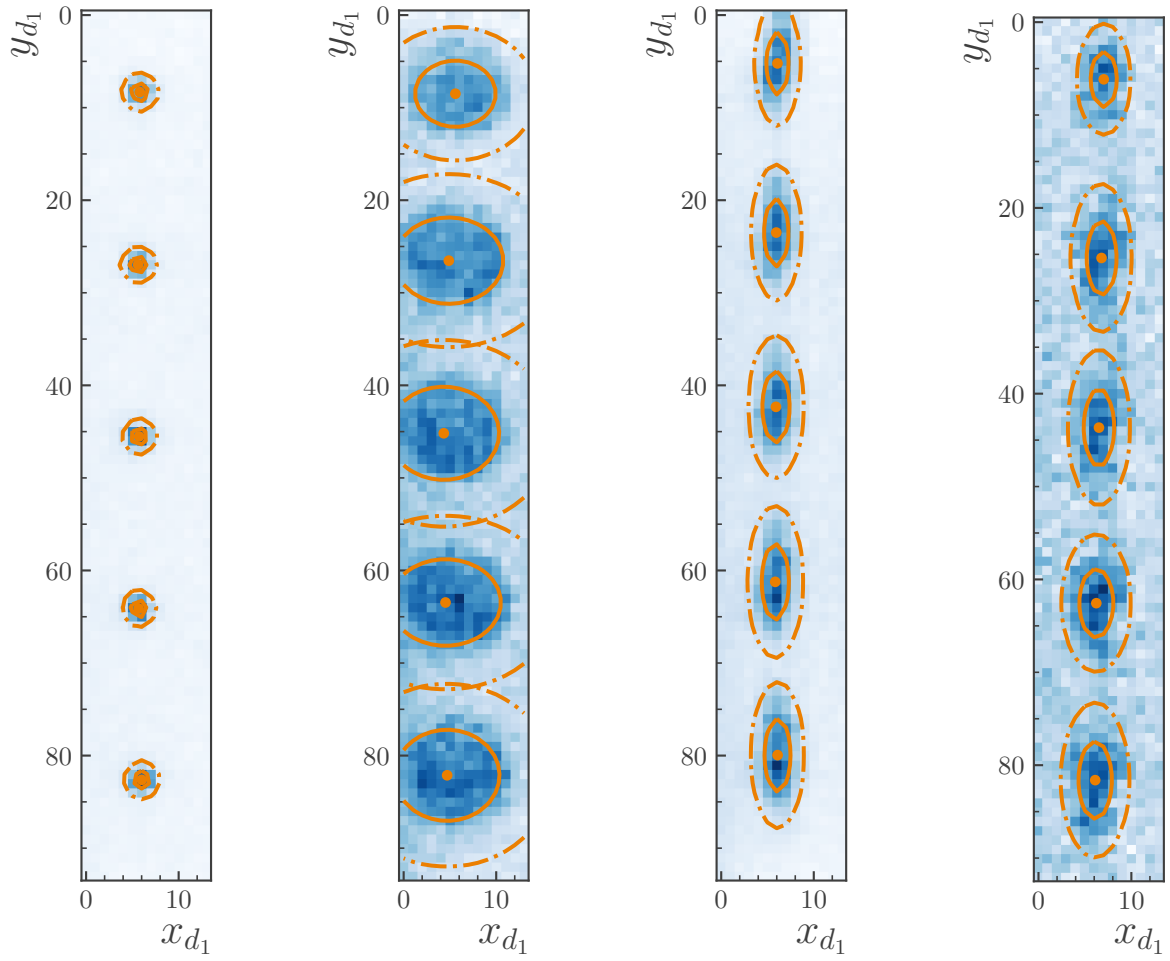

(a) Focused, fire window out

(b) Unfocused, fire window out

(c) Focused, fire window in

(d) Alternative focus, fire window in

Figure 5.11.: Calibration mask 1 mm dots for a variety of focusing conditions. The dots are fitted together with a sum of five 2D Gaussians, the mean (orange point), 1σ (solid) and 2σ (dot-dashed) lines are shown for each.

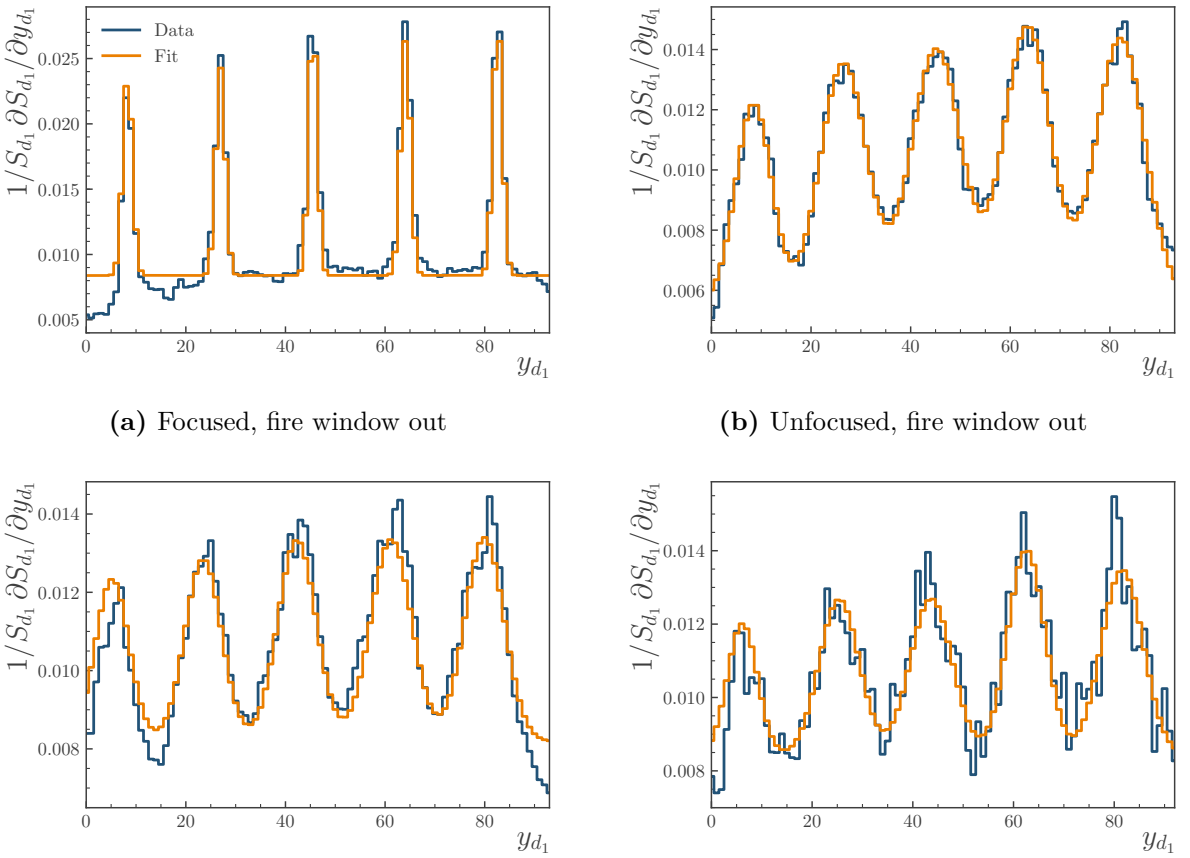

(a) Focused, fire window out

(b) Unfocused, fire window out

(c) Focused, fire window in

(d) Alternative focus, fire window in

Figure 5.12.: Horizontal projections of the 1 mm dots on the calibration mask. The projections of both the data and the fit from Figure 5.11 are shown. The fits, whilst not as accurate as for the 2 mm images, capture the widths of the dot signals well. For each projection S_{d_1} is defined as the sum over the corresponding image in Figure 5.11.

Setup	1 mm dots			
	σ_x	σ_y	FWHM$_x$ / mm	FWHM$_y$ / mm
Focused, window out	0.916 ± 0.016	0.961 ± 0.015	$1.163 \pm 0.021^{\text{stat.}} \pm 0.003^{\text{syst.}}$	$1.219 \pm 0.019^{\text{stat.}} \pm 0.003^{\text{syst.}}$
Unfocused, window out	5.57 ± 0.28	4.58 ± 0.23	$7.08 \pm 0.35^{\text{stat.}} \pm 0.02^{\text{syst.}}$	$5.81 \pm 0.29^{\text{stat.}} \pm 0.01^{\text{syst.}}$
Focused, window in	1.365 ± 0.049	3.78 ± 0.11	$1.733 \pm 0.063^{\text{stat.}} \pm 0.003^{\text{syst.}}$	$4.80 \pm 0.14^{\text{stat.}} \pm 0.01^{\text{syst.}}$
Alt. focus, window in	1.661 ± 0.069	3.79 ± 0.20	$2.107 \pm 0.088^{\text{stat.}} \pm 0.004^{\text{syst.}}$	$4.81 \pm 0.25^{\text{stat.}} \pm 0.01^{\text{syst.}}$

Setup	2 mm dots			
	σ_x	σ_y	FWHM$_x$ / mm	FWHM$_y$ / mm
Focused, window out	1.359 ± 0.014	1.384 ± 0.010	$1.725 \pm 0.018^{\text{stat.}} \pm 0.004^{\text{syst.}}$	$1.756 \pm 0.012^{\text{stat.}} \pm 0.004^{\text{syst.}}$
Unfocused, window out	4.235 ± 0.017	4.128 ± 0.011	$5.374 \pm 0.021^{\text{stat.}} \pm 0.012^{\text{syst.}}$	$5.239 \pm 0.014^{\text{stat.}} \pm 0.012^{\text{syst.}}$
Focused, window in	1.658 ± 0.021	4.297 ± 0.047	$2.104 \pm 0.027^{\text{stat.}} \pm 0.004^{\text{syst.}}$	$5.453 \pm 0.060^{\text{stat.}} \pm 0.012^{\text{syst.}}$
Alt. focus, window in	1.897 ± 0.011	3.914 ± 0.062	$2.408 \pm 0.014^{\text{stat.}} \pm 0.005^{\text{syst.}}$	$4.967 \pm 0.080^{\text{stat.}} \pm 0.011^{\text{syst.}}$

Table 5.2.: Mean and mean error of the fitted Gaussian sigmas in Figure 5.9 and Figure 5.11. The width values for the sigmas are given in pixels. The values of the FWHMs have a statistical uncertainty from the mean error and a systematic uncertainty from the definition of the effective pixel width, as discussed in Section 5.1.

The mean of the fitted sigmas of the Gaussians for each case are given in Table 5.2. Properly focused, the optical system without the fire window resolves the dots well in both axes. The introduction of the fire window has an interesting effect. In the horizontal axis the resolution remains reasonably good, with the FWHM of a 2 mm dot rising from $1.725 \pm 0.018^{\text{stat.}} \pm 0.004^{\text{syst.}}$ without the window installed to $2.104 \pm 0.027^{\text{stat.}} \pm 0.004^{\text{syst.}}$ with it. The vertical resolution, however, is significantly affected, with the width increasing by a factor of three. This value exceeds the vertical width for the unfocused setup with no fire window. The reason for this resolution loss is likely down to the unspecified flatness of the fire window. A simple random flatness variation across the window's surface is unlikely to be sufficient to cause this, however, and the effect most likely comes from an overall warping of the window [86]. The window is fixed at the edges by its mounting in the frame meaning the position of maximum displacement relative to a flat plane is likely to be in its centre. For a given displacement at this point, the curvature of the glass in the vertical has to be a factor 2.75 greater than in the horizontal due to the transverse dimensions of the fire window: $550 \times 200\,\text{mm}^2$. This larger curvature leads to increased wavefront distortion and resolution loss in the vertical axis.

As discussed in Section 4.3.4, the inclusion of the fire wall window in the optical line was unavoidable. Unfortunately, its negative effect on the spectrometer's optical resolution is clear. While the impact in the horizontal axis, and therefore on the energy measurement, is only to degrade the resolution from 1.5 mm to approximately 2 mm, the impact in the vertical axis is much worse, seriously constraining the effectiveness of the spectrometer's proposed emittance measurements.

5.3.2. Vignetting

The spectrometer's optical system does not capture and record all of the scintillation light produced during an event. This is due to the finite size of the spectrometer's optics and the angular emission profile of the scintillator. This results in a gradual fading of the image towards the periphery, an effect known as vignetting [89]. This process is highly relevant to the spectrometer as it affects the number of CCD counts which are generated by a unit charge at any given point on the screen. The limited vertical range of the scintillator (see Figure 5.2) means that vignetting in this axis is negligible. Vignetting as a function of ξ, however, is not negligible and is characterised using the calibration lamp. The lamp is scanned in steps across the surface of the scintillator and the brightness of a part of it (the 2 mm dots, for example) is measured at each location. The images are background-subtracted and normalised relative to the point $\xi = 0.84\,\mathrm{m}$. The choice of normalisation point is arbitrary and this point is chosen because it's the point at which incoming accelerated electrons are normally incident on the screen.

The vignetting results are shown in Figure 5.13. The mean at each measured point is shown along with the mean error. Between the measured points the results are linearly interpolated and at the edges they are extrapolated using a linear fit through the previous two points. The extrapolation is necessary because no part of the lamp can be imaged at all ξ values due to its size and the limits of the motorised rail. The broad shape of the curve is as expected and the noisy nature of it is interpreted as being due to the mirror mounts, which scatter the lamp light.

5.4. Scintillator calibration

5.4.1. Incident angle

The scintillator's emission is proportional to the energy deposited in it by the accelerated electrons (or other radiation). This deposited energy is proportional to the electron's path length through the scintillator, which varies with angle of incidence θ [91]. Electrons incident at oblique angles will generate a signal which is boosted by the cosine of the incident angle. That is, the correction to the scintillator signal is

$$\mathcal{A} = \cos\left|\frac{\pi}{2} - \theta\right| . \tag{5.2}$$

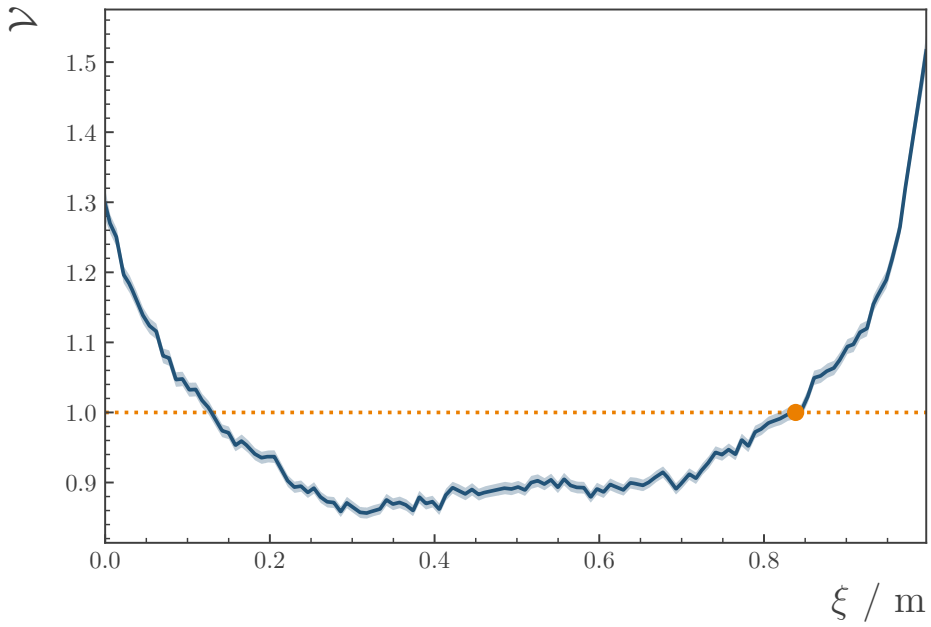

Figure 5.13.: Vignetting correction $\mathcal{V}$ determined by the calibration lamp scan. The correction is the inverse of the relative brightness of a given spot on the lamp. The normalisation point and $\xi = 0.84\,\mathrm{m}$ is shown in orange. The uncertainty is shown as a band around the correction.

The spectrometer's nominal incident angle range, defined by the tracking simulations discussed in Section 3.3, is shown in Figure 5.14. This is defined up to the 0.01° uncertainty in the scintillator's angle. The validity of the correction factor is assumed, rather than measured, since it was not possible to scan a beam of well known charge across the scintillator's surface.

5.4.2. Scintillator decay

Protons propagate through AWAKE and produce radiation which is incident on the scintillator. This occurs on nanosecond time scales, after which, the scintillator starts to glow. The intensity of the scintillator emission increases from zero to a maximum and then decays in an exponential manner. As such, when imaging the scintillator, the gate delay relative to the proton extraction and the gate width will both affect the measured intensity of the scintillator emission. If the scintillator's temporal emission profile is known then this difference is calculable.

When screens such as the BTVs are inserted into the AWAKE beamline the radiation incident upon the scintillator and, hence, the scintillator signal are proportional to

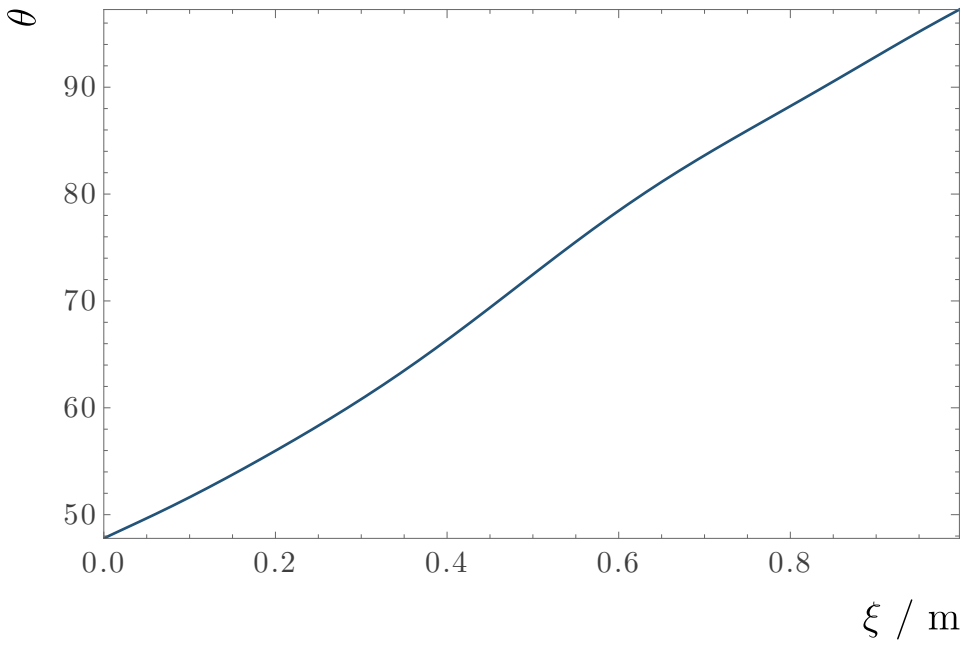

Figure 5.14.: Nominal electron incident angle at the scintillator. The angles, given in degrees, are determined by a tracking simulation.

the proton bunch population. The proton bunch population is always $\mathcal{O}(10^{11})$ but varies considerably shot-to-shot. It is measured by beam current transformers along the AWAKE line up to an uncertainty of 2×10^9 protons per bunch [92]. The emission profile is found by acquiring images for a number of events over a series of gate delays. By taking the background-subtracted sum over the scintillator and fitting it with a linear function with an intercept of zero to the proton bunch population, the relative emission of the scintillator at the different delays can be found.

The results of the scan are shown in Figure 5.15. The data have been corrected to a gate width of 1 μs and normalised relative to the first point, the statistical uncertainty is the uncertainty of the fit coefficient. The scan was performed over three days in September 2018 during self-modulation physics running and, therefore, the proton bunch conditions were not completely constant over longer times. As such, a 1% systematic uncertainty has been added to the coefficients. This was estimated by retaking data for one of the delay points periodically and comparing the coefficients. An exponential function was fit to the data with delays greater than 163.7 μs. The scintillator emission very quickly reaches its maximum brightness before decaying away, with the exponential form describing the data well after approximately 200 μs. This exponential function has a decay time (half-life) of 379 ± 1 μs.

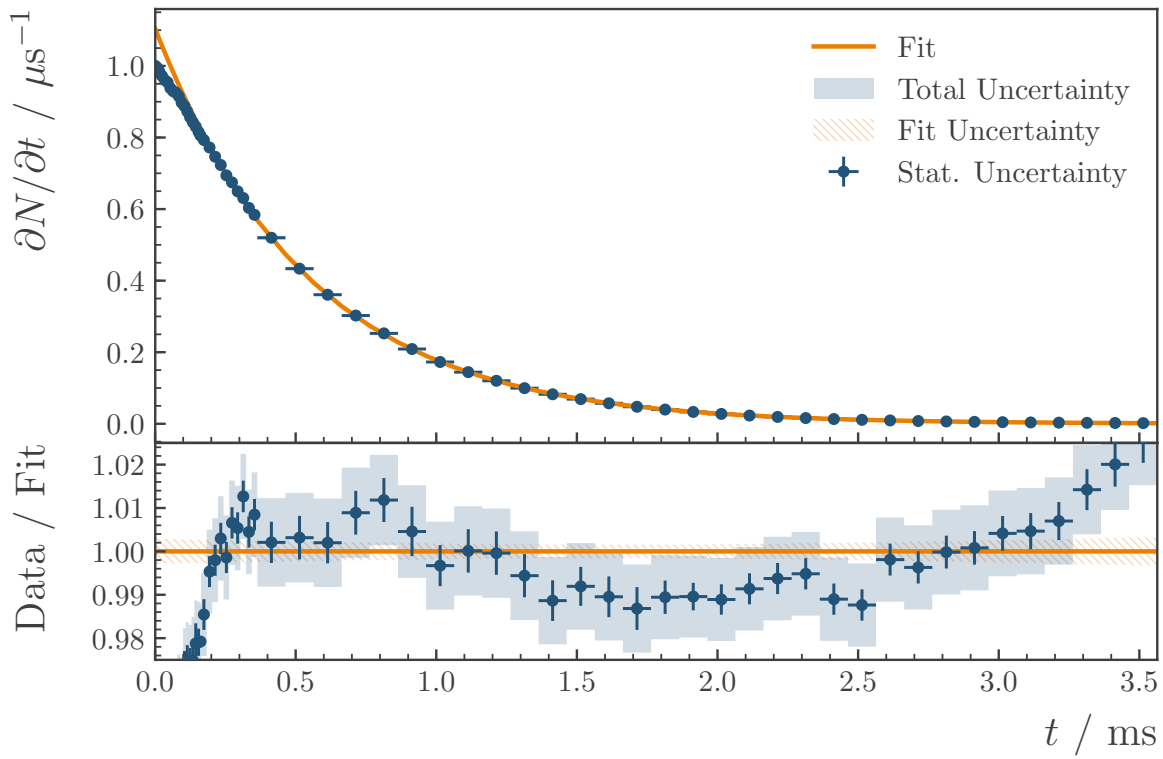

Figure 5.15.: Decay of the scintillator's light production for time t after the proton bunch radiation. The response for a given time window is shown, normalised to the response of the first μs. The data are fitted with an exponential function, from which a decay time (half-life) of 379 ± 1 μs is extracted. The statistical uncertainty is from the fit to the proton bunch charge and the total uncertainty includes the width correction uncertainty and an uncertainty due to the changing experimental conditions.

5.4.3. Charge calibration

The Faraday cup which provides the charge measurement for the AWAKE electron bunch is situated close to the source, in the TCV4 area, as discussed in Section 2.2. By the time the bunch has propagated to the spectrometer it has lost a significant but indeterminate fraction of this charge. The lack of a charge measuring device in the vicinity of the spectrometer, therefore, eliminates the possibility of calibrating the scintillator's charge response *in situ*. As a result, the charge response of the scintillator was measured at the CERN Linear Electron Accelerator for Research (CLEAR) facility [93]. CLEAR generates 10–500 pC electron bunches with energies of approximately 100 MeV, providing a reasonable proxy for accelerated bunches at AWAKE.

The experimental setup at CLEAR is shown in Figure 5.16. A copy of the scintillator and vacuum window are installed, with the surface of the scintillator orthogonal to the electron bunch's mean trajectory. Immediately upstream of the vacuum window is a beam charge monitor. Downstream of the scintillator is a 5 cm diameter circular mirror, the face of which is at 45° to the beamline. The spectrometer's Andor camera, fitted with a 105 mm focal length lens is situated 3 m away at a right angle to the beamline. The camera's field of view is shown in Figure 5.17 with the scintillator in-focus in the centre of the image. The scintillator and vacuum window are installed on a motorised stage which moves in the vertical direction, allowing different parts of the scintillator to be tested.

An example of a beam image is shown in Figure 5.19. The beam spot has a typical width of 3 mm in the horizontal and 1.5 mm in the vertical. For each image, a recording of the electron bunch charge is made and the response may be compared. Due to the variation in scintillator response with beam charge, images were acquired at a variety of camera settings to prevent saturation. The image sums are corrected to the camera setup used for the largest data sample: a gate width of 0.5 ms width, an MCP gain of 250 and a delay of 0.2 ms with respect to the passage of the electron bunch. Correction for the width involves taking into account the decay of the scintillator as well as the raw gate width adjustment. Provided that the delay is always long enough that the scintillator decay is described by an exponential[1] this amounts to a correction factor $\mathcal{F}$ of the form

$$\mathcal{F} = \frac{\int_{d_1}^{d_1+w_1} dt\, e^{-\lambda t}}{\int_{d_2}^{d_2+w_2} dt\, e^{-\lambda t}} = e^{(d_2+w_2-d_1-w_1)\lambda}\, \frac{1-e^{w_1\lambda}}{1-e^{w_2\lambda}}\,, \tag{5.3}$$

[1] This was ensured by keeping the delay ≥ 0.2 ms.

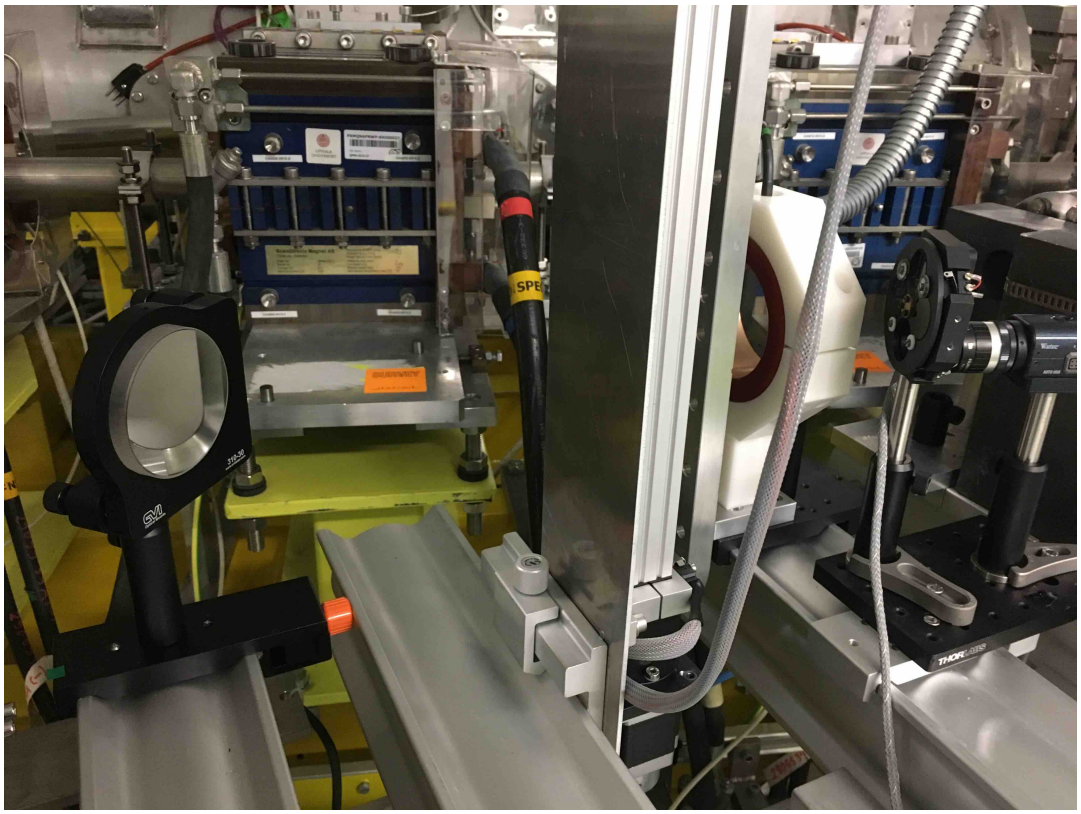

(a)

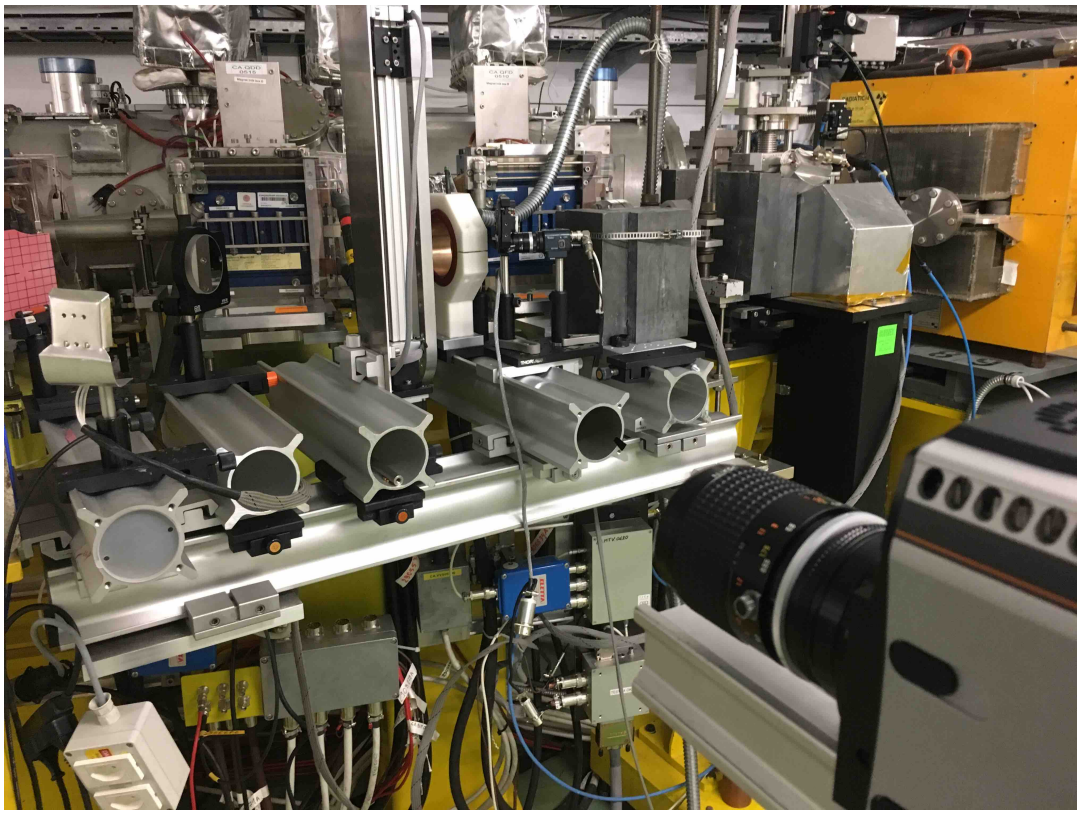

(b)

Figure 5.16.: Experimental setup at CLEAR.

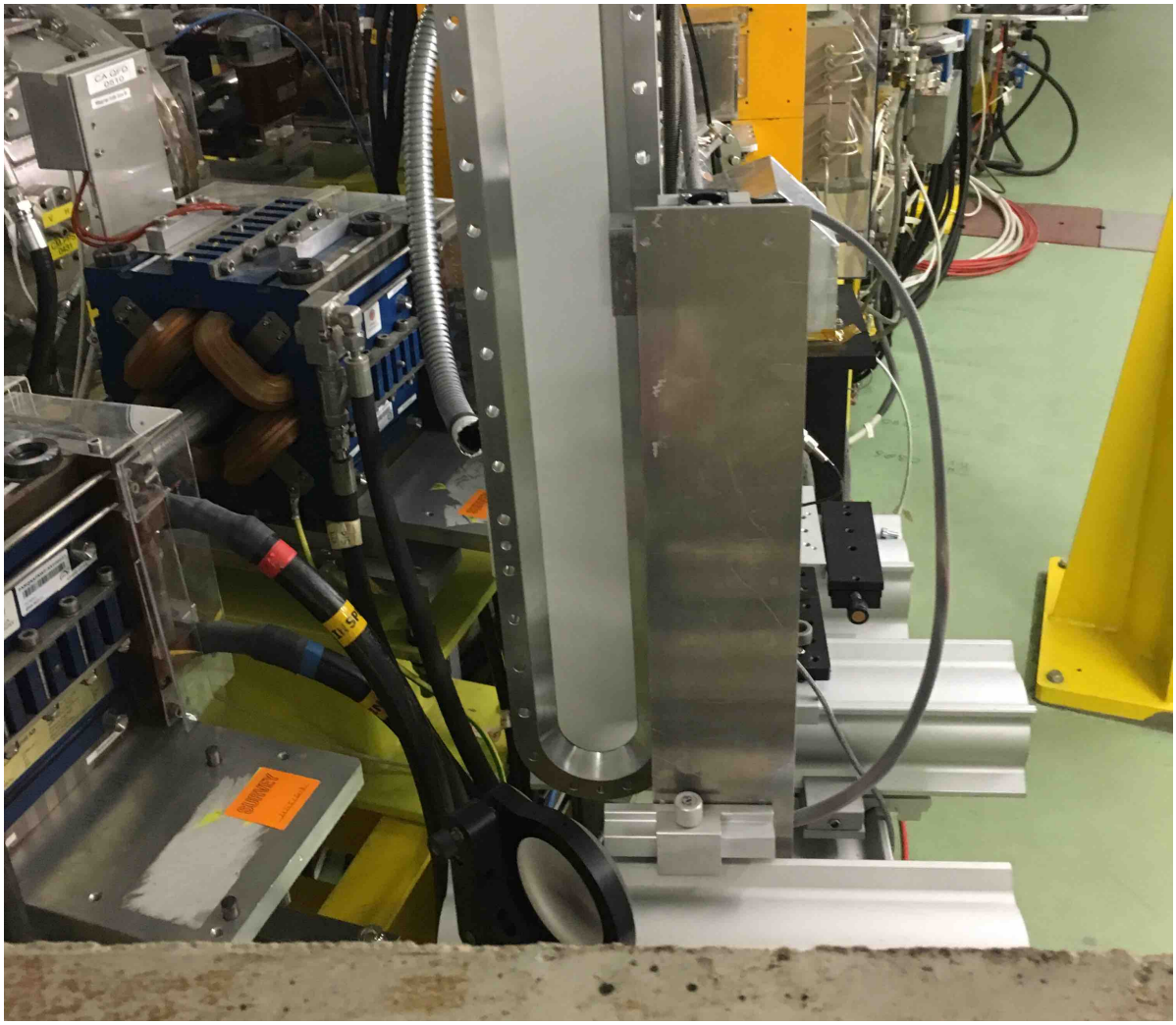

(c)

Figure 5.16.: Experimental setup at CLEAR (continued).

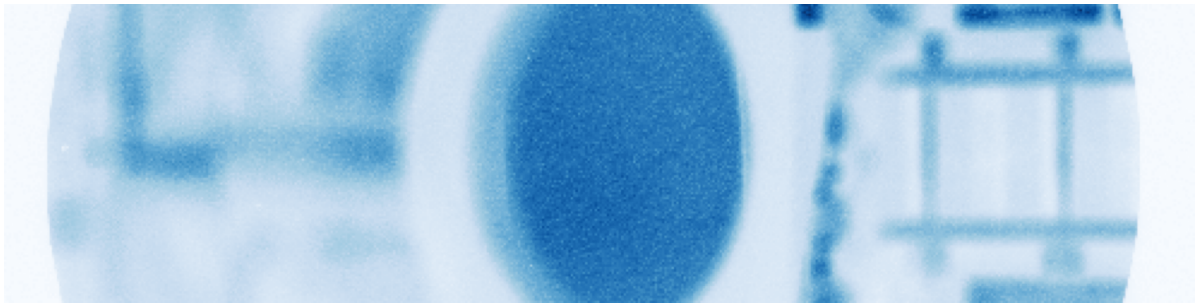

Figure 5.17.: Field of view of the spectrometer camera at CLEAR. The camera is focused to the surface of the scintillator (dark blue, centre) which is imaged via a 5 cm diameter circular mirror. During running the area lights were switched off.

(a) CLEAR

(b) AWAKE

Figure 5.18.: Images of the calibration lamp at CLEAR and AWAKE.

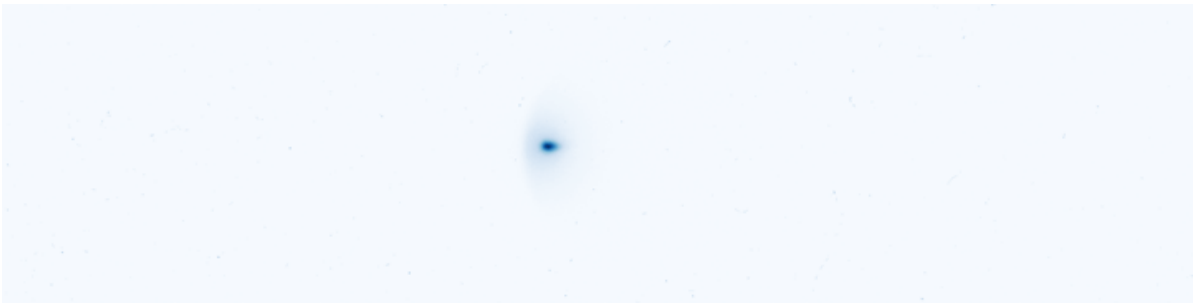

Figure 5.19.: Beam image from CLEAR. The beam spot size is approximately 3 mm in the horizontal and 1.5 mm in the vertical.

where λ is the scintillator's decay constant and d_i and w_i are, respectively, the delay and width settings for event i. The precision of both the camera and the CLEAR trigger mean that the uncertainty in the gate width and delay are negligible so the uncertainty in $\mathcal{F}$ is given by

$$\sigma_{\mathcal{F}} = \frac{\partial \mathcal{F}}{\partial \lambda} \sigma_{\lambda} \, . \tag{5.4}$$

The corrected response is shown in Figure 5.20, with the beam spot brightness binned in charge steps of 5 pC; the approximate resolution of the beam charge monitor. The

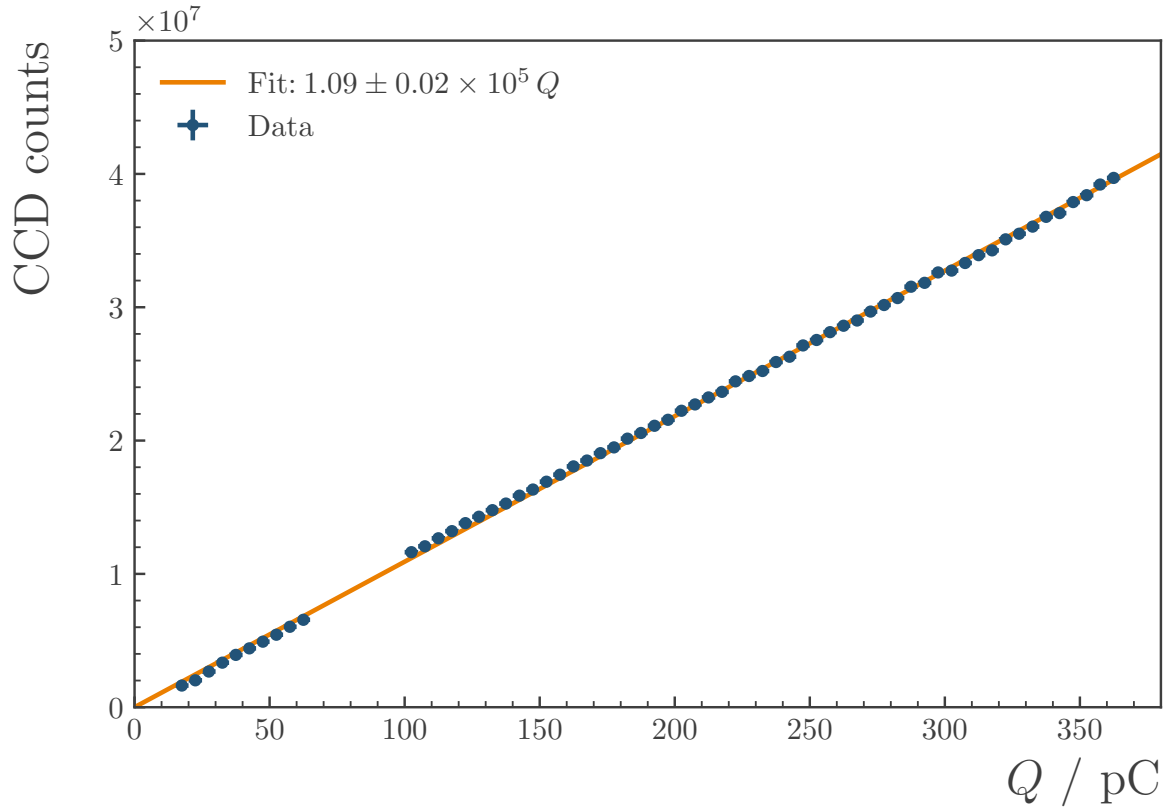

Figure 5.20.: Scintillator response as a function of incident electron bunch charge at CLEAR. The data are binned in steps of 5 pC and have been corrected for differences in the camera settings. The data are fitted to a linear function with an intercept of zero and a coefficient of $1.09 \pm 0.02 \times 10^5$ CCD counts pC^{-1}.

response is fitted to a linear function with an intercept of zero which return a coefficient of $1.09 \pm 0.02 \times 10^5$ CCD counts pC^{-1}. Further data taken at two different positions on the scintillator and at beam energies of 90 MeV and 140 MeV agree with the fit to within 1σ.

5.5. AWAKE charge response

The results from the CLEAR setup are translated to AWAKE using the calibration lamp. An image of the lamp at CLEAR is shown in Figure 5.18a, which may be compared to Figure 5.18b which shows the lamp at AWAKE. Between these two images the difference in the signal generated by some part of this lamp (the leftmost bar, say) is generated by three effects:

- Camera settings such as gate width or gain. These are known and their effect may be determined.
- The absolute brightness of the lamp. This may be due to, for example, a different power supply setting. This may be measured and is discussed below.
- Optical effects. This encapsulates all the effects due to the different optical paths such as the solid angle covered by the lens and the reflectiveness of the mirrors. If the above two factors are known, this may be determined from images such as those shown in Figure 5.18.

At AWAKE, the lamp's power supply is situated in TSG4, to protect it from radiation damage, and connected to the lamp via a long cable. Remotely, the power supply is set using FESA control software with a voltage value in the range 0.0–5.0 V. The image in Figure 5.18b, for example, was taken with the power supply set remotely to a value of 4.0 V. At CLEAR the same power supply is connected directly to the lamp and set manually using a dial on the front. This results in an additional conversion factor for the lamp brightness due to the power supply. This was measured at AWAKE by connecting the lamp directly to the power supply and comparing the brightness to that captured with the remote settings. The result is a conversion factor of 3.4 ± 0.1 for a 4.0 V image such as Figure 5.18b.

The AWAKE charge response for the May setup is given by

$$\begin{aligned} \mathcal{Q}_F &= \frac{\mathcal{C}\mathcal{T}\mathcal{G}_{3000}}{\mathcal{U}\mathcal{B}\mathcal{G}_{250}} \,, \\ &= 1.09 \pm 0.02 \times 10^5 \times \frac{312 \pm 1}{1.7 \pm 0.1} \times \frac{1}{3.4 \pm 0.1} \times \frac{1}{14 \pm 1} \times 3.26 \pm 0.10 \,, \\ &= 1.37 \pm 0.14 \times 10^6 \,\text{CCD counts pC}^{-1} \,, \end{aligned} \tag{5.5}$$

where the factors are as follows:

$\boldsymbol{\mathcal{C} = 1.09 \pm 0.02 \times 10^5}$ This is the response measured at CLEAR, as described above.

$\boldsymbol{\mathcal{G}_{3000} = 312 \pm 1}$ The relative response for a gain of 3000, given by Andor. Given in Table 5.1.

$\boldsymbol{\mathcal{G}_{250} = 1.7 \pm 0.1}$ The relative response for a gain of 250, measured using the calibration lamp. Found in Figure 5.5.

$\mathcal{U} = \mathbf{3.4 \pm 0.1}$ The voltage adjustment for the calibration lamp images at AWAKE and CLEAR, detailed above.

$\mathcal{B} = \mathbf{14 \pm 1}$ The difference in brightness between the lamp images at CLEAR and AWAKE in Figure 5.18.

$\mathcal{T} = \mathbf{3.26 \pm 0.10}$ The estimated difference in the scintillator response between the CLEAR triggering conditions and the May AWAKE triggering conditions, detailed below.

This represents a preliminary update on to the response listed in [67] which was given as $6.9 \pm 2.1 \times 10^6$ CCD counts pC^{-1}. This change stems from an updated CLEAR charge response, which was previously given by $0.9 \pm 0.2 \times 10^6$ and an updated trigger adjustment, which was previously given by 2.0 ± 0.4. The charge response changed due to a more thorough analysis of the results, yielding the improved precision reported above and a notice issued by CLEAR that their bunch charge determination had been miscalculated by a factor of 10. See, for example, the erratum reported in Ref. [94].

The update to the trigger adjustment is calculated from AWAKE data taken with the new, more precise trigger installed after May 2018. The previous value of 2.0 ± 0.4 predates the measurement of the scintillator's 0.379 ms decay time (half-life) and was based on an assumed decay time of approximately 0.33 ms [95]. The range was determined by comparing the values of Eq. (5.3) with $w_1 = 0.5\,\mathrm{ms}$, $d_1 = 0.2\,\mathrm{ms}$ and $w_2 = 4\,\mathrm{ms}$, $d_2 = [0, 0.18]\,\mathrm{ms}$. This large range in d_2 reflected the lack of knowledge about the scintillator's emission profile over the first 0.2 ms. The uncertainty due to the trigger jitter was negligible in comparison.

The new value of 3.26 ± 0.10 lies outside the predicted range but was measured directly and, therefore, should incorporate all possible effects including the scintillator, camera and any unknown contributions to the signal. The measurement compared the scintillator response to radiation as a function of proton bunch charge when foils were inserted along the beamline. The response was recorded with a gate width of 4 ms and gate delays of $-0.5\,\mathrm{ms}$, $-0.9\,\mathrm{ms}$ and $-1.3\,\mathrm{ms}$ relative to the passage of the proton bunch, to mimic the May setup. The coefficient of the response against charge was compared to measurements with a gate width of 0.5 ms and delay of 0.2 ms relative to the bunch. The ratio of the coefficients gives 3.26 ± 0.10. Both the value and the uncertainty are higher than anticipated and will be verified in future calibration work on the scintillator. For this reason, the updated charge results presented in Chapter 6 should be considered to be preliminary.

For AWAKE triggering conditions after May, the situation is greatly simplified. The gate width of 0.5 ms matches that used at CLEAR, meaning the only difference is AWAKE's 36 μs shorter delay relative to the passage of the bunch. This factor has been measured as $(1.0687 \pm 0.0028)^{-1}$, using the method described in the previous paragraph but with a delay of 0.164 ms relative to the proton bunch. Unlike the results for a 4 ms gate width, this result agrees well with the prediction of $(1.06806 \pm 0.00004)^{-1}$ from Eq. (5.3) with $\lambda = \log 2/(0.379 \pm 0.001\,\text{ms})$, $w_1 = w_2 = 0.5\,\text{ms}$, $d_1 = 0.2\,\text{ms}$ and $d_2 = 0.164\,\text{ms}$.

Chapter 6.

Detection of electrons at AWAKE

This chapter presents the first measurements of electrons accelerated by proton-driven plasma wakefield acceleration [67]. These results include the successful acceleration of electrons to GeV energies, representing the achievement of AWAKE's initial goal, as defined in the experiement's 2011 letter of intent [96].

A detailed study of the proton-generated backgrounds is presented along with techniques for isolating the electron signal. A number of individual signals at different plasma densities are discussed. Analyses with larger datasets showing the stability of the acceleration and the variation of the peak energy with plasma density are also shown.

6.1. Backgrounds at AWAKE

The background affecting spectrometer data may be factored into three components

- Background intrinsic to the camera. This includes the camera's DC offset and contributions arising from thermal noise on the CCD and electronic noise during readout. This background is estimated by capturing images with the experimental acquisition settings applied but with the lens cap on.
- Ambient background in the tunnel. This is largely due to safety lights in the experimental area and may be measured by capturing images at the experimental acquisition settings without proton or electron bunches passing through the area and subtracting the camera background.
- Proton-generated backgrounds. This arises when radiation generated by the proton bunch is incident upon the scintillator. This radiation is caused by the interaction

of the protons with a thin window between AWAKE and the SPS and, at higher plasma densities, with an iris downstream of the plasma cell. This background is defined using events where no electrons are injected.

The estimation of the first two backgrounds is trivial in that arbitrarily large datasets may be acquired in order to do so. Estimation of the proton background requires data from proton extractions under acceleration conditions. Extraction in this manner is incompatible with any other physics studies and therefore the proton background dataset is small compared to the datasets for the other backgrounds.

To find the energy distribution of the accelerated beam the scintillator signal is summed in the vertical axis. Let p_{ij} be the CCD counts of the pixel in the ith row and jth column in the image. In any image $p_{ij} = s_{ij} + b_{ij}$ where s_{ij} are the CCD counts generated by signal (scintillator photons from accelerated electrons) and b_{ij} are counts from any other source. When the image is summed in the vertical the relevant background quantities, then, are the sums $b_j = \sum_i b_{ij}$. To estimate any given b_j there are a set of n background images (images with $s_{ij} = 0 \,\forall\, i, j$) each of which are summed in the vertical axis to produce a total $v_{k,j}$, where $k = 1, \ldots, n$ is the image (event) index. The v_k[1] are assumed to be Gaussian random variables following a p.d.f. with unknown mean μ_k but with known variance[2] $\sigma_k^2 \simeq 9 \times 10^{-5} v_k^2$. That is

$$\mathcal{N}(v_k;\, \mu_k,\, \sigma_k) = \frac{1}{\sqrt{2\pi}\sigma_k} \exp\left(\frac{-(v_k - \mu_k)^2}{2\sigma_k^2}\right). \tag{6.1}$$

Each image has an associated proton bunch population $N_{p,\,k}$ with an uncertainty σ_{N_p} which is taken to be 2×10^9 protons [92]. These N_p are also assumed to be Gaussian, following $\mathcal{N}(N_{p,\,k}; \tilde{N}_{p,\,k}, \sigma_{N_p})$. The first two backgrounds described above are assumed to be approximately constant for a given camera setting, while the proton background is generated by radiation which should be proportional to the bunch population. As such, the mean is assumed to be a linear function in the proton bunch population

$$\mu(N_p; \vec{\theta}) = \theta_0 + \theta_1 N_p \,. \tag{6.2}$$

The θ_0 is the combination of the camera and ambient backgrounds, which is measured to be a Gaussian variable with mean c and standard deviation σ_c. Therefore, the overall

[1] This applies to any column so the index j is dropped. Omitted indices indicate generality rather than the result of a sum over that index, unless explicitly stated.

[2] This is established by imaging the lamp and summing over 120 pixels at various brightnesses. The relationship is linear in the range of the typical scintillator signal.

likelihood function is given by

$$\begin{aligned}\mathcal{L}(\vec{\theta}) &= \prod_{k=1}^{n} \mathcal{N}(v_k;\vec{\theta})\mathcal{N}(\theta_0;c,\sigma_c)\mathcal{N}(N_{p,k};\tilde{N}_{p,k},\sigma_{N_p})\,,\\ &= \prod_{k=1}^{n} \frac{1}{\sqrt{2\pi}\sigma_k}\exp\left(\frac{-(v_k-\mu_k(\tilde{N}_{p,k};\vec{\theta}))^2}{2\sigma_k^2}\right)\frac{1}{\sqrt{2\pi}\sigma_c}\exp\left(\frac{-(\theta_0-c)^2}{2\sigma_c^2}\right)\\ &\qquad\times\frac{1}{\sqrt{2\pi}\sigma_{N_p}}\exp\left(\frac{-(N_{p,k}-\tilde{N}_{p,k})^2}{2\sigma_{N_p}^2}\right). \end{aligned} \tag{6.3}$$

By the effective variance method [97], maximising this likelihood is equivalent to minimising

$$\chi^2(\vec{\theta}) = \sum_{k=1}^{n}\frac{(v_k-\mu_k(N_{p,k};\vec{\theta}))^2}{\sigma_k^2+\theta_1^2\sigma_{N_p}^2} + \frac{(\theta_0-c)^2}{\sigma_c^2} \simeq -2\log\mathcal{L}(\vec{\theta})+C\,, \tag{6.4}$$

where C represents all the terms which are independent of $\vec{\theta}$. This results in a maximum likelihood estimator (MLE) $\hat{\mu}$. The b_j, then, follow $\mathcal{N}(\hat{\mu}_j,\sigma_j)$. In general, this estimation is reasonable but often overestimates or underestimates the entire profile of the background. This can be mitigated by defining a region on the screen where no electrons are expected. Let the surface of the scintillator be $\mathcal{S}$ and let $\mathcal{R}\subset\mathcal{S}$ be a region without electrons such that $s_j = 0\,\forall\, j\subset\mathcal{R}$. Rescaling of $\hat{\mu}$ may be done using this area

$$\hat{\mu}' = \hat{\mu}\frac{1}{n_{\mathcal{R}}}\sum\nolimits_{j\subset\mathcal{R}}\frac{v_j}{\hat{\mu}_j}\,, \tag{6.5}$$

where $n_{\mathcal{R}}$ is the number of columns in $\mathcal{R}$. Comparisons of the predicted background to data for two events are shown in Figure 6.1. For display purposes, several (185) column totals v_j have been summed together to give patches S_ℓ with $\ell = 1,\ldots,10$. The p.d.f. $\mathcal{N}(S_\ell;\hat{\mu}'_\ell,\sigma_\ell)$ describes the data well across the screen, whereas the 'unnormalised background' p.d.f. using $\hat{\mu}_\ell$ does not in either case. For both events shown in Figure 6.1 $\mathcal{R}$ is taken to be the entire low energy half of the screen ($\xi \gtrsim 0.5\,\mathrm{m}$, in this case $k\in[1,5]$) but for real data this region is set by considering the expected electron energy distribution and magnetic field strength.

The proton background sample for $n_{\mathrm{pe}}\sim 1.8\times10^{14}\,\mathrm{cm}^{-3}$ used to estimate $\hat{\mu}$ contains only $n = 30$ events but is still able to provide a good prediction for the data, with 68.3% of the v_j within $\hat{\mu}'_j\pm\sigma_j$; indicating that the background is indeed constant up to the proton bunch scaling. The least well modelled region is the low ξ part of the scintillator, which often exceeds the predicted background, as can be seen, for example,

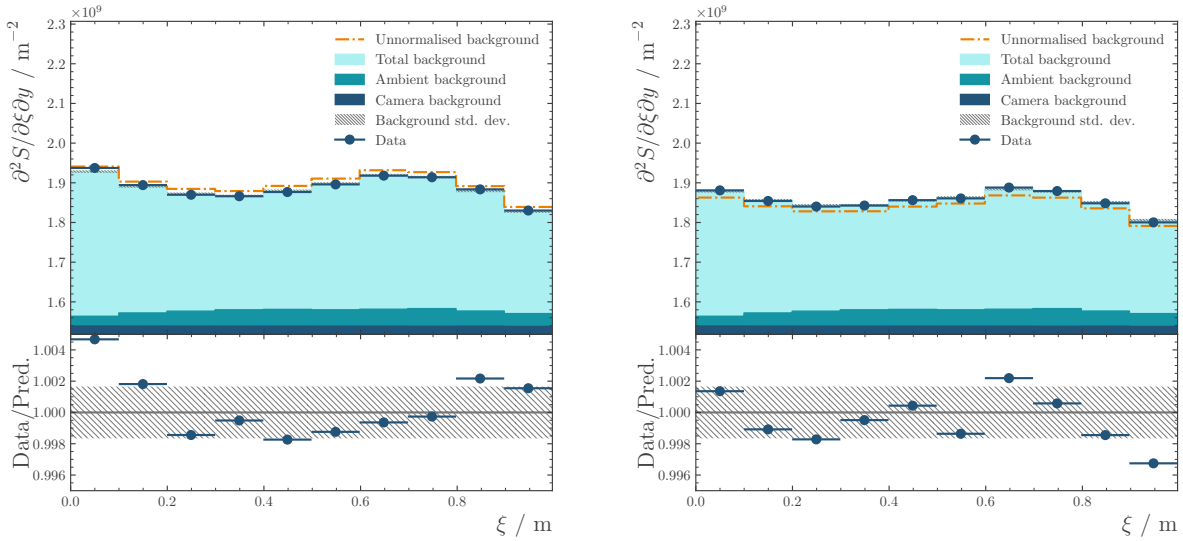

(a) Event 1 **(b)** Event 2

Figure 6.1.: Data–model comparison for two background events from the May dataset. For clearer illustration, the camera data is summed in the vertical over the scintillator and then the columns are combined into 10 patches. The background is modelled in each region as a Gaussian random variable. The mean is modelled as an approximately constant contribution from the camera (dark blue) and the ambient light in the tunnel (teal) and a linear term in the proton bunch population. This background model (orange) often overestimates or underestimates all the data and so the mean is normalised to a chosen region in the each event to give a better prediction (light blue). A ratio of the data to the model prediction is shown below the main plot. The hatched region in both plots indicates the standard deviation of the background model. The reasonable agreement in each event shows that the background is well modelled. The events shown are excluded from the sample used to model the backgrounds.

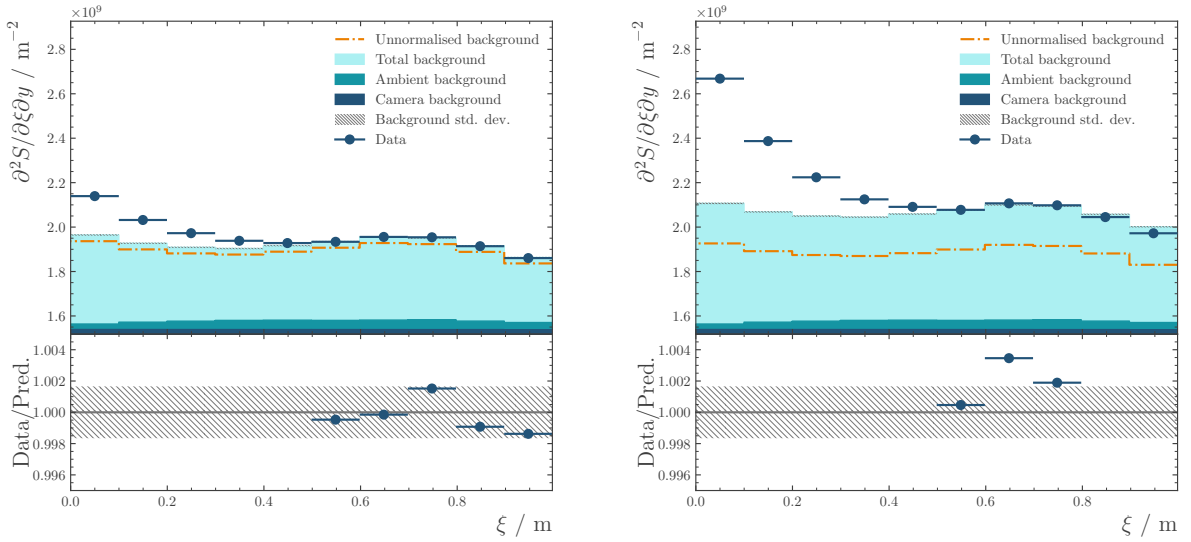

(a) Event 3 **(b)** Event 4

Figure 6.2.: Data–model comparison for two background events at higher plasma density. The event on the left is at $3.9 \times 10^4\,\mathrm{cm}^{-3}$ and the event on the right is $6.6 \times 10^4\,\mathrm{cm}^{-3}$. Further details are given in Figure 6.1.

in the first point in Figure 6.1a. This is likely due to blowout from the proton–plasma interaction which, although less significant at lower plasma densities, provides a non-zero contribution to the background, particularly if the proton trajectory is off its nominal axis.

The contribution from the proton halo becomes critical at higher plasma densities such as $3.9 \times 10^{14}\,\mathrm{cm}^{-3}$ or $6.6 \times 10^{14}\,\mathrm{cm}^{-3}$. This can be seen in Figure 6.2 which shows background events at higher densities modelled with the low density background dataset. At $3.9 \times 10^{14}\,\mathrm{cm}^{-3}$ the data are reasonably well described in the low energy part of the screen but underestimate the background close to the beam line. At $6.6 \times 10^{14}\,\mathrm{cm}^{-3}$ the profile has changed too much and only one patch is well described by the background model. Close to the beamline the radiation contribution from the halo interaction is larger than the well-modelled radiation from the window.

In these cases, where the background isn't described by a linear function of the proton bunch population, a different subtraction process is used. A region $\mathcal{E} \subset \mathcal{S}$ which includes the top and bottom edges of the screen is defined. For each column j in an image, ϵ_j is defined as the vertical sum over $\mathcal{E}_j$, which contains n_{ϵ_j} pixels. As with $\mathcal{R}$, the region $\mathcal{E}$ is defined on an event-by-event basis such that no electrons are expected to be contained within it; $s_{ij} = 0\,\forall\, i, j \subset \mathcal{E}$. Accelerated electrons with a narrow energy spread close to

the focussing energy of the quadrupoles will be confined to a small region in the centre of the screen and, consequently, $\mathcal{E}$ may be a large fraction of the screen. If the energy spread is large or if the quadrupoles are not focussing at the energy peak (if they are turned off, for example) then $\mathcal{E}$ needs to be small or this subtraction method may be inappropriate.

The relationship between ϵ and v may be estimated from the background data. Let the number of pixels in column j be n_{v_j} and the number of pixels in $\mathcal{E}_j$ be n_{ϵ_j}, the expected relation would be $v/n_v = \epsilon/n_\epsilon$. This is expected because the radiation should be approximately uniform over the vertical aperture of the scintillator as this is small compared to the distance to the radiation source; the downstream iris or the SPS window. This relation does not generally hold however, as is shown in Figure 6.3a, which is a histogram of $r_j = \epsilon_j n_{v,j}/v_j n_{\epsilon,j}$ for the event shown in Figure 6.1a. The mean of a Gaussian fit to the histogram is $\mu_r = 0.99497 \pm 0.00017$. In this example, $\mathcal{E}$ is defined as the top and bottom third of the screen[3]. A better result is achieved with the relation

$$\frac{v}{n_v} = \phi_0 \frac{\epsilon}{n_\epsilon} + \phi_1 \,. \tag{6.6}$$

The justification for this form comes from the finite resolution of the optical system and the definition of the scintillator. The edge of the scintillator may only be defined up to a finite resolution given by $\sigma_\xi \simeq 2\,\text{mm}$, thus $\mathcal{E}$ may contain pixels which do not lie on the scintillator and are therefore not expected to have values which are directly proportional to those for scintillator pixels. In addition to this, the scintillator's maximum height in the image mask is set at 120 pixels, but with the conversion of 997/1850 mm per pixel this is 64.7 mm; 2.7 mm more than the height of the scintillator. Thus there are two likely sources of non-scintillator pixels at the edge. Let there be n_δ such pixels in $\mathcal{E}$, with a summed value δ. Then the expectation that $v/n_v = \epsilon/n_\epsilon$ becomes

$$\frac{v - \delta}{n_v - n_\delta} = \frac{\epsilon - \delta}{n_\epsilon - n_\delta} \,, \tag{6.7}$$

[3]Note that this 'third' is not constant due to the curved edges of the scintillator. The total height varies from just 22 pixels in column $i = 0$, to 120 pixels over the majority of the screen and $\mathcal{E}$ varies from the outer 16 pixels to the outer 80, accordingly. All other things being equal this would mean that the possibility of including electrons in the edge is very high in the curved regions of the screen. In reality this is rarely the case because the spectrometer dipole was generally set to keep the accelerated electrons well away from this region.

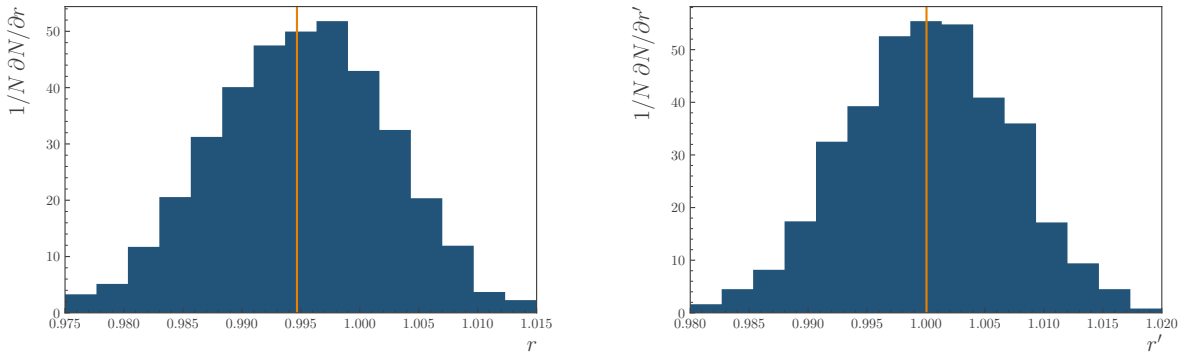

(a) **(b)**

Figure 6.3.: Histograms showing the relation of the scintillator glow at the edges to the total glow for each column in a background event. The event is the same as that used in Figure 6.1a. The edge region is defined as the top and bottom thirds of the scintillator screen. The histogram on the left shows a pixel-weighted ratio of the edge to the centre, while the histogram on the right shows the ratio using a pixel-weighted linear function, as defined in Eq. (6.6). The Gaussian mean for each histogram is shown with an orange line.

which gives

$$\frac{v}{n_v} = \frac{\epsilon}{n_\epsilon}\frac{n_\epsilon(n_\delta - n_v)}{n_v(n_\delta - n_\epsilon)} + \delta\frac{n_v - n_\epsilon}{n_v(n_\delta - n_\epsilon)}\,, \tag{6.8}$$

justifying the construction of Eq. (6.6). The fit is done with $\vec{\phi}$ rather than δ and n_δ to allow for other small effects to influence the relation.

MLEs for the $\vec{\phi}$ are determined using the n images in the background sample[4]. The values are weakly dependent on the size of $\mathcal{E}$ and need to be recalculated each time this is changed; a serious disadvantage of this background subtraction method. The histogram of $r'_j = n_{v,j}\left(\hat{\phi}_{0,j}\epsilon_j/n_{\epsilon,j} + \hat{\phi}_{1,j}\right)/v_j$ corresponding to Figure 6.3a is shown in Figure 6.3b. The mean of a Gaussian fit to this histogram is $\mu_{r'} = 0.99980 \pm 0.00014$, a notable improvement over Figure 6.3a. Background predictions for each of the events shown in Figure 6.1 and Figure 6.2 are shown in Figure 6.4. The orange line shows the background predicted using the 'bunch charge' method (previously labelled 'total background') and the filled light blue section gives the background predicted by Eq. (6.6).

[4] Assuming Eq. (6.8) holds, the $\hat{\phi}_{0,\ell}$ estimated from this sample correspond to $n_\delta \sim 6$–11 pixels per column or approximately 3–6 mm; reasonable values given σ_ξ and the up to 2.7 mm height discrepancy. The values of $\partial^2\delta/\partial\xi\partial y$ range from 1.5–1.7×10^9 which are also reasonable (cf. the 'Ambient background' in Figure 6.1).

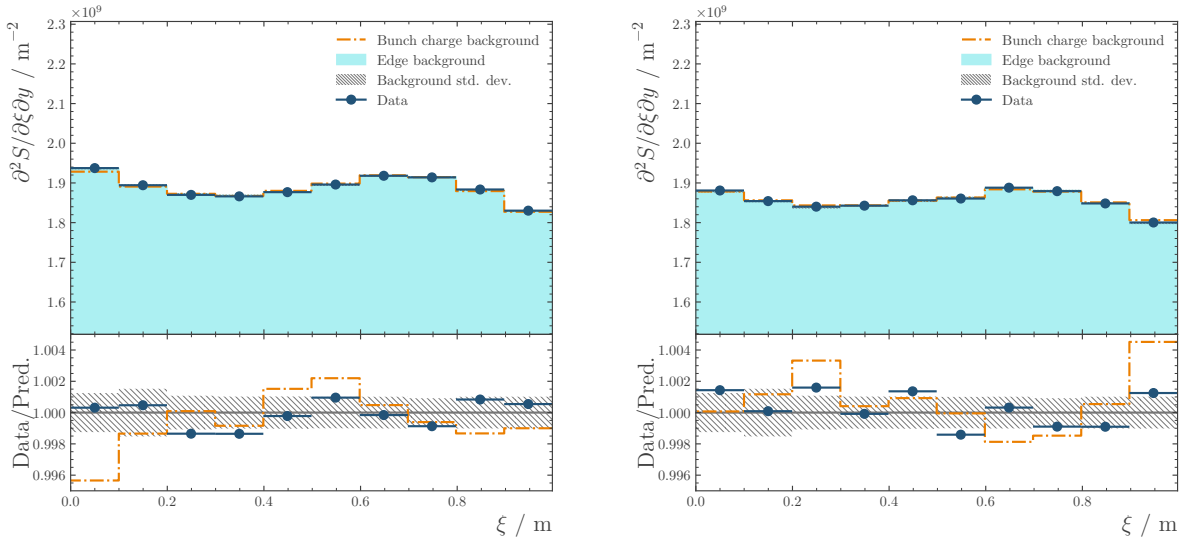

(a) Event 1

(b) Event 2

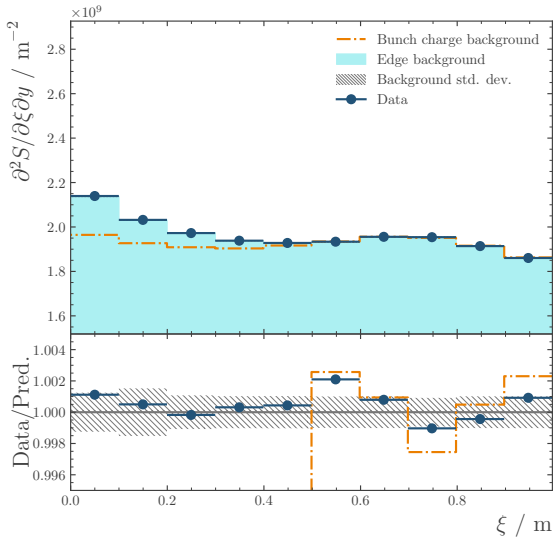

(c) Event 3

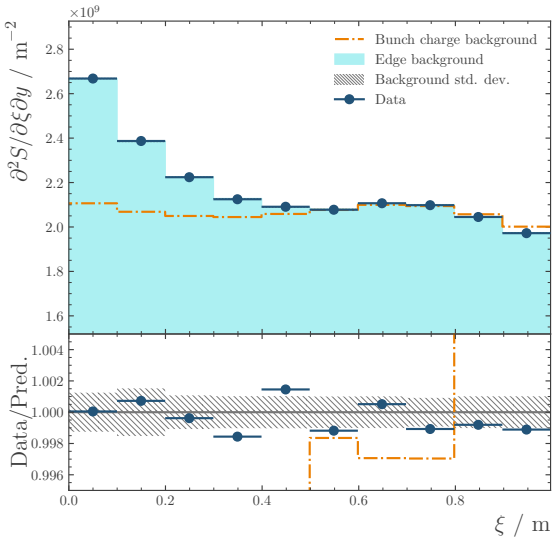

(d) Event 4

Figure 6.4.: Data–model comparison using edge background estimation. The four events shown correspond to those in Figure 6.1 and Figure 6.2. The orange line shows the background estimated using the proton bunch population model (labelled 'total background' in previous plots). The edge region is defined as the top and bottom thirds of the scintillator screen. The ratios of the data and the proton bunch model estimate to the edge background estimate are shown below each of the main plots.

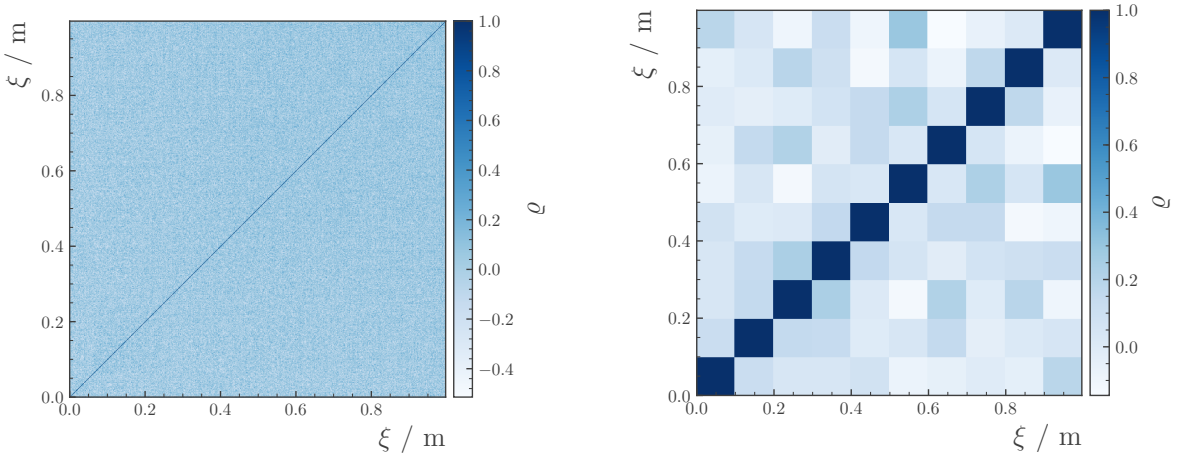

(a) **(b)**

Figure 6.5.: Correlation coefficients for the estimated signal, $v_j - \hat{b}_j$. The full matrix is shown on the left while the matrix for 185 summed adjacent columns is shown on the right. The edge region used in both cases comprises the top and bottom thirds of the screen.

The variance of the background is estimated from the background sample as

$$\hat{\sigma}_b^2 = \hat{b}^2 \cdot \frac{1}{n-1} \sum_k \left(\frac{v_k}{\hat{b}_k} - \frac{1}{n} \sum_k \frac{v_k}{\hat{b}_k} \right)^2 , \tag{6.9}$$

where $\hat{b}$ is the MLE of the background. The square root of $\hat{\sigma}_b^2$ is labelled 'background std. dev.' in Figure 6.4. Defining the uncertainty in the estimated total signal $\sum_j v_j - \hat{b}_j$ requires the calculation of the column-to-column correlations. This is estimated by

$$\varrho_{\alpha\beta} = \frac{\sum_k \left(v_{k,\alpha} - \hat{b}_{k,\alpha} - \frac{1}{n} \sum_k \left(v_{k,\alpha} - \hat{b}_{k,\alpha} \right) \right) \left(v_{k,\beta} - \hat{b}_{k,\beta} - \frac{1}{n} \sum_k \left(v_{k,\beta} - \hat{b}_{k,\beta} \right) \right)}{\sqrt{\sum_k \left(v_{k,\alpha} - \hat{b}_{k,\alpha} - \frac{1}{n} \sum_k \left(v_{k,\alpha} - \hat{b}_{k,\alpha} \right) \right)^2 \cdot \sum_k \left(v_{k,\beta} - \hat{b}_{k,\beta} - \frac{1}{n} \sum_k \left(v_{k,\beta} - \hat{b}_{k,\beta} \right) \right)^2}} , \tag{6.10}$$

for columns α and β. The full version of this is shown in Figure 6.5a for the same definition of $\mathcal{E}$ as above. The summed version corresponding to the points in Figure 6.4 is shown in Figure 6.5b. The mean correlation between adjacent columns in the full matrix is $\bar{\varrho}_{\alpha,\alpha\pm1} \simeq 0.65$.

While there are points where the 'bunch charge' background $\hat{\mu}'$ performs best (for example, the two patches around $\xi = 0.6\,\mathrm{m}$ in Figure 6.4c) it is clear that Eq. (6.6) generally provides the best estimation of the b. This is particularly true at low ξ and

at higher plasma densities, where the contribution to the background from the halo interactions along the beamline is large and cannot be predicted.

The main disadvantage of the edge subtraction is also clear: it relies on being able to define a region along both edges of the screen where no electrons are expected. Defining this region is difficult to automate and is ideally done manually, invalidating the technique for large datasets. In general, this is not a problem as a precise distribution of charge is not required for most AWAKE analyses and a single $\mathcal{E}$ can be used for the entire dataset. For much of the experimental running, the proton bunch charge background estimate was used for the data quality monitors. In publications displaying individual events, such as Ref. [67], an $\mathcal{E}$ was defined for each event and edge subtraction was used.

6.2. Electron acceleration

An accelerated electron peak is minimally defined by the following algorithm:

1. Find the column P_c with the maximum value of $(v_j - \hat{b}_j)/\hat{\sigma}_{b,j}$.
2. The upper side of the peak P_u is given as the minimum value of $j > P_c$ which satisfies $v_{j'} - \hat{b}_{j'} \leq \hat{\sigma}_{b,j'} \; \forall \; j' \in [j+1, j+3]$.
3. The lower side of the peak P_l is given as the maximum value of $j < P_c$ which satisfies $v_{j'} - \hat{b}_{j'} \leq \hat{\sigma}_{b,j'} \; \forall \; j' \in [j-1, j-3]$.
4. The peak region $\mathcal{P}$ is defined as the interval $[P_l, P_u]$.

The purpose of the algorithm is to establish the energy and charge of an accelerated bunch. Optional further steps may be added to this to cut on the peak's charge and rerun with the next-to-maximum positive deviation until a suitable peak is defined or some limit is reached and the event is rejected. In this way, the algorithm may be modified to perform a charge 'cut' on events for an analysis.

The choice of three columns in steps (2) and (3) is somewhat arbitrary and may be adjusted as necessary. For example, if the data are summed into 10 points as in Figure 6.4 then changing three to one or two would be appropriate. In general, the data are not summed into such a low number of points and three is a good choice for the peak definition.

For very low signals, hot pixels in the background can affect the location of P_c. In these cases it is better to sum five or 10 adjacent v_j into patches and use that in step (1) instead.

Let $Q_j = \mathcal{Q}_F(v_j - \hat{b}_j)$ be the signal charge in the jth column, with $\mathcal{Q}_F$ as defined in Section 5.5. Then the charge in the peak is given by

$$Q_{\mathcal{P}} = \sum\nolimits_{j\in\mathcal{P}} \mathcal{V}_j \mathcal{A}_j Q_j \,, \tag{6.11}$$

where $\mathcal{V}$ and $\mathcal{A}$ are the vignetting and angle corrections detailed in Section 5.3.2 and Section 5.4.1 respectively. The uncertainty on the peak charge will be given as two separate components, one from a combination of the Q_F, $\mathcal{V}$ and $\mathcal{A}$ uncertainties, labelled 'corr.', and one labelled 'peak' from the background uncertainty, which is given by the square root of

$$\sigma^2_{\mathcal{P}} = \sum\nolimits_{j,\iota\in\mathcal{P}} \hat{\sigma}_{b,j} \hat{\sigma}_{b,\iota} \varrho_{j\iota} \,, \tag{6.12}$$

with $\hat{\sigma}_b$ and ϱ defined in Eq. (6.9) and Eq. (6.10) respectively. The two uncertainties are uncorrelated so the total uncertainty in the peak charge is their sum in quadrature.

6.2.1. Results at $n_{\mathrm{pe}} = 1.8 \times 10^{14}\,\mathrm{cm}^{-3}$

Figure 6.6 shows an electron acceleration event from the May AWAKE dataset. All events from the May dataset have the same camera acquisition settings: an MCP gain of 3000, a gate width of 4 ms and a gate delay of 0.5 ms. For the event shown the quadrupoles were set to focus at approximately 700 MeV and the peak of the electron distribution is seen at 822 ± 41 MeV. The full width at half maximum (FWHM) of the distribution is 137.3 ± 13.7 MeV. The uncertainties are driven by the beam emittance and trajectory [75], which dominate over the other factors. The edge region can be seen in the figure and comprises the top and bottom quarters of the screen. The tradeoff in choosing this region is clear from the peak finding algorithm: for smaller $\mathcal{E}$ the variance in the background will be larger and the peak area satisfying steps (2) and (3) will be smaller but larger $\mathcal{E}$ will start of include regions containing electrons, reducing the peak charge by subtracting them from the central region. This relationship is displayed in Figure 6.7, which shows how the apparent charge in the peak in Figure 6.6 changes with the fraction of the screen covered by $\mathcal{E}$, $f_{\mathcal{E}}$. The edge definition chosen in Figure 6.6 corresponds to $f_{\mathcal{E}} = 0.5$ and

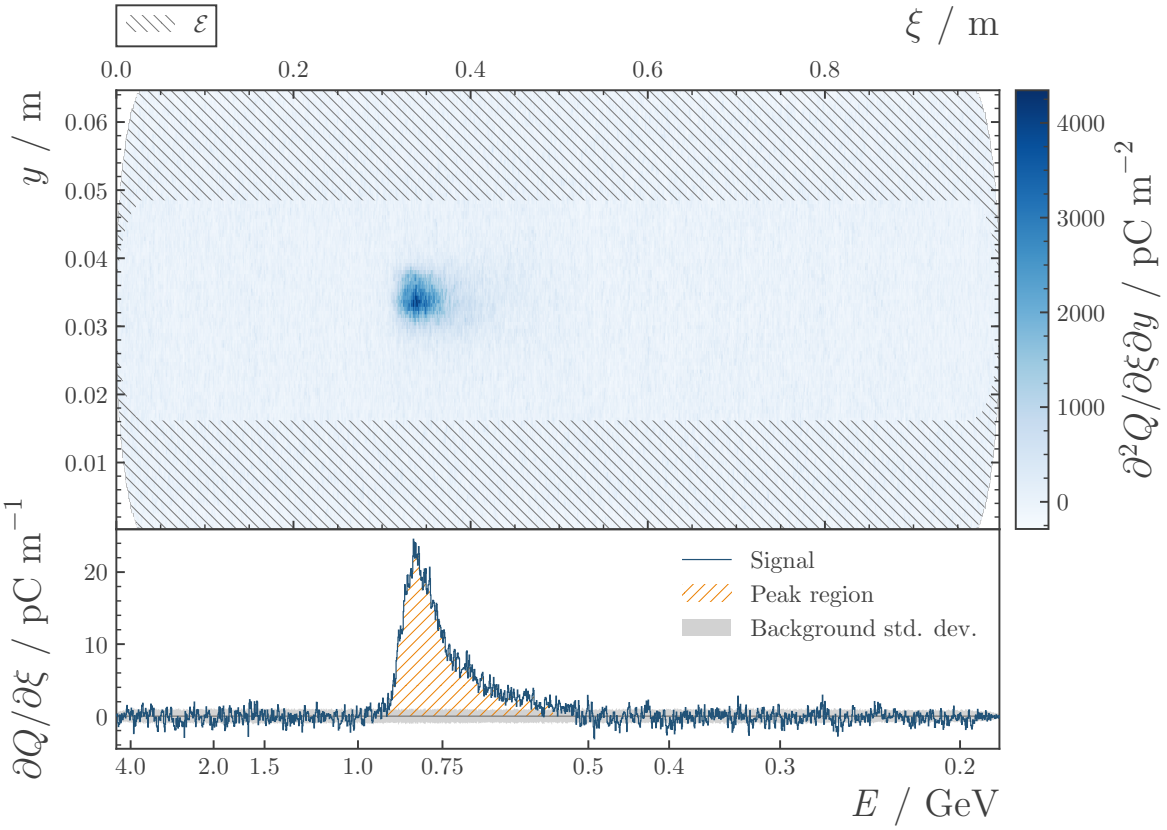

Figure 6.6.: Accelerated electrons at AWAKE. The background-subtracted beam image is shown top with a peak clearly visible. The edge region $\mathcal{E}$ is defined as the top and bottom quarter of the screen and is shaded. The vertical sum over the image is shown below, with the peak region shown in orange. The standard deviation of the subtracted background is shaded in grey around zero. Both the charge and the energy are calculated using their central values. The plasma density is $n_{\mathrm{pe}} = 1.8 \times 10^{14}\,\mathrm{cm}^{-3}$ with a $+5.3\% \pm 0.3\%$ difference over 10 m and the spectrometer quadrupoles are focusing at approximately 700 MeV. The charge in the peak region is $Q_{\mathcal{P}} = 1.136 \pm (0.037)^{\mathrm{peak}} \pm (0.116)^{\mathrm{corr.}}$ pC. The dipole current is set to 240 A. AWAKE event ID `1527302868`.

gives $Q_{\mathcal{P}} = 1.136 \pm (0.037)^{\mathrm{peak}} \pm (0.116)^{\mathrm{corr.}}$ pC. This point in Figure 6.7 can be seen to maximise the apparent peak charge without increasing the uncertainty too much.

A plasma density difference of $+5.3\% \pm 0.3\%$ over 10 m was set for the event in Figure 6.6, raising the energy of the accelerated electrons. The effect of density gradients is discussed further in Section 6.2.3. Figure 6.8 shows an example of an event without a gradient set. The peak energy is 638 ± 32 MeV. The event is also interesting to consider because of the defocused low energy tail. The analog to Figure 6.7 for this event without a gradient is shown in Figure 6.9. An edge region with $f_{\mathcal{E}} = 0.375$ maximises the peak

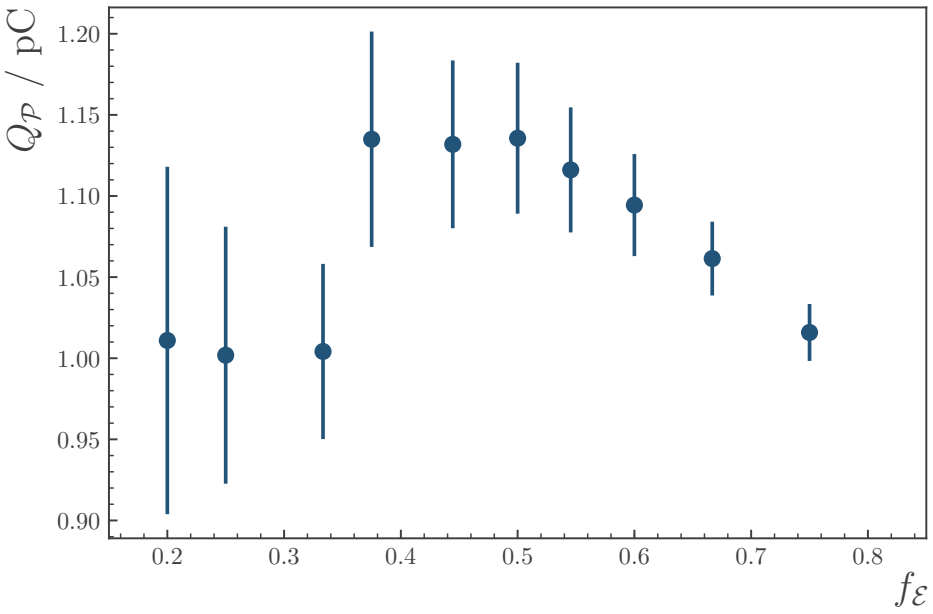

Figure 6.7.: Electron peak charge as a function of the edge definition for the event shown in Figure 6.6. The apparent charge in the electron acceleration peak as defined by the peak algorithm changes with the fraction $f_{\mathcal{E}}$ of the screen defined as belonging to $\mathcal{E}$.

charge, with a reasonable uncertainty. A smaller optimum $f_{\mathcal{E}}$ is consistent with the observation that the low energy part of Figure 6.8 spreads out more in y than Figure 6.6. Although $f_{\mathcal{E}} = 0.375$ has been selected it should be noted that several of the points surrounding it overlap to within 1σ, as is the case for $f_{\mathcal{E}} = 0.5$ in Figure 6.7. This overlap shows that the peak charge is not overly sensitive to the precise definition of the edge region. For the remaining events shown in the chapter, values of $f_{\mathcal{E}}$ have been chosen in accordance with these considerations.

A notable feature of electron acceleration at low density is its reliability. A collection of 194 consecutive electron injection events is shown in Figure 6.10 with the focusing strength of the quadrupoles in each axis overlaid. The stability of the peak location with varying quadrupole strength is a strong indication that the energy spectrum shown is close to the true spectrum and is not determined by the energy at which the quadrupoles focus.

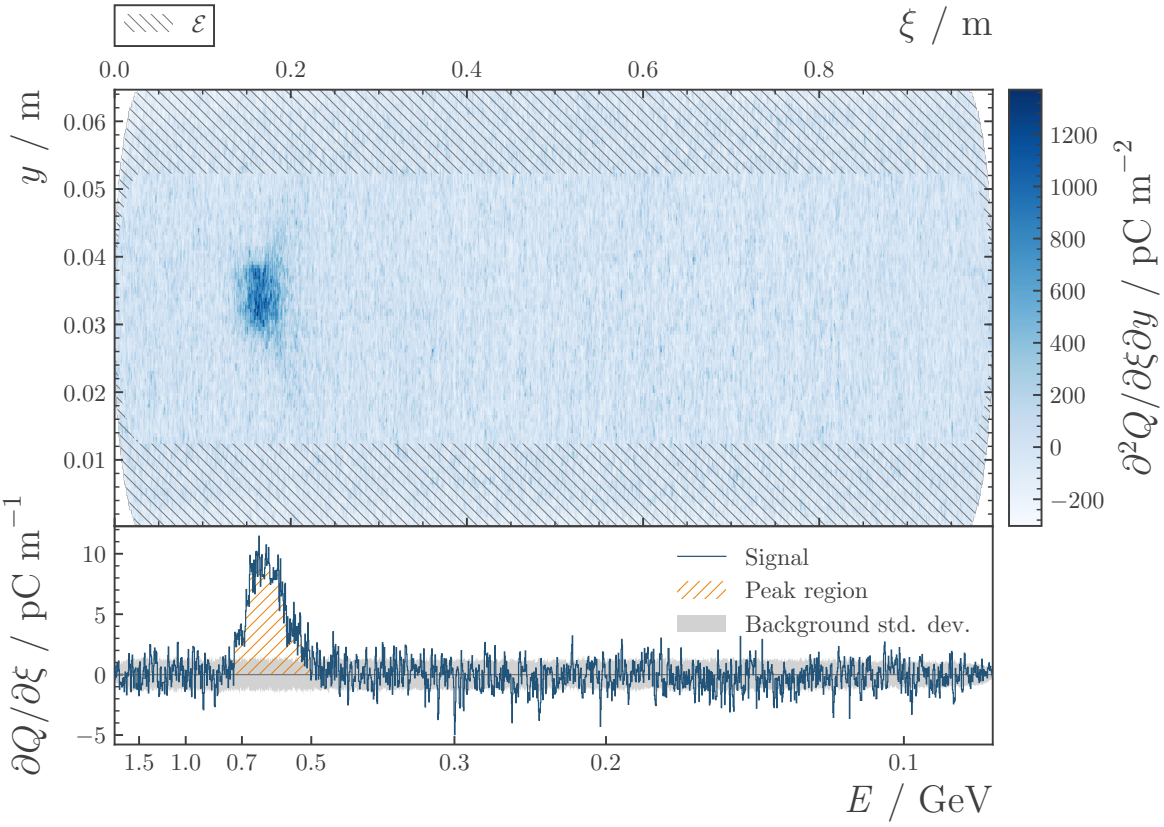

Figure 6.8.: Accelerated electrons at low plasma density with no gradient. The edge region $\mathcal{E}$ is defined with $f_{\mathcal{E}} = 0.375$. The plasma density is $n_{\mathrm{pe}} = 1.8 \times 10^{14}\,\mathrm{cm}^{-3}$ no density gradient and the spectrometer quadrupoles are focusing at approximately 550 MeV. The charge in the peak region is $Q_{\mathcal{P}} = 0.386 \pm (0.021)^{\mathrm{peak}} \pm (0.039)^{\mathrm{corr.}}$ pC. Further details on the plot style may be found in Figure 6.6. The dipole current is set to 100 A. AWAKE event ID 1527291333.

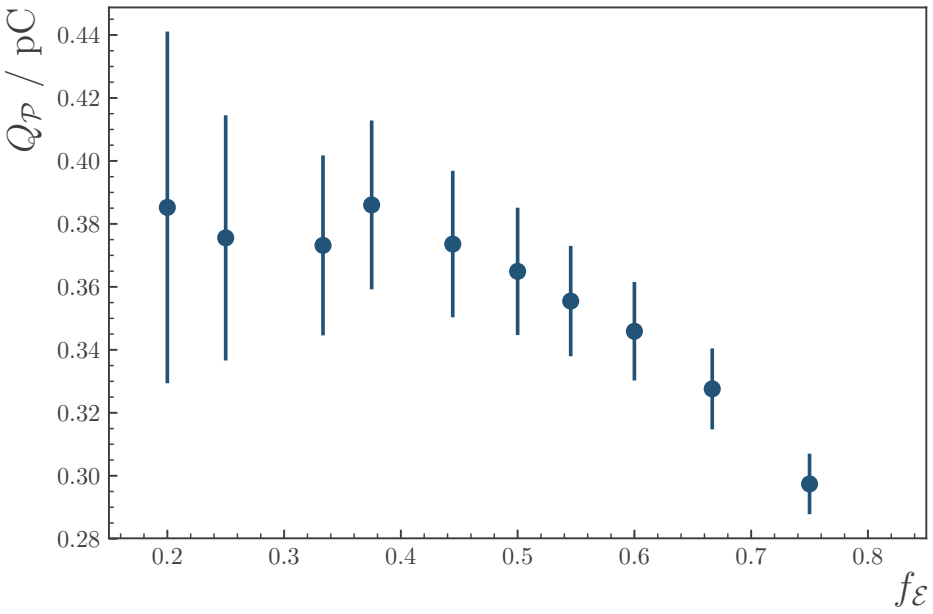

Figure 6.9.: Electron peak charge as a function of the edge definition for the event shown in Figure 6.8.

6.2.2. Results at higher density

Higher plasma densities lead to stronger wakefields and higher energy electrons. Examples of this trend are shown for events at $n_{\mathrm{pe}} = 3.9 \times 10^{14}\,\mathrm{cm}^{-3}$ in Figure 6.11 and Figure 6.12 and at $n_{\mathrm{pe}} = 6.6 \times 10^{14}\,\mathrm{cm}^{-3}$ in Figure 6.13 and Figure 6.14. The captured charge generally decreases with increasing plasma density[5]. This is interpreted as a geometric effect: the higher the plasma density the smaller the wakefield and, therefore, the smaller the probability to overlap the beam with an accelerating region. The combination of this reduction in signal with the limited range of the quadrupoles, which have a maximum of approximately 1.3 GeV, makes events at the highest densities difficult to detect. The peak energy reached in the event shown in Figure 6.14 is 2.0 ± 0.1 GeV with a width of approximately 300 ± 30 MeV.

6.2.3. Plasma density gradient studies

Simulations of acceleration at AWAKE indicate increases in the energy gained by the electrons when a density gradient is introduced in the plasma [59]. Experimentally this gradient is introduced by changing the heating between the upstream and downstream

[5] Figure 6.13 is an exception.

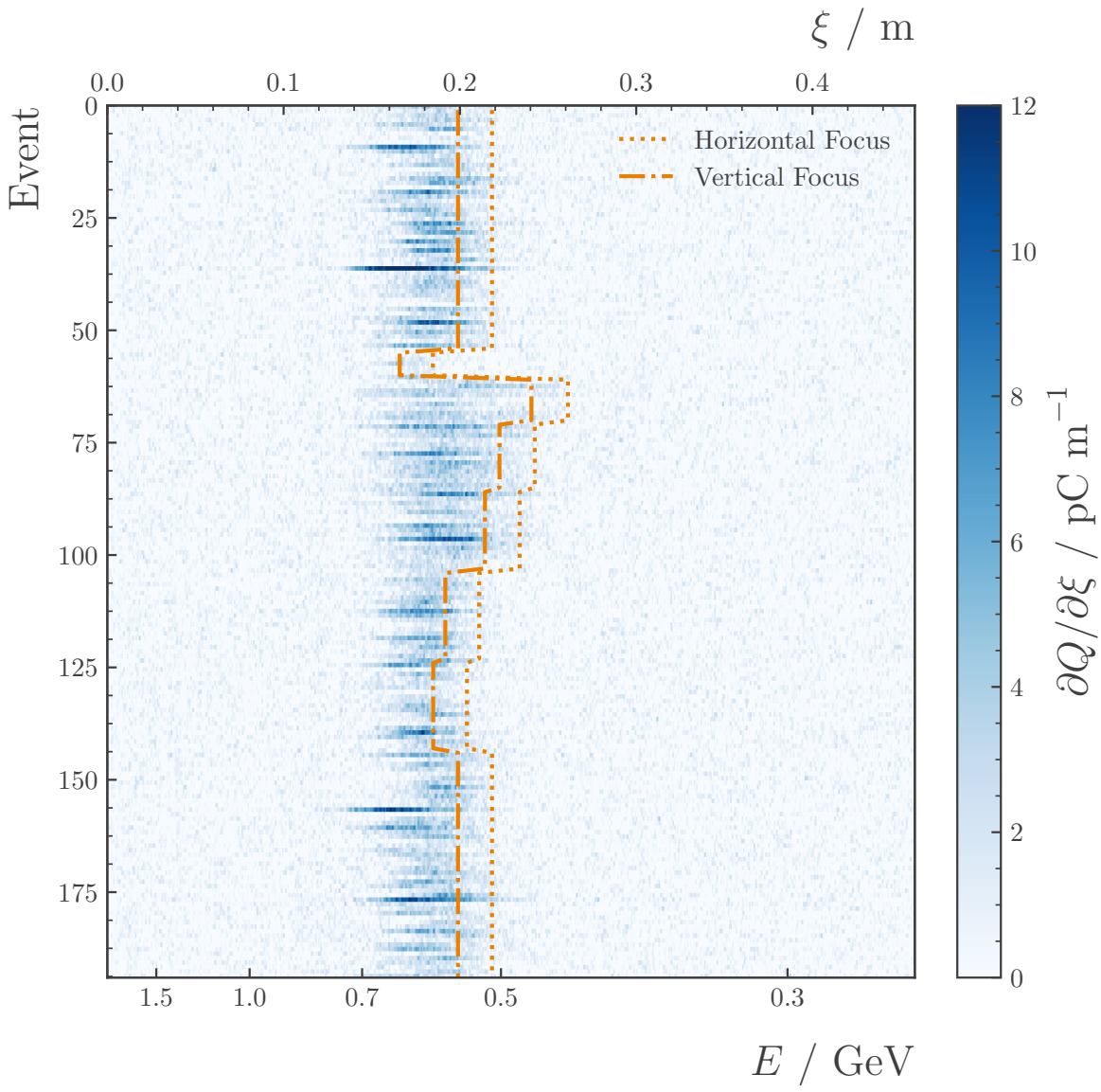

Figure 6.10.: Consecutive electron injection events at low density. Each column shows the estimated charge density in an event (cf. the bottom plot in Figure 6.6). The focusing energies of the quadrupoles are shown in orange and are scanned around the peak energy. No other parameters were deliberately varied, though some vary naturally, such as the proton bunch population. The consistent peak at around 600 MeV demonstrates the stability and reliability of the electron acceleration. The dipole current is set to 100 A throughout.

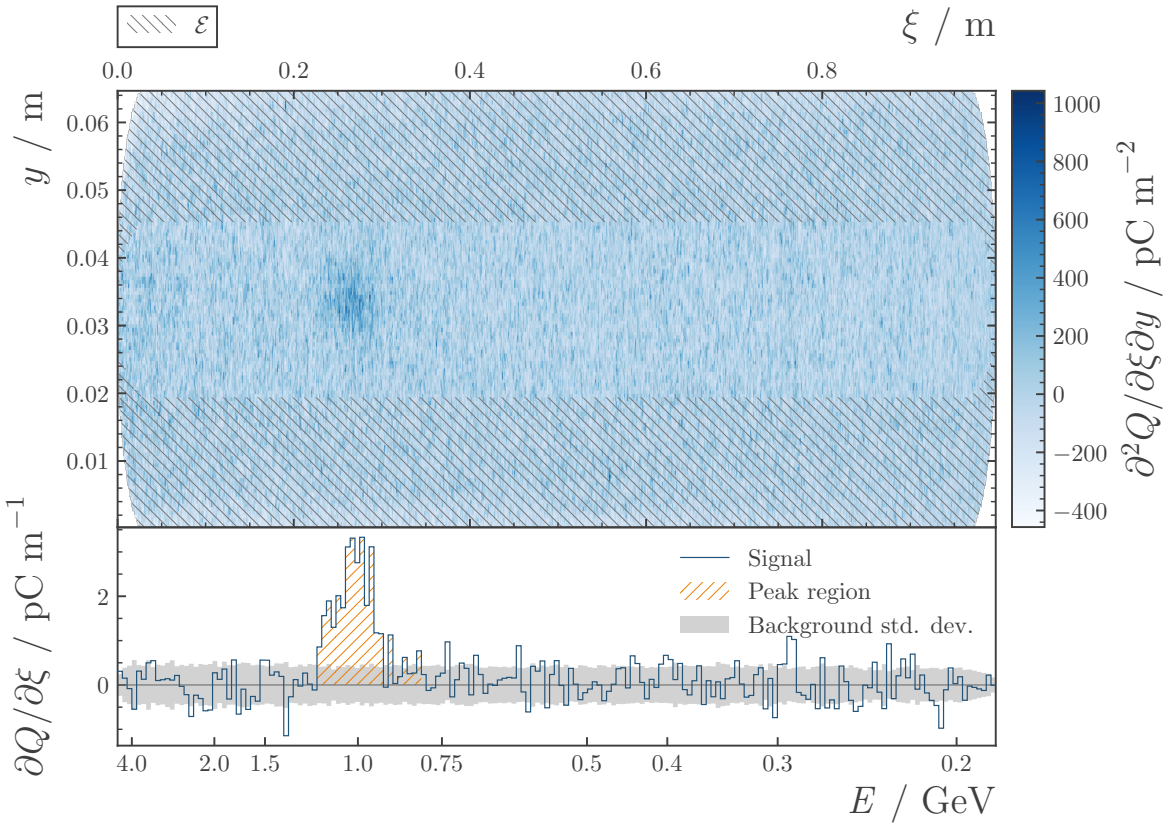

Figure 6.11.: Accelerated electrons at $n_{\mathrm{pe}} = 3.9 \times 10^{14}\,\mathrm{cm}^{-3}$ with no gradient. The edge region $\mathcal{E}$ is defined as the top and bottom 30% of the screen. The spectrometer quadrupoles are focusing at approximately 850 MeV. The charge in the peak region is $Q_{\mathcal{P}} = 0.131 \pm (0.011)^{\mathrm{peak}} \pm (0.013)^{\mathrm{corr.}}$ pC. In the lower plot, groups of 10 adjacent columns in the image have been summed to make the signal clearer. The dipole current is set to 240 A. AWAKE event ID `1527386694`.

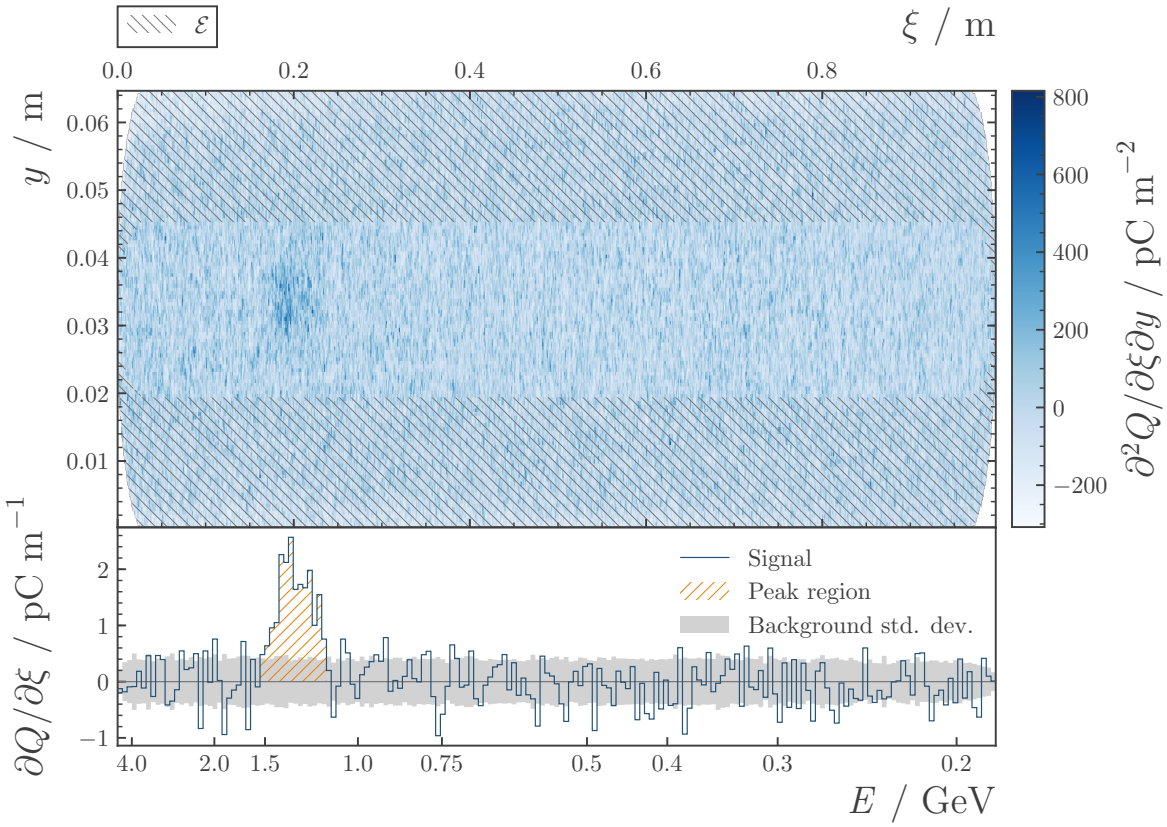

Figure 6.12.: Accelerated electrons at $n_{\mathrm{pe}} = 3.9 \times 10^{14}\,\mathrm{cm}^{-3}$ with a density difference of $2.5\% \pm 0.3\%$ over 10 m. The edge region $\mathcal{E}$ is defined as the top and bottom 30% of the screen. The spectrometer quadrupoles are focusing at approximately 1.3 GeV. The charge in the peak region is $Q_{\mathcal{P}} = 0.084 \pm (0.009)^{\mathrm{peak}} \pm (0.009)^{\mathrm{corr.}}$ pC. The dipole current is set to 240 A. AWAKE event ID 1527392828.

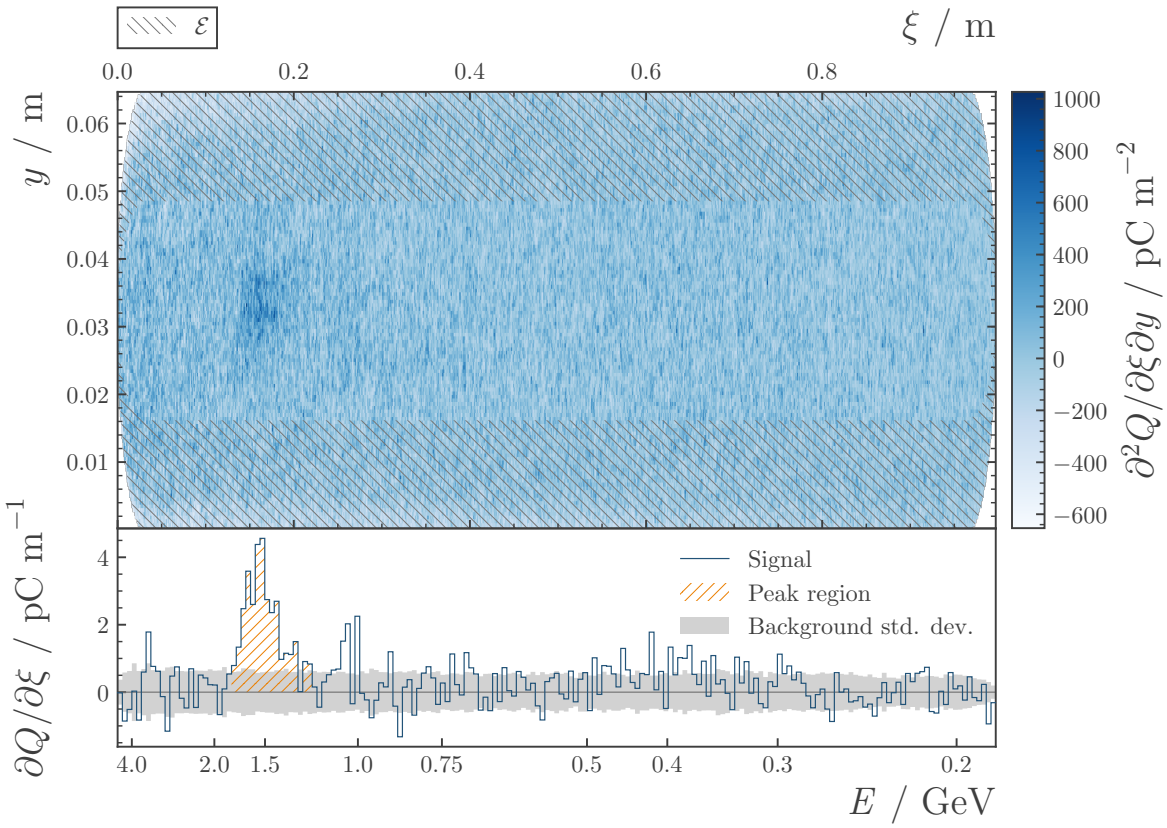

Figure 6.13.: Accelerated electrons at $n_{\mathrm{pe}} = 6.6 \times 10^{14}\,\mathrm{cm}^{-3}$ with no gradient. The edge region $\mathcal{E}$ is defined as the top and bottom quarter of the screen. The spectrometer quadrupoles are focusing at approximately 1.3 GeV. The charge in the peak region is $Q_{\mathcal{P}} = 0.145 \pm (0.017)^{\mathrm{peak}} \pm (0.015)^{\mathrm{corr.}}$ pC. The dipole current is set to 240 A. AWAKE event ID `1527457119`.

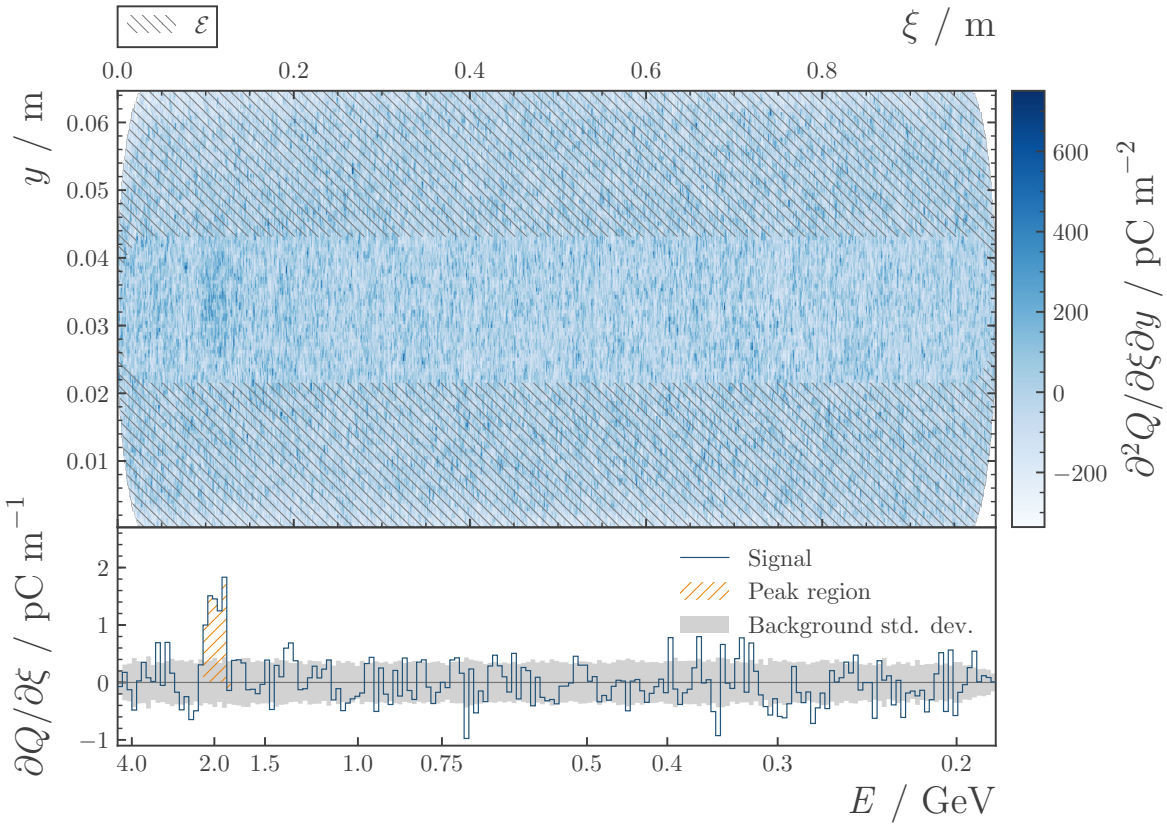

Figure 6.14.: Accelerated electrons at $n_{\mathrm{pe}} = 6.6 \times 10^{14}\,\mathrm{cm}^{-3}$ with a density difference of $2.2\% \pm 0.1\%$ over 10 m. The edge region $\mathcal{E}$ is defined as the top and bottom third of the screen. The spectrometer quadrupoles are focusing at approximately 1.3 GeV. The charge in the peak region is $Q_{\mathcal{P}} = 0.031 \pm (0.006)^{\mathrm{peak}} \pm (0.003)^{\mathrm{corr.}}$ pC. The dipole current is set to 240 A. AWAKE event ID `1527461958`.

rubidium flasks. Specifically, increasing density in the direction of propagation for the beams (a positive density gradient) is predicted to increase the energy gained and this is done by raising the temperature in the downstream rubidium flask relative to the upstream flask. This increase in density over the length of the vapour source corresponds to an increasing plasma wavelength and, therefore, wakefield phase velocity. It is predicted that the increasing phase velocity mitigates the effect of dephasing, where the accelerating electrons gain enough energy to 'overrun' the wakefield, moving out of the accelerating phase and achieving a lower final energy as a result.

Data at different density gradients were taken for three different plasma densities, as indicated in the previous subsections. Other parameters also vary during these three datasets, either due to deliberate alteration to improve the quality of the data or naturally due to jitter and drift in the experimental apparatus. As such, a number of cuts are made on the datasets to reduce the dependence on these other parameters which may also affect the energy gain of the electrons. These parameters include the laser pulse energy, the proton bunch population and the electron's injection trajectory (as measured by the electron line BPMs). The cuts made at each density are intended for comparison within that dataset rather than between them. For example, the laser pulse energy is approximately 60 mJ for almost all the events at $n_{\mathrm{pe}} = 6.6 \times 10^{14}\,\mathrm{cm}^{-3}$ but is set around 115 mJ for $n_{\mathrm{pe}} = 1.8 \times 10^{14}\,\mathrm{cm}^{-3}$. Without compensating for the possible effect of this change (and others) the energies at different densities may not be directly compared. This rules out, for example, a true $E \propto \sqrt{n_{\mathrm{pe}}}$ comparison.

The details of the cuts for each density are given in Table 6.1 and are shown in Figure 6.15 alongside the event-by-event measurements of the relevant parameters for each dataset. Histograms showing the number of events passing the cuts at each density are shown alongside the results in Figure 6.16. The cuts were chosen to sufficiently flatten the data with respect to variables other than the density while keeping the number of events as large as possible. The AWAKE extraction rate of approximately one event per 30 seconds makes this difficult. However, even with the small number of events there is clear difference in energy with and without a gradient set.

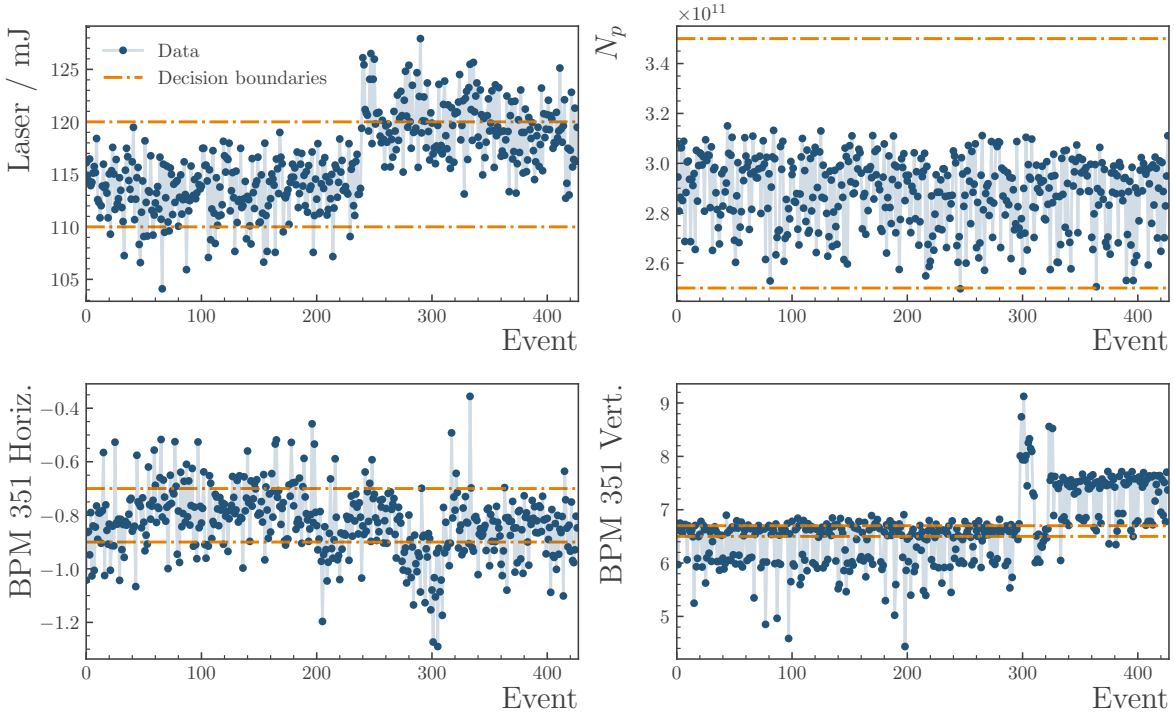

(a) $1.8 \times 10^{14}\,\mathrm{cm}^{-3}$

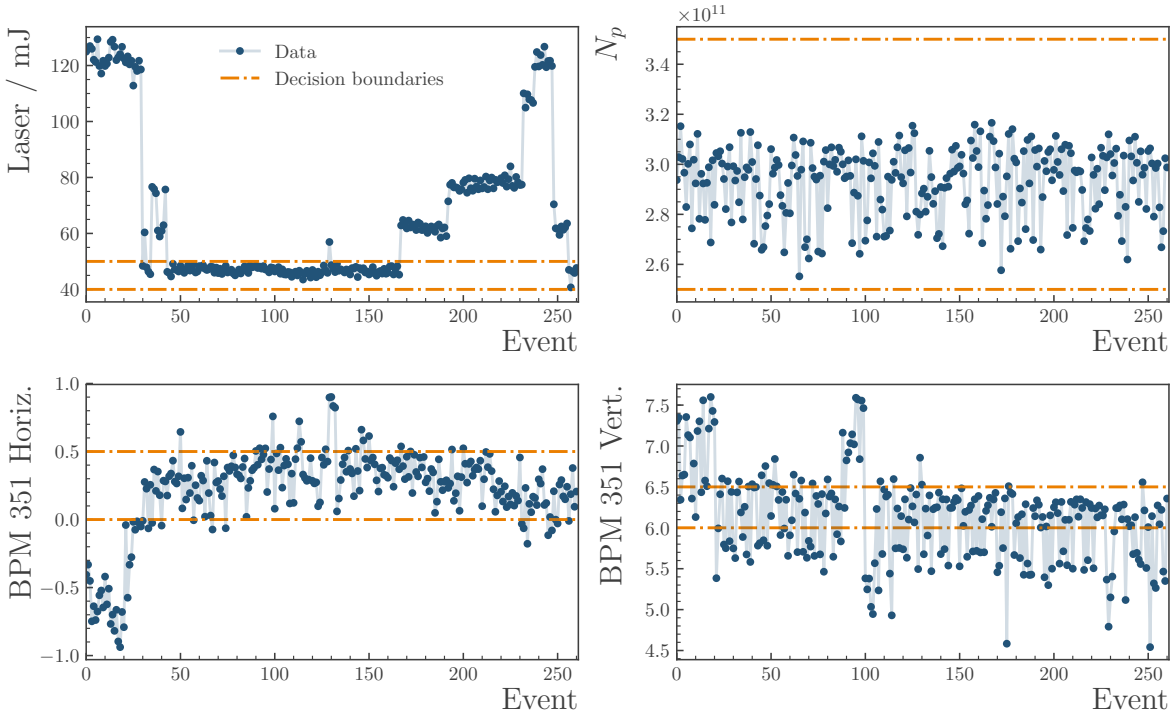

(b) $3.9 \times 10^{14}\,\mathrm{cm}^{-3}$

Figure 6.15.: Events and cuts for the gradient scans. The cuts are specified in Table 6.1. The events between all the decision boundaries are accepted. Only electron acceleration events with a charge more than 5 fC are shown.

Parameter	$1.8 \times 10^{14}\,\mathrm{cm}^{-3}$	$3.9 \times 10^{14}\,\mathrm{cm}^{-3}$	$6.6 \times 10^{14}\,\mathrm{cm}^{-3}$
Laser pulse energy / mJ	$[110, 120]$	$[40, 50]$	$[55, 65]$
$Q_{\mathcal{P}}$ / fC	> 5	> 5	> 5
N_p / 10^{11}	$[2.5, 3.5]$	$[2.5, 3.5]$	$[2.5, 3.5]$
BPM 351 Horiz.	$[-0.9, -0.7]$	$[0.0, 0.5]$	$[-0.5, 0.0]$
BPM 351 Vert.	$[6.5, 6.7]$	$[6.0, 6.5]$	$[6.2, 6.5]$

Table 6.1.: Cuts for the density gradient datasets.

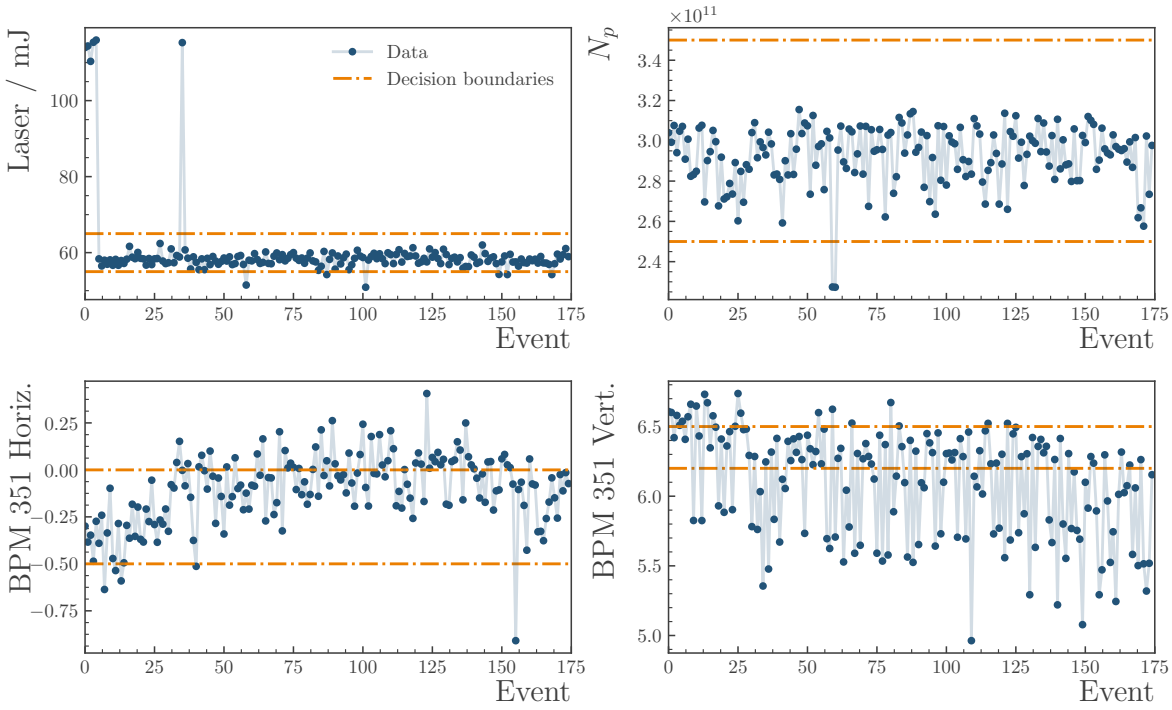

(c) $6.6 \times 10^{14}\,\mathrm{cm}^{-3}$

Figure 6.15.: Events and cuts for the gradient scans (continued). The cuts are specified in Table 6.1. The events between all the decision boundaries are accepted. Only electron acceleration events with a charge more than 5 fC are shown.

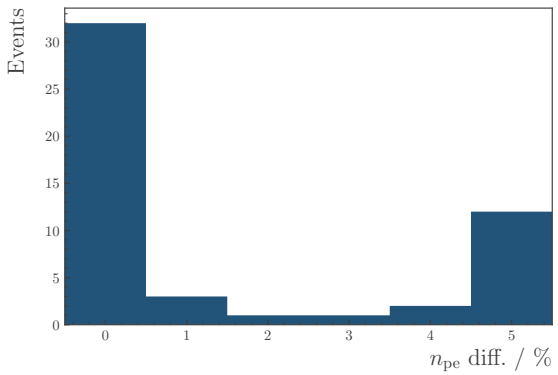

(a) $1.8 \times 10^{14}\,\mathrm{cm}^{-3}$

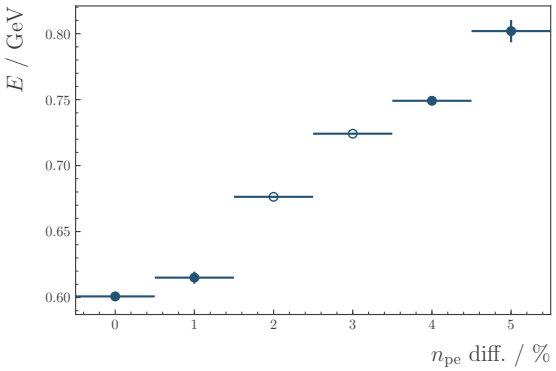

(b) $1.8 \times 10^{14}\,\mathrm{cm}^{-3}$

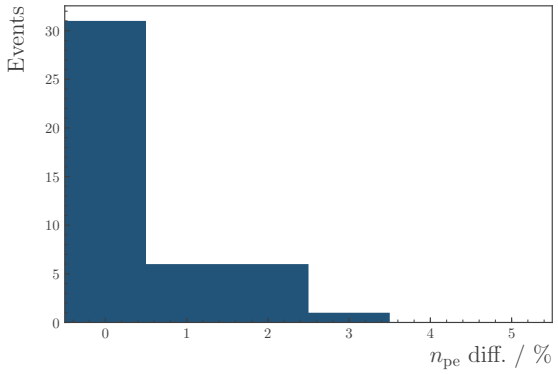

(c) $3.9 \times 10^{14}\,\mathrm{cm}^{-3}$

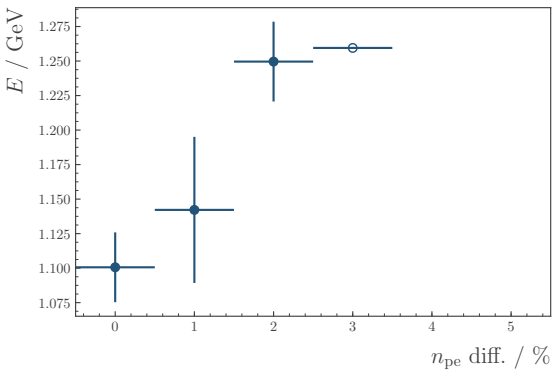

(d) $3.9 \times 10^{14}\,\mathrm{cm}^{-3}$

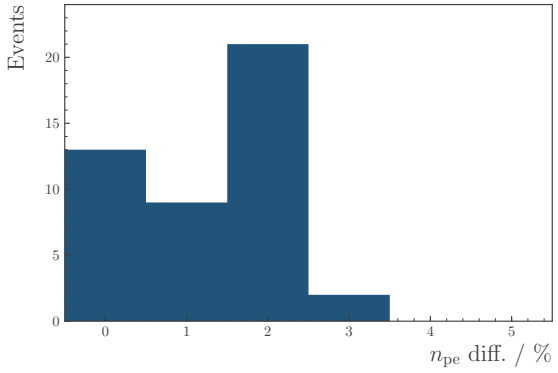

(e) $6.6 \times 10^{14}\,\mathrm{cm}^{-3}$

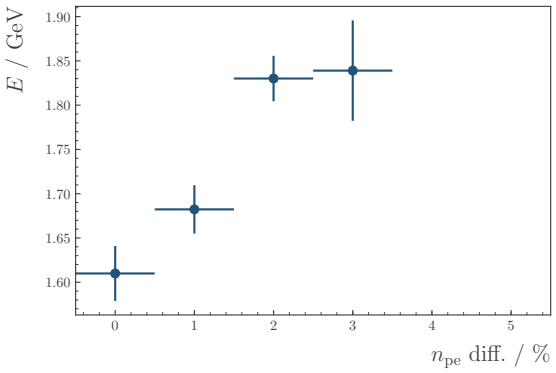

(f) $6.6 \times 10^{14}\,\mathrm{cm}^{-3}$

Figure 6.16.: Analysis results for energy against density gradient. The data are binned by density gradient with the mean energy shown. The number of events in each bin are shown in the histograms on the left. In the energy plot the vertical error bar indicates the error on the mean and the horizontal error bar indicates the width of the density gradient bin. Events with a single event in the bin are indicated with an empty marker. The small numbers of events are due to the slow extraction rate of the experiment and data cuts which flatten the bins in other variables such as laser energy.

Chapter 7.

Future colliders

A number of proposals exist for high energy physics experiments using proton-driven plasma wakefield acceleration [98]. The most ambitious proposal is the very high energy electron-proton collider (VHEeP) [99], which collides a 7 TeV LHC proton beam with a 3 TeV electron beam produced by a plasma wakefield driven by the counter-circulating LHC beam, resulting in a centre-of-mass energy of approximately 9 TeV. This unique collider proposal is the focus of this chapter. In Section 7.1 a brief introduction to deep inelastic scattering will be presented. Following this, the kinematics of the final state at VHEeP will be reviewed and from this a first proposal for the detector location will be given in Section 7.2. Finally, the hitherto unsolved problem of separating the accelerated electrons from their proton drive beam without incurring excessive energy loss through synchrotron radiation will be considered.

7.1. Deep inelastic scattering

At centre-of-mass energies significantly above m_p, the proton can break apart during $e^- p^+$ scattering. This is referred to as deep inelastic scattering (DIS), an example of which is shown in the Feynman diagram in Figure 7.1. An incoming electron of momentum k^μ scatters off a proton of momentum P^μ through the t-channel exchange of a photon, with a momentum transfer $q^\mu = k^\mu - k'^\mu$. In the lab frame, the outgoing electron has an angle θ_e relative to the incoming proton (such that $\theta_e = 0$ is backward scattering). These two quantities are related by

$$q^2 = -2k \cdot k' = -4E_e E'_e \cos^2 \frac{\theta_e}{2} \,, \tag{7.1}$$

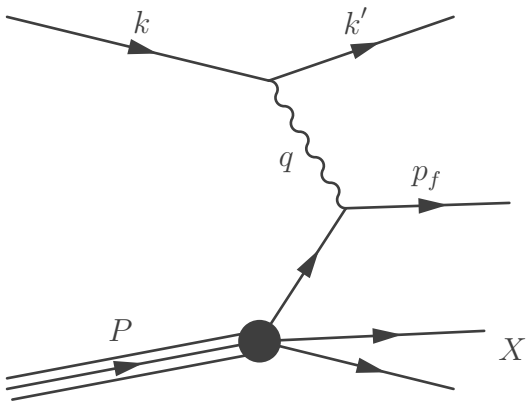

Figure 7.1.: An example of a Feynman diagram for DIS, showing an electron of momentum k^μ scattering off a proton of momentum P^μ and generating a multibody final state containing the scattered electron (k'^μ) the struck quark (p_f^μ) and the rest of the hadronic final state (X).

where E_e and E'_e are the electron's initial and final energies, respectively and the relativistic limit $m_p = 0$, $m_e = 0$ has been taken. The energy scale of the collision is $Q \equiv \sqrt{-q^2}$ and this may be used to define the dimensionless quantity

$$x \equiv \frac{Q^2}{2P \cdot q}\,, \tag{7.2}$$

which is known as Bjorken x. Consider the struck parton (in Figure 7.1 a quark) within the proton of initial momentum p_i^μ and final momentum p_f^μ such that momentum conservation gives $p_i^\mu + q^\mu = p_f^\mu$. Squaring both sides gives

$$m_q^2 + 2p_i \cdot q + q^2 = m_q^2\,, \tag{7.3}$$

where m_q is the parton's mass. This leads to

$$\frac{Q^2}{2p_i \cdot q} = 1\,. \tag{7.4}$$

This is equal to Eq. (7.2) if $p_i^\mu = xP^\mu$, therefore x can be interpreted as the fraction of the proton's momentum carried by the struck parton. The final DIS variable commonly defined [100] is

$$y = \frac{P \cdot q}{P \cdot k}\,, \tag{7.5}$$

which is known as the inelasticity of the event and may be interpreted as the fraction of energy transferred from the electron to the proton in the proton's rest frame. The

square of the centre-of-mass energy $s = (k + P)^2$ relates these DIS variables by

$$Q^2 = sxy\,. \tag{7.6}$$

Historically, the development of DIS and the development of quantum chromodynamics (QCD) have been intrinsically linked [101]. Mysteries about the substructure of the proton and the fundamental nature of QCD persist [102] and a very high energy DIS collider is one promising way of exploring them.

7.2. VHEeP

A simple representation of VHEeP is shown in Figure 7.2. The proposed beam line for proton extraction uses the $\sim 16\,\mathrm{T}$ magnets under investigation for FCC-hh [103]. Recalling Eq. (3.13), a 16 T magnet would bend the 7 TeV protons along a path with a radius of approximately 1.5 km. The diameter of the LHC is approximately 8.5 km and simulations have shown that a plasma wakefield driven by an LHC proton beam could accelerate witness electrons to 3 TeV in 4 km [104]. There would, therefore, be approximately 1.5 km remaining for beam optics and detectors.

A key appeal of the VHEeP physics programme is the ability to probe DIS at lower values of x than other proposed experiments of the same nature [105, 106]. At $Q^2 = 1\,\mathrm{GeV}^2$ this value is $x \sim 10^{-8}$. In this regime the energy dependence of the hadronic cross sections, which are currently poorly understood, may be measured. A cross section of particular interest is the total photon–proton cross section which, at fixed Q^2, rises with the photon–proton centre-of-mass energy $W = \sqrt{(q + P)^2}$ [107] and is related to the total DIS cross section by the equivalent photon approximation [108–110]. This rising cross section combined with the uniquely high energy reach of the VHEeP proposal goes some way towards mitigating the present luminosity limitations of collider experiments based on proton-driven plasma wakefield acceleration.

A specific example of a cross section which rises with W is that of vector meson production. In this process, the proton contributes two gluons to produce the meson and its rising cross section is explained by the rise in the proton's gluon density at low x (for fixed Q^2). The large E_e at VHEeP allows threshold production of vector mesons such as the J/ψ at much lower values of x than is possible at other DIS collider proposals. Extrapolations in W of the currently measured J/ψ production cross section $\sigma_{J/\psi}$ show

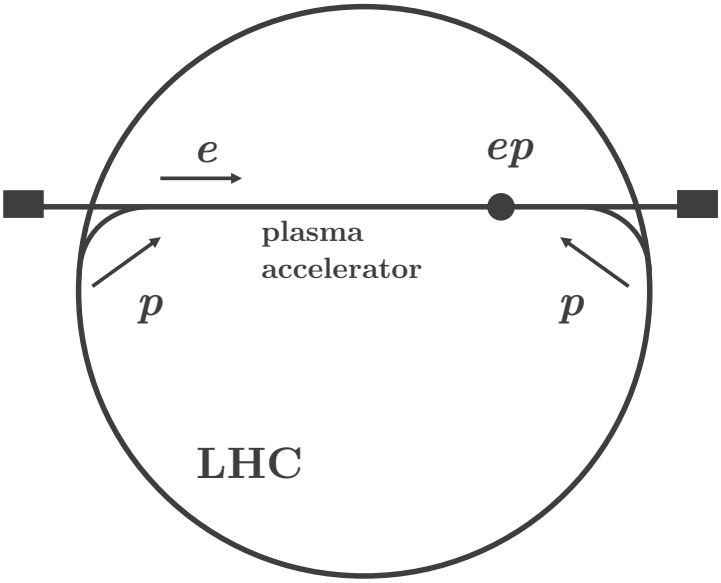

Figure 7.2.: The VHEeP collider. A proton beam is extracted from the LHC and injected into a plasma accelerator, driving a wakefield which accelerates a witness electron bunch to high energy. The counter circulating LHC beam is extracted and collides with this electron bunch. Each proton beam would likely need to be dumped afterwards.

an apparently nonsensical result at, or near, the W reach of the VHEeP collider: $\sigma_{J/\psi}$ overtaking σ_ϕ and σ_ω, the production cross sections of two lighter vector mesons [111].

The rise in $\sigma_{J/\psi}$ and the total photon–proton cross section may be moderated by the saturation of the gluon density. A number of proposed mechanisms exist which may explain this saturation [112]. A conceptually straight forward example is that below some energy scale, gluon recombination grows and matches the soft gluon emission which is responsible for driving up the gluon density at low x. Gluon saturation is a topic of interest in heavy ion collisions [113], cosmic ray physics [114] and as a testing ground for new theoretical approaches [115]. As such, it is a topic of considerable importance and one which VHEeP would be uniquely positioned to contribute to experimentally. The detection of low x events at VHEeP is, therefore, critical to its success and is the subject of much of the remainder of this section.

7.2.1. Leptonic final state

The measurement of the final state electron is central to a DIS experiment. The electron–hydrogren scattering experiments at SLAC, which first indicated the existence of partons,

measured only the electron final state [1] and from this deduced a significant amount of information about the structure of the proton and the nature of QCD.

The nature of this final state can understood using the DIS variables. Eq. (7.5) may be directly evaluated as

$$y = \frac{P \cdot q}{P \cdot k} = 1 - \frac{P \cdot k'}{P \cdot k} = \frac{E_e - E'_e \sin^2 \frac{\theta_e}{2}}{E_e} , \tag{7.7}$$

and y may also be reexpressed using Eq. (7.1) and Eq. (7.6) as

$$y = \frac{Q^2}{sx} = \frac{E'_e \cos^2 \frac{\theta_e}{2}}{xE_p} . \tag{7.8}$$

These may be combined to give

$$\sin^2 \frac{\theta_e}{2} = \frac{E_e E'_e - xE_p E_e}{E_e E'_e - xE_p E'_e} , \tag{7.9}$$

and

$$E'_e = \frac{xE_p E_e}{E_e \cos^2 \frac{\theta_e}{2} + xE_p \sin^2 \frac{\theta_e}{2}} . \tag{7.10}$$

Both of which may be substituted back into Eq. (7.7) to give

$$y = \frac{E_e - E'_e}{E_e - xE_p} , \tag{7.11}$$

$$y = \frac{E_e}{E_e + x \tan^2 \frac{\theta_e}{2}} . \tag{7.12}$$

Substituting for y in Eq. (7.6) this gives

$$Q^2(x, E'_e) = sx \frac{E_e - E'_e}{E_e - xE_p} , \tag{7.13}$$

$$Q^2(x, \theta_e) = sx \frac{E_e}{E_e + x \tan^2 \frac{\theta_e}{2}} . \tag{7.14}$$

which define isolines of constant E'_e and θ_e, respectively, in the (x, Q^2) plane.

7.2.2. Hadronic final state

The hadronic final state consists of the struck parton and the proton remnant. For now, the kinematics of the proton remnant will be ignored. By conservation of momentum $k^\mu + xP^\mu = k'^\mu + p_f^\mu$, which directly gives

$$xE_p + E_e = E'_e + E_h \,, \tag{7.15}$$

where E_h is the final state energy of the struck parton. In analogy with Eq. (7.10), some manipulation shows that

$$E_h = \frac{xE_pE_e}{E_e \cos^2 \frac{\gamma_h}{2} + xE_p \sin^2 \frac{\gamma_h}{2}} \,, \tag{7.16}$$

where γ_h is the lab frame angle between the final state of the struck parton and the incoming proton beam. Substituting in Eq. (7.13) gives

$$Q^2(x, E_h) = sx\frac{xE_p - E_h}{xE_p - E_e} \,, \tag{7.17}$$

$$Q^2(x, \gamma_h) = sx\frac{xE_p}{xE_p + E_e \cot^2 \frac{\gamma_h}{2}} \,. \tag{7.18}$$

These are the hadronic equivalents of the electron's isolines.

7.2.3. The VHEeP final state

The colliding electrons and protons at VHEeP have energies of 3 TeV and 7 TeV respectively. The solutions to Eq. (7.13) for various electron angles of interest are shown in Figure 7.3. The majority of the phase space in the region of interest (low x) has final state electrons at angles very close to π, that is, forward scattering. For reference, the full angular reach of the ATLAS detector [116] including the barrel, end-cap and forward calorimeters, is shown in Figure 7.3a. The full reach is up to $|\eta| = 4.9$ where the pseudorapidity η is defined as

$$\eta \equiv -\log\left(\tan\frac{\theta}{2}\right) \,, \tag{7.19}$$

with θ defined relative to the incoming protons. Figure 7.4 and Figure 7.5 show the energy of the scattered electron and parton. At very low x Eq. (7.15) simplifies to

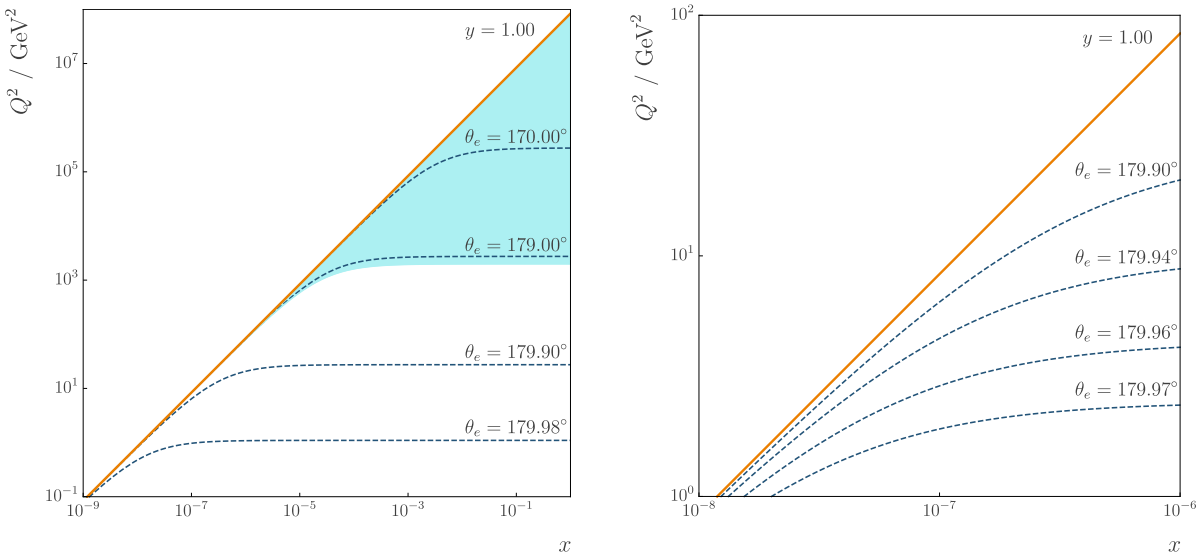

(a) **(b)**

Figure 7.3.: Kinematics of the final state electrons at VHEeP. Isolines of constant electron angle are shown. The full angular reach of the ATLAS detector (up to $|\eta| = 4.9$) is shaded in light blue.

$E_e \simeq E'_e + E_h$. This may be seen by comparing Figure 7.4b and Figure 7.5b. The angle of the final state of the scattered parton is shown in Figure 7.6, again with the angular reach of the ATLAS detector highlighted. Clearly, a standard detector will not provide sufficient coverage at very forward angles to diagnose the low x interactions.

Moving the detector downstream of the interaction is one way to extend the reach to large values of $|\eta|$. Consider the external diameter of the VHEeP beampipe to be 53 mm (the same as the LHC [5]), a scattered electron with $\theta_e = 179.97°$ would exit this approximately 50 m downstream of the interaction region. Consider a forward detector placed 100 m downstream of the interaction with an inner radius of 26.5 mm and an outer radius of 3 m. Figure 7.7 shows the region of the (x, Q^2) plane where this detector could measure both the scattered electron and the scattered parton's final state. This reach of this detector encompasses both hard DIS processes with $Q^2 \sim 10^3\,\text{GeV}^2$ and softer processes with $x \sim 10^{-8}$ and $Q^2 \sim m_p^2$. Additional detector regions may be needed to study the remainder of the hadronic remnant (which will largely be scattered in the opposite direction) or search for specific processes at low η such as leptoquark production[1] [99]. It is likely, however, that a very forward detector such as this will be required to measure the scattered electron and its associated parton jet.

[1] Given VHEeP's proposed luminosity, the viability of this search is debatable.

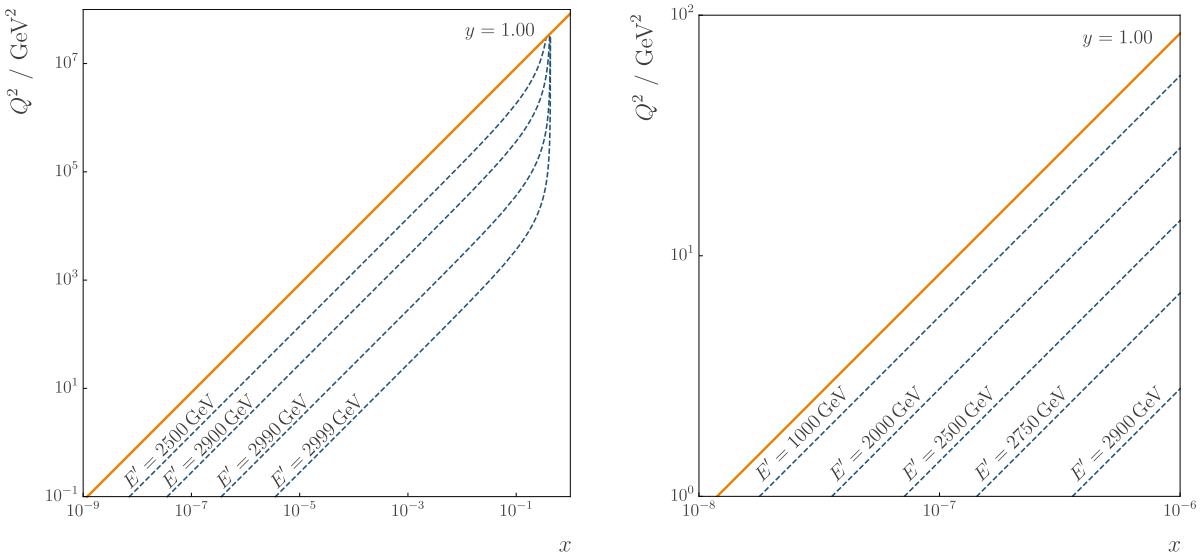

(a) **(b)**

Figure 7.4.: Kinematics of the final state electrons at VHEeP. Isolines of constant electron energy are shown.

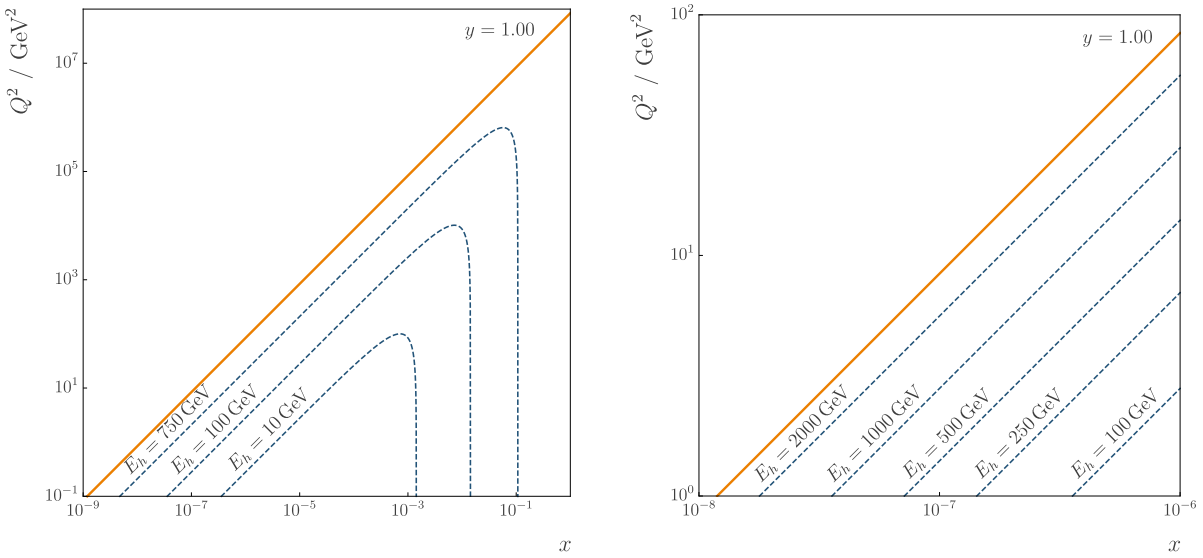

(a) **(b)**

Figure 7.5.: Kinematics of the final state parton. Isolines of constant hadronic energy are shown.

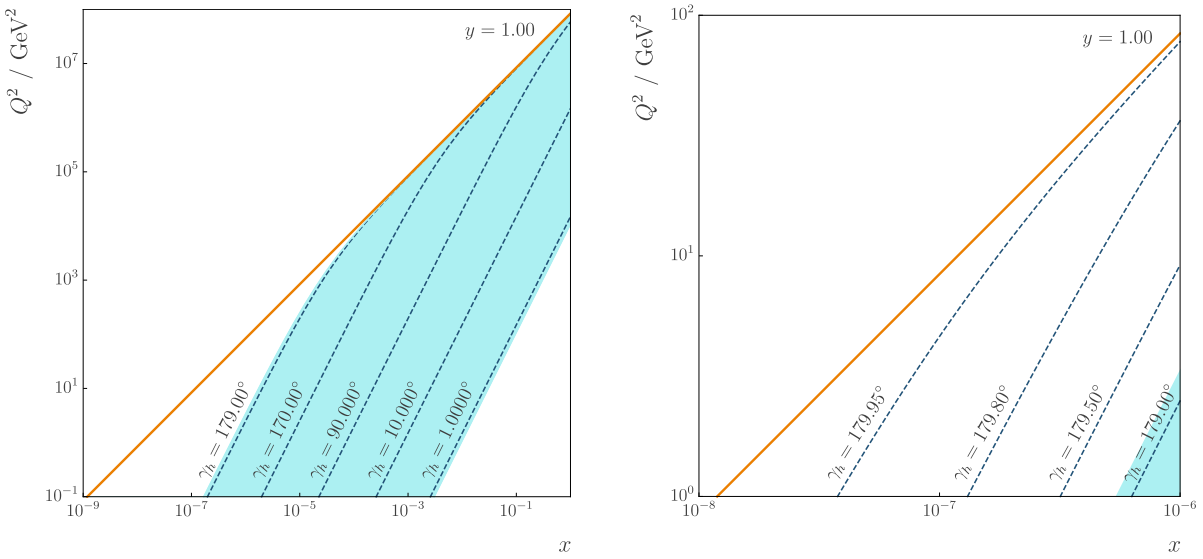

Figure 7.6.: Kinematics of the final state parton. Isolines of constant hadronic angle are shown. The full angular reach of the ATLAS detector (up to $|\eta| = 4.9$) is shaded in light blue.

7.2.4. Beam separation

The problem of separating the accelerated electron beam from the proton beam driving the plasma wakefield is relevant to all proton-driven plasma wakefield experiments. Beam separation of VHEeP is particularly challenging due to the very high energy of the electrons. When charged particles are accelerated they emit synchrotron radiation [17]. This emission is much greater for acceleration in the transverse direction than the longitudinal. The radiated power of the synchrotron radiation due to a magnetic field deflecting a singly charged particle of energy E along a trajectory or radius ρ is given by

$$P_\gamma = \frac{c\, C_\gamma}{2\pi} \frac{E^4}{\rho^2} \,, \tag{7.20}$$

where c is the speed of light in a vacuum and C_γ is a constant which, for electrons, is equal to $8.85 \times 10^{-5}\,\mathrm{m\,GeV^{-3}}$. Recall Eq. (3.13):

$$\rho = \frac{\beta E}{eB} \,. \tag{7.21}$$

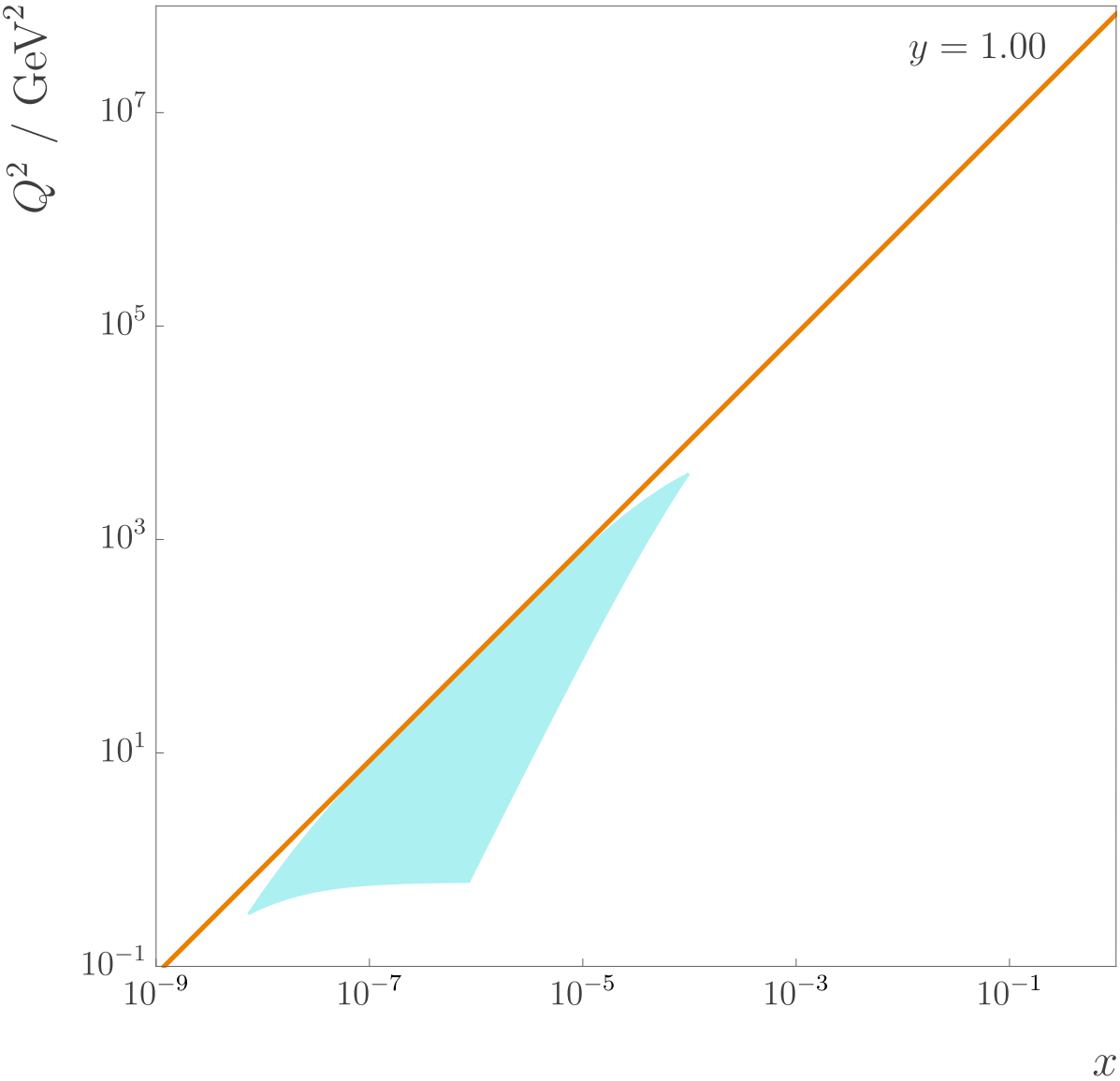

Figure 7.7.: Region of coverage for a proposed detector. The front plane detector is 100 m downstream of the interaction point, with an internal radius of 26.5 mm and an external radius 3 m. The shaded region shows where both the scattered electron and the final state of the scattered parton would be measured by the detector.

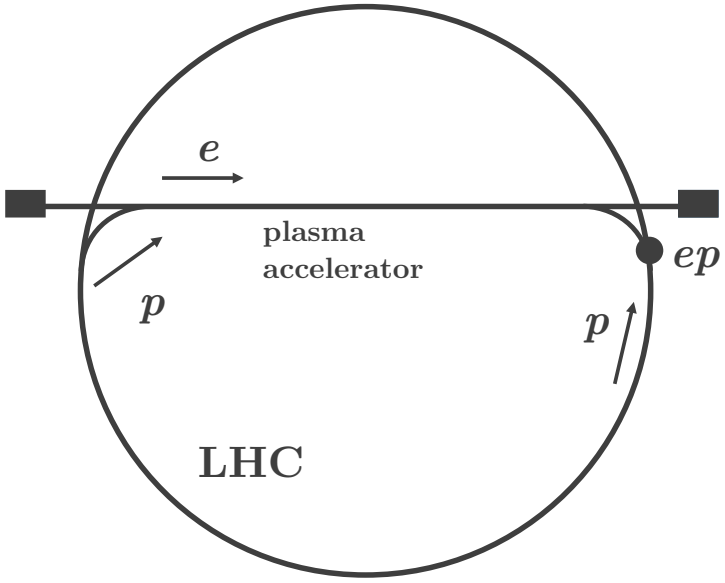

Figure 7.8.: A straw man proposal for separating the electron and proton beams at VHEeP.

Suppose that the electrons are bent along a path of constant ρ, emitting synchrotron radiation as they go. Then Eq. (7.20) may be solved as

$$-\frac{dE}{dt} = \frac{c\,C_\gamma}{2\pi\rho^2}E^4\,, \tag{7.22}$$

$$\Longrightarrow \quad E(t) = \frac{E_e}{\left(\frac{3c\,C_\gamma}{2\pi\rho^2}E_e^3 t + 1\right)^{\frac{1}{3}}}\,, \tag{7.23}$$

where $E_e = E(0)$ is the electron's initial energy.

Consider the proposal for beam separation at VHEeP shown in Figure 7.8, where the electrons, rather than the protons, are bent through $\pi/2$ of the 1.5 km radius ring discussed in Section 7.2. Figure 7.9a shows the energy of the 3 TeV electrons as they are bent through this turn and Figure 7.9b shows the magnetic field required to bend the electrons along this path. Clearly, this is not an appropriate solution, since the electrons lose approximately 90% of their energy. The main accomplishment of this proposal would be the creation of 40 GeV photons[2].

The separation of the beams need not be very large. For example, separating the beams by 50 mm, such that they could be contained within separate beam pipes, would likely be more than sufficient to ensure a clean collision environment. Let the fractional

[2]From the critical photon energy [17], $\varepsilon_c = \frac{3\hbar c}{2\left(m_e c^2\right)^3}\frac{E^3}{\rho}$.

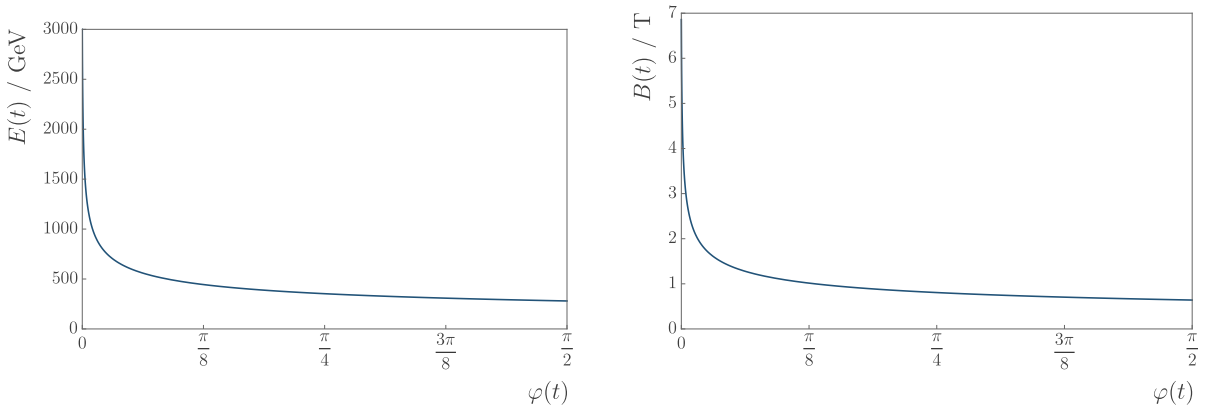

(a) **(b)**

Figure 7.9.: The effect of bending the electrons as shown in Figure 7.8. The 3 TeV electrons are bent through an angle φ around a circlular beamline with a radius of 1.5 km. The energy of the electrons and the magnetic field required to keep them on the trajectory are shown.

energy loss of the electrons be

$$F(t) = \frac{E_e - E(t)}{E_e} \,. \tag{7.24}$$

For this loss to be small $\frac{3cC_\gamma}{2\pi\rho^2}E_e^3 t \ll 1$, so F may be expanded to first order around 0 as

$$F(t) \simeq \frac{c\,C_\gamma E_e^3}{2\pi\rho^2} t \,. \tag{7.25}$$

Recall the results of Section 3.2 and consider the electron and proton beams propagating through a dipole of length L. For small energy loss, the bending radius in this magnet may be assumed to be constant, therefore at the exit of the dipole F may be appoximated by

$$F \simeq \frac{C_\gamma E_e^3}{2\pi\rho}\varphi = \frac{C_\gamma E_e^3}{2\pi\rho} \arcsin\frac{L}{\rho} \,, \tag{7.26}$$

where φ is the angle through which the electrons have been bent. For small φ values

$$F \simeq \frac{C_\gamma E_e^3 L}{2\pi\rho^2} = \frac{C_\gamma e^2 B^2 E_e L}{2\pi} \,, \tag{7.27}$$

given the assumption that $\beta \simeq 1$. Thus, for a given magnetic field strength, the maximum length of dipole that the electrons can propagate through without losing more than a

fraction F of their energy is

$$L \simeq \frac{2\pi F}{C_\gamma e^2 B^2 E_e} \,. \tag{7.28}$$

For a 1 T magnet and a fractional loss of 10^{-4} this length is 0.26 m. As the protons and electrons propagate through this dipole they will be bent in opposite directions and their separation at the end of the dipole will be given by

$$w = \rho_e - \sqrt{\rho_e^2 - L^2} + \rho_p - \sqrt{\rho_p^2 - L^2} \,, \tag{7.29}$$

where $\rho_{e,p}$ are the bending radii of the electrons and protons. A distance z downstream of the end of the dipole the separation will be

$$\begin{aligned} S(z) &= w + z\left(\tan\varphi_e + \tan\varphi_p\right) \,, \\ &= w + zL\left(\frac{1}{\sqrt{\rho_e^2 - L^2}} + \frac{1}{\sqrt{\rho_p^2 - L^2}}\right) \,. \end{aligned} \tag{7.30}$$

Inverting this, a given separation can be achieved over a total distance

$$z + L = \frac{S - \rho_e\left(1 - \dfrac{\rho_e}{\sqrt{\rho_e^2 - L^2}}\right) - \rho_p\left(1 - \dfrac{\rho_p}{\sqrt{\rho_p^2 - L^2}}\right)}{\dfrac{L}{\sqrt{\rho_e^2 - L^2}} + \dfrac{L}{\sqrt{\rho_p^2 - L^2}}} \,. \tag{7.31}$$

The distance required to separate the two beams by 50 mm for three different values of F is plotted against the magnetic field strength in Figure 7.10a and the corresponding magnetic length is shown in Figure 7.10b. With the 0.26 m, 1 T magnet considered above this distance is 13.3 km for $F = 10^{-4}$; an impractically long beamline. Finding the minima of Eq. (7.31) with respect to B sets a lower limit on the distance required to separate the beams.

Eq. (7.31) is difficult to differentiate and solve directly but for $\rho_{e,p}^2 \gg L^2$, as is necessary to keep F small, it may be approximated by

$$z + L \simeq \frac{L}{2} + \frac{S}{L}\frac{\rho_e \rho_p}{\rho_e + \rho_p} \equiv Z \,. \tag{7.32}$$

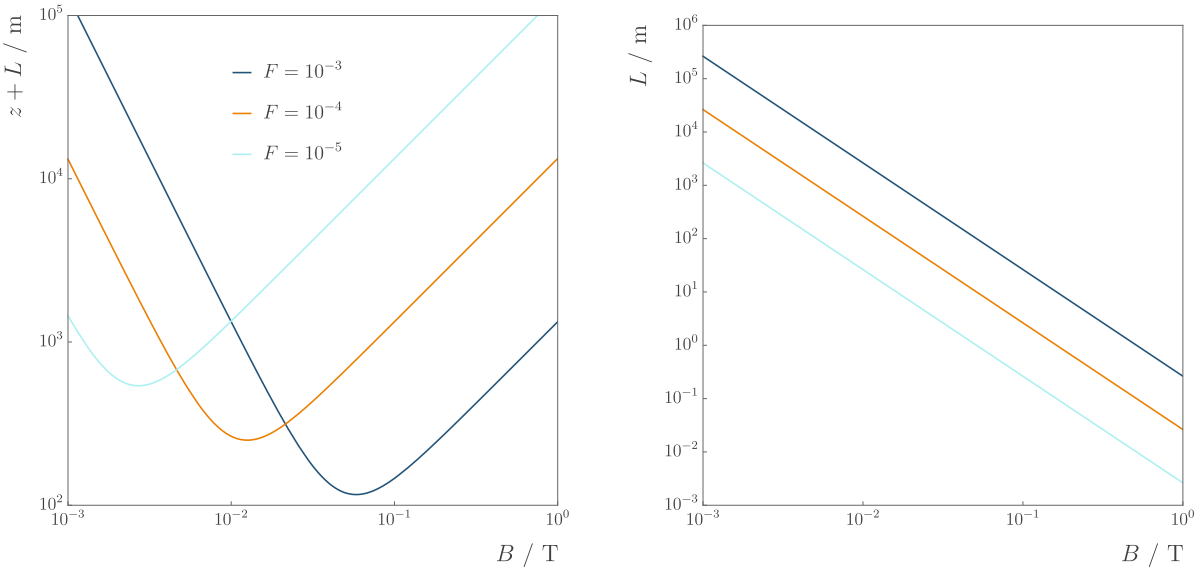

(a) **(b)**

Figure 7.10.: The distance and magnetic length required to separate the electron and proton beams by 50 mm as a function of field strength, for a variety of fractional energy losses.

Now $\rho_{e,p}$ and L may be substituted to give

$$Z = \frac{\pi F}{C_\gamma e^2 B^2 E_e} + \frac{C_\gamma e B E_e^2 E_p S}{2\pi F (E_e + E_p)} \,, \tag{7.33}$$

which has a minima at

$$-\frac{2\pi F}{C_\gamma e^2 B^3 E_e} + \frac{C_\gamma e E_e^2 E_p S}{2\pi F (E_e + E_p)} = 0 \,, \tag{7.34}$$

$$\implies \quad B_0 = \left(\frac{4\pi^2 F^2 \left(E_e + E_p\right)}{C_\gamma^2 e^3 E_e^3 E_p S} \right)^{\frac{1}{3}} \,. \tag{7.35}$$

Leading to

$$Z_0 \equiv Z(B_0) = \frac{3}{2} \left(\frac{C_\gamma E_e^3 E_p^2 S^2}{2\pi F \left(E_e + E_p\right)^2} \right)^{\frac{1}{3}} = \frac{3}{2} L(B_0) \,. \tag{7.36}$$

That is, L is always 2/3 of Z when Z is minimised. Figure 7.11a shows this value of B for three different values of F as a function of the beam separation and Figure 7.11b shows the corresponding minimum distance. For $F = 10^{-4}$ and $S = 50\,\text{mm}$ the minimum

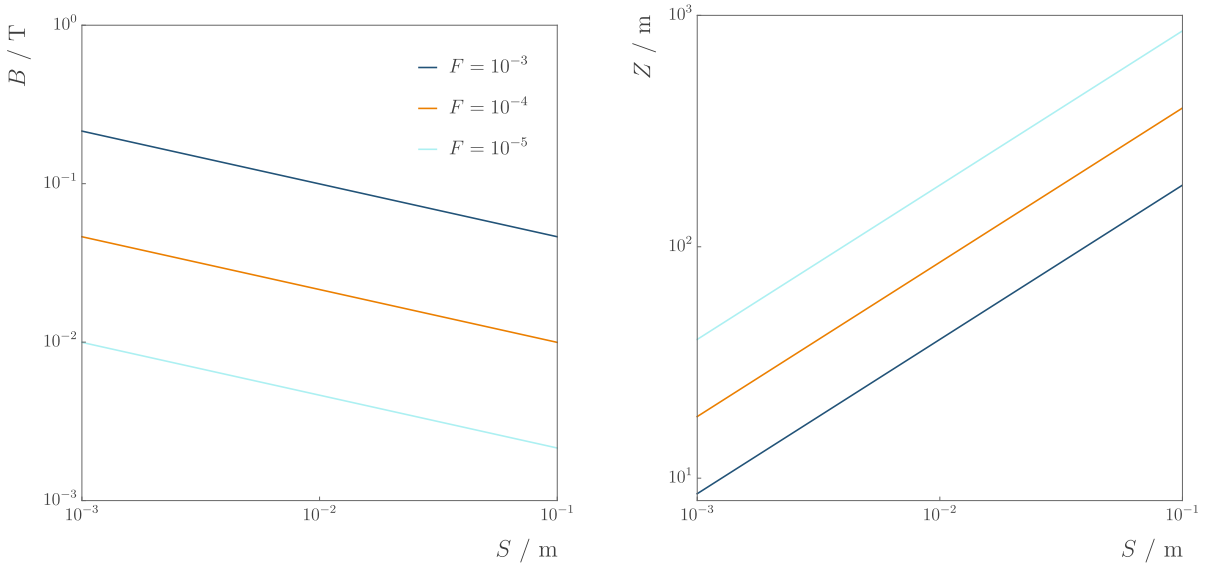

(a) **(b)**

Figure 7.11.: The minimum distance Z_0 and corresponding magnetic field strength B_0 required to separate the two beams by S while maintaining a fractional energy loss higher than F.

length is 250.5 m, of which 167 m is magnets with a 0.0126 T field. This is an approximate solution, assuming one long single strength dipole, and therefore only sets the minimum distance rather being a real beam line design. What it does show, however, is that separation of the beams is very likely to be possible within the space available at VHEeP. Even if a more realistic design for the beam line were to be 500 m long rather than 250 m, this would still be acceptable.

Chapter 8.

Conclusion

8.1. Summary

The uncertain future of collider physics is due, in part, to the cost associated with building accelerators at the energy frontier. Reducing the scale of these projects is motivated by both historic [117] and contemporary [118] events. Furthermore, exceeding the TeV scale at a lepton collider based on radio frequency cavities is, in the author's opinion, implausible. To change this, a novel technology will need to employed and proton-driven plasma wakefield acceleration was conceived for this exact purpose. The work presented in this thesis has centred around a major milestone in the development of this technique: the first acceleration of electrons in the plasma wakefield of a proton bunch.

This milestone has been achieved at AWAKE, a proof-of-principle experiment using 400 GeV proton bunches from CERN's SPS to drive a wakefield in a 10 m column of ionised rubidium. The first results from AWAKE established self-modulation of the SPS proton bunch, a prerequisite for electron acceleration to high energy.

The acceleration was verified using a magnetic spectrometer, installed downstream of the plasma. The unique radiation environment of the AWAKE area necessitated a complex design, with the components of the spectrometer spanning three tunnels. The dispersion caused by the spectrometer's dipole at various settings has been characterised to produce the position–energy conversion functions which underpin the electron energy measurement. The scintillator providing the electron acceleration signal has been calibrated at an electron beam line to determine its charge response. The necessary conversion factors to translate these results back to the AWAKE experimental setup have been determined.

The spectrometer's multicomponent optical line has been installed and aligned to image the scintillator. The resolution of these images has been characterised by a series of measurements, verifying that the percent-level energy resolution specified in the spectrometer's design has been achieved. The necessary correction factors required to provide a true determination of the accelerated electron bunch charge have been determined. A thorough characterisation of the backgrounds present in the spectrometer's measurements has been carried out and effective methods for subtracting these backgrounds have been proposed and verified.

At a plasma density of $1.8 \times 10^{14}\,\mathrm{cm}^{-3}$, the acceleration of picocoulomb bunches to 800 MeV has been demonstrated. The stability of acceleration at this density has been proven with an acceleration peak observed consistently over several hours of running. Increased energy gain at higher plasma densities and in the presence of plasma density gradients has been shown, with acceleration to $2.0 \pm 0.1\,\mathrm{GeV}$ achieved close to the AWAKE baseline density with a gradient set.

A highly ambitious collider proposal, VHEeP, has been discussed. The final state kinematics have been considered and the location of a very forward detector has been proposed. The novel problem of separating a highly energetic electron beam from its proton drive beam without incurring significant radiative energy loss has been presented. An analytic formula has been derived which, for a given energy loss, provides the minimum possible distance over which this separation can occur.

8.2. Reflections

The success of the spectrometer in detecting and diagnosing accelerated electron bunches does not grant the work presented in this thesis immunity from some *ex post facto* criticism and it is appropriate to reflect on where things could have been done better given more time, more resources or with clearer thinking.

The calibration of the spectrometer's scintillator, discussed in Chapter 5, presented a significant challenge. In particular, the translation of the results from CLEAR to AWAKE was a complicated multi-step process as evidenced by the many factors present in Eq. (5.5). A far better solution, had it been available, would have been to install a removable charge measuring device, such as a Faraday cup, at the external face of the scintillator at AWAKE. The injection electron beam could be propagated through the

beamline and imaged a large number of times using the spectrometer optical system. A significant number of charge readings could also be taken (though likely not concurrently as the charge measuring device would block the optical path) providing an *in situ* measurement of the scintillator's charge response, likely with a smaller uncertainty. With appropriate adjustment of the spectrometer's dipole an experimental confirmation of the validity of Eq. (5.2) would also have been possible by scanning the injection electrons across the scintillator's surface. Indeed this would provide a direct measurement of the quantity $\mathcal{VA}$ used in Eq. (6.11) without relying on the results of the vignetting scan discussed in Section 5.3.2. This scan would have been possible with a change in the dipole magnet's power supply which is presently limited at the low end to 18 A but would need to reach down to approximately 1 A.

A deeper understanding of the spectrometer's fire window and its effect on the results of Section 5.3 would also be beneficial. In particular, since the precise cause of the window's deleterious effect on the resolution, particularly in the vertical axis, is unknown, a dedicated set of measurements to determine this would be required before a solution could be implemented. One possible way to do this would be to employ a setup similar to that described in Section 5.1, with a laser mounted on a microrotation stage at the surface of the scintillator. By scanning the laser spot over the surface of the window in each axis and measuring the change in the spot's profile, a better understanding of the window's optical properties could be reached. This would be a way to test the hypothesis that the window's narrower vertical dimension contributes to it affecting the vertical resolution more significantly. Ideally, of course, the fire window would not be a necessary part of the optical line and this would in principle have been possible if the entire spectrometer darkroom, including the window's protective housing, had been fire rated to the same specification as the wall. A significant cost increase was associated with this option.

A comparison between densities of the effects of plasma density gradients would have been possible in Section 6.2.3 if more care had been taken at the time to provide uniform parameters to the electron beam and the ionising laser pulse. Given the beam time constraints on the experiment, however, a more systematic approach such as this may have meant missing out on a headline result, such as the maximum energy of 2.0 ± 0.1 GeV.

8.3. Future work

Establishing electron acceleration is a very early step on the road to producing a collider based on proton-driven plasma wakefield acceleration. A key priority in the short term is fruther analysis of the AWAKE data to understand the process of acceleration. While broadly in line with the predictions of simulations, the AWAKE acceleration results published thus far have not undergone rigorous comparison to theory. Furthermore, a systematic scan over only a single parameter (the plasma density gradient) has been presented at this point and this analysis was seriously affected by a lack of consistent data. Optimising acceleration at AWAKE requires an understanding of how each parameter affects the electrons.

The results of the AWAKE data analysis will have considerable influence on AWAKE run 2, the design of which is already underway. Run 2 aims to bridge the gap between proof-of-principle experiment and operational machine. The run 2 spectrometer will need be able to detect electrons up to 10 GeV with excellent energy resolution. This may involve the use of a second dipole magnet. Measurements of the emittance of the accelerated bunch in both transverse axes will be crucial to prove the viability of proton-driven plasma wakefield acceleration.

Even if AWAKE run 2 proves that reliable production of a stable, high energy, high charge, low emittance electron bunch is possible, a major hurdle remains: repetition rate. The VHEeP proposal relies on the increasing photon–proton cross section at high energy and low x to mitigate the luminosity limitations brought about by this. Novel experimental proposals based on very high energy but low luminosity beams should be actively pursued and schemes to increase the technology's repetition rate must be devised.

Appendix A.

Electron trajectories

If the magnetic field is confined to some area which does not cover the entire circular path of the electrons then at some time t_e the electrons will exit the magnetic field. Once the electron exits the field there is no force acting upon it

$$\vec{F} = \gamma m_e \frac{d\vec{v}}{dt} = 0 \,, \tag{A.1}$$

and thus

$$v_x(t) = k_x \,, \tag{A.2}$$
$$v_z(t) = k_z \,, \tag{A.3}$$

where $k_{x,z}$ are constants and

$$x(t) = k_x t + c_x \,, \tag{A.4}$$
$$z(t) = k_z t + c_z \,, \tag{A.5}$$

where $c_{x,z}$ are also constants. This can be rearranged to give

$$x(t) = \frac{k_x}{k_z} z(t) + c_x + \frac{k_x}{k_z} c_z \,, \tag{A.6}$$

that is, the electrons follow a straight line at a constant velocity, as expected of a particle with no force acting upon it. The constants can be determined by the condition that the positions must match Eq. (7.2) and Eq. (3.11) and velocities must match Eq. (3.8) and

Eq. (3.7) at t_e, thus

$$k_x = v_x(t_e) = v_x(t_e) = \rho \sin\left(\frac{vt_e}{\rho}\right) , \tag{A.7}$$

$$k_z = v_z(t_e) = v_z(t_e) = \rho \cos\left(\frac{vt_e}{\rho}\right) , \tag{A.8}$$

$$c_x = x(t_e) - k_x t_e = x(t_e) - k_x t_e = \rho\left(1 - \cos\left(\frac{vt_e}{\rho}\right) - \sin\left(\frac{vt_e}{\rho}\right) t_e\right) , \tag{A.9}$$

$$c_z = z(t_e) - k_z t_e = z(t_e) - k_z t_e = \rho\left(\sin\left(\frac{vt_e}{\rho}\right) - \cos\left(\frac{vt_e}{\rho}\right) t_e\right) . \tag{A.10}$$

With these, Eq. (A.6) becomes

$$x(t) = \tan\left(\frac{vt_e}{\rho}\right) z(t) + \rho\left(1 - \sec\left(\frac{vt_e}{\rho}\right)\right) . \tag{A.11}$$

Let the tangent to the circle at t_e be $T(t)$. This is given by

$$T(t) = \left.\frac{dz}{dx}\right|_{t_e} z(t) + C(t_e) . \tag{A.12}$$

The gradient of the circle Eq. (3.12) is

$$\frac{dz}{dx} = \frac{\frac{dz}{dt}}{\frac{dx}{dt}} = \tan\left(\frac{vt}{\rho}\right) , \tag{A.13}$$

and the constant term is given by

$$\begin{aligned} C(t_e) &= \rho - \sqrt{\rho^2 - z^2(t_e)} - \tan\left(\frac{vt}{\rho}\right) z(t_e) , \\ &= \rho - \sqrt{\rho^2 - \rho^2 \sin^2\left(\frac{vt_e}{\rho}\right)} - \rho \tan\left(\frac{vt_e}{\rho}\right) \sin\left(\frac{vt_e}{\rho}\right) , \\ &= \rho\left(1 - \sec\left(\frac{vt_e}{\rho}\right)\right) . \end{aligned} \tag{A.14}$$

Therefore

$$T(t) = \tan\left(\frac{vt_e}{\rho}\right) z(t) + \rho\left(1 - \sec\left(\frac{vt_e}{\rho}\right)\right) , \tag{A.15}$$

which is the same as Eq. (A.11). Thus, after leaving the magnetic field the electrons move at a constant velocity following a straight line which is the tangent to the circle at the exit point.

Colophon

This thesis was made in LaTeX 2_ε using the "hepthesis" class [119].

Bibliography

[1] M. D. Schwartz, *Quantum Field Theory and the Standard Model* (Cambridge University Press, Cambridge, 2014).

[2] Particle Data Group, M. Tanabashi *et al.*, Phys. Rev. **D98**, 030001 (2018).

[3] CMS Collaboration, G. Aad *et al.*, Phys. Lett. **B716**, 1 (2012).

[4] ATLAS Collaboration, S. Chatrchyan *et al.*, Phys. Lett. **B716**, 30 (2012).

[5] L. Evans and P. Bryant, J. Instrum. **3**, S08001 (2008).

[6] CMS Collaboration, A. Sirunyan *et al.*, Phys. Lett. **B779**, 283 (2018).

[7] ATLAS Collaboration, M. Aaboud *et al.*, Phys. Rev. **D99**, 072001 (2019).

[8] CMS Collaboration, A. M. Sirunyan *et al.*, Phys. Rev. Lett. **120**, 231801 (2018).

[9] ATLAS Collaboration, M. Aaboud *et al.*, Phys. Lett. **B784**, 173 (2018).

[10] CMS Collaboration, A. M. Sirunyan *et al.*, Phys. Rev. Lett. **121**, 121801 (2018).

[11] ATLAS Collaboration, M. Aaboud *et al.*, Phys. Lett. **B786**, 59 (2018).

[12] G. Apollinari *et al.*, CERN Report No. CERN-2017-007-M, 2017 (unpublished).

[13] M. Mangano *et al.*, CERN Report No. CERN-ACC-2018-0056, 2018 (unpublished), Submitted for publication to Eur. Phys. J. C.

[14] CEPC Study Group, IHEP Report No. IHEP-CEPC-DR-2018-01, 2018 (unpublished), arXiv:1809.00285.

[15] T. Behnke *et al.*, CERN Report No. CERN-ATS-2013-037, 2013 (unpublished), arXiv:1306.6327.

[16] M. Aicheler *et al.*, CERN Report No. CERN-2012-007, 2012 (unpublished).

[17] H. Wiedemann, *Particle Accelerator Physics*, 3rd ed. (Springer, Heidelberg, 2007).

[18] A. Hassanein *et al.*, Phys. Rev. ST Accel. Beams **9**, 062001 (2006).

[19] A. D. Cahill, J. B. Rosenzweig, V. A. Dolgashev, S. G. Tantawi, and S. Weathersby, Phys. Rev. Accel. Beams **21**, 102002 (2018).

[20] F. Wang, C. Adolphsen, and C. Nantista, Phys. Rev. ST Accel. Beams **14**, 010401 (2011).

[21] V. I. Veksler, Coherent Principle Of Acceleration Of Charged Particles, in *Proc. 1st International Conference on High-Energy Accelerators*, pp. 80–83, 1956.

[22] T. Tajima and J. M. Dawson, Phys. Rev. Lett. **43**, 267 (1979).

[23] C. Joshi, T. Tajima, J. Dawson, H. Baldis, and N. Ebrahim, Phys. Rev. Lett. **47**, 1285 (1981).

[24] Y. Kitagawa *et al.*, Phys. Rev. Lett. **68**, 48 (1992).

[25] K. Nakajima *et al.*, AIP Conference Proceedings **335**, 145 (1995).

[26] S. P. D. Mangles *et al.*, Nature **431**, 535 (2004).

[27] C. G. R. Geddes *et al.*, Nature **431**, 538 (2004).

[28] J. Faure *et al.*, Nature **431**, 541 (2004).

[29] R. D. Ruth, A. W. Chao, P. L. Morton, and P. B. Wilson, Part. Accel. **17**, 171 (1985).

[30] P. Chen, J. M. Dawson, R. W. Huff, and T. Katsouleas, Phys. Rev. Lett. **54**, 693 (1985).

[31] I. Blumenfeld *et al.*, Nature **445**, 741 (2007).

[32] J. M. Dawson, Phys. Rev. **113**, 383 (1959).

[33] J. B. Rosenzweig, Phys. Rev. **A38**, 3634 (1988).

[34] B. Cros and P. Muggli, (2017), http://cds.cern.ch/record/2298632.

[35] M. J. Hogan, Rev. Acc. Sci. Tech. **09**, 63 (2016).

[36] C. B. Schroeder, E. Esarey, C. G. R. Geddes, C. Benedetti, and W. P. Leemans, Phys. Rev. ST Accel. Beams **13**, 101301 (2010).

[37] S. Steinke *et al.*, Nature **530**, 190 (2016).

[38] A. Caldwell, K. Lotov, A. Pukhov, and F. Simon, Nature Physics **5**, 363 (2009).

[39] G. Xia and A. Caldwell, Producing Short Proton Bunch for Driving Plasma Wakefield Acceleration, in *Proc., 1st International Particle Accelerator Conference*, pp. 4395–4397, 2010.

[40] N. Kumar, A. Pukhov, and K. Lotov, Phys. Rev. Lett. **104**, 255003 (2010).

[41] A. Pukhov *et al.*, Phys. Rev. Lett. **107**, 145003 (2011).

[42] E. Esarey, J. Krall, and P. Sprangle, Phys. Rev. Lett. **72**, 2887 (1994).

[43] D. Whittum, Phys. Plasmas **4**, 1154 (1997).

[44] J. Krall and G. Joyce, Phys. Plasmas **2**, 1326 (1995).

[45] C. Siemon, V. Khudik, S. Austin Yi, A. Pukhov, and G. Shvets, Physics of Plasmas **20**, 103111 (2013).

[46] J. Vieira, Y. Fang, W. B. Mori, L. O. Silva, and P. Muggli, Phys. Plasmas **19**, 063105 (2012).

[47] J. Vieira, W. B. Mori, and P. Muggli, Phys. Rev. Lett. **112**, 205001 (2014).

[48] E. Mobs, CERN Report No. OPEN-PHO-ACCEL-2018-005, 2018 (unpublished), http://cds.cern.ch/record/2636343.

[49] F. Galleazzi, private communication, 2017.

[50] AWAKE Collaboration, P. Muggli *et al.*, Plasma Phys. Control. Fusion **60**, 014046 (2017).

[51] AWAKE Collaboration, E. Gschwendtner *et al.*, Nucl. Instrum. Methods **A829**, 76 (2016), 2nd European Advanced Accelerator Concepts Workshop (EAAC2015).

[52] AWAKE Collaboration, A. Caldwell *et al.*, Nucl. Instrum. Methods **A829**, 3 (2016), 2nd European Advanced Accelerator Concepts Workshop (EAAC2015).

[53] V. Fedosseev *et al.*, Integration of a Terawatt Laser at the CERN SPS Beam for the AWAKE Experiment on Proton-Driven Plasma Wake Acceleration, in *Proc. 7th International Particle Accelerator Conference*, pp. 2592–2595, 2016.

[54] K. Pepitone *et al.*, Nucl. Instrum. Methods **A909**, 102 (2018), 3rd European Advanced Accelerator Concepts Workshop (EAAC2017).

[55] O. Mete Apsimon, S. Döbert, C. Welsch, and G. Xia, Review of Emittance Diagnostics for Space Charge Dominated Beams for AWAKE e^- Injector, in *Proc. 7th International Particle Accelerator Conference*, pp. 337–339, 2016.

[56] E. Öz and P. Muggli, Nucl. Instrum. Methods **A740**, 197 (2014), 1st European Advanced Accelerator Concepts Workshop (EAAC2013).

[57] J. Vieira, R. A. Fonseca, W. B. Mori, and L. O. Silva, Phys. Rev. Lett. **109**, 145005 (2012), arXiv:1208.3242.

[58] F. Batsch *et al.*, Nucl. Instrum. Methods **A909**, 359 (2018), 3rd European Advanced Accelerator Concepts Workshop (EAAC2017).

[59] A. Petrenko, K. Lotov, and A. Sosedkin, Nucl. Instrum. Methods **A829**, 63 (2016), 2nd European Advanced Accelerator Concepts Workshop (EAAC2015).

[60] AWAKE Collaboration, A. Caldwell *et al.*, CERN Report No. CERN-SPSC-2013-013. SPSC-TDR-003, 2013 (unpublished).

[61] AWAKE Collaboration, E. Adli *et al.*, Phys. Rev. Lett. **122**, 054802 (2019).

[62] AWAKE Collaboration, M. Turner *et al.*, Phys. Rev. Lett. **122**, 054801 (2019).

[63] K. Rieger, A. Caldwell, O. Reimann, R. Tarkeshian, and P. Muggli, Rev. Sci. Instrum. **88**, 025110 (2017).

[64] A. Campillo and S. Shapiro, IEEE J. Quantum Electron. **19**, 585 (1983).

[65] V. L. Ginzburg and I. M. Frank, J. Phys. (USSR) **9**, 353 (1945).

[66] M. Turner *et al.*, Nucl. Instrum. Methods **A854**, 100 (2017).

[67] AWAKE Collaboration, E. Adli *et al.*, Nature **561**, 363 (2018).

[68] L. Nevay *et al.*, (2018), arXiv:1808.10745.

[69] P. Dewitte, private communication, 2017.

[70] G. Cowan, *Statistical Data Analysis* (Clarendon, Oxford, 1998).

[71] J. Bauche, private communication, 2017.

[72] A. Vorozhtsov, private communication, 2017.

[73] L. Deacon, private communication, 2015.

[74] A. Petrenko, private communication, 2017.

[75] J. Chappell, private communication, 2018.

[76] N. Chritin, Spectrometer vacuum chamber and window, SPSVCW___0082, https://edms.cern.ch/document/1702386, 2016.

[77] C. Capelli, Spectrometer vacuum window, SPSVWW___0019, https://edms.cern.ch/document/1720798, 2016.

[78] Mitsubishi Chemical, *X-ray Scintillator Screen—DRZ*^{TM}, 2017, https://www.m-chemical.co.jp/en/products/departments/mcc/ledmat/product/1201037_7550.html.

[79] MCI Optonix, *DRZ Screens*, 2017, http://www.mcio.com/Products/drz-screens.aspx.

[80] S. Mazzoni and L. Deacon, private communication, 2016.

[81] P. La Penna and M. Quattri, private communication, 2017.

[82] T. Schneider, private communication, 2019.

[83] C. Capelli, Mirror support—Bosch Structure, SPSXAHBA0029, https://edms.cern.ch/document/1807982, 2017.

[84] C. Capelli, Mirror support 1, SPSXAHBA0011, https://edms.cern.ch/document/1808284, 2017.

[85] C. Capelli, Mirror support 2, SPSXAHBA0019, https://edms.cern.ch/document/1808029, 2017.

[86] P. La Penna, private communication, 2019.

[87] M. Arruat *et al.*, Front-end software architecture, in *ICALEPCS* Vol. 7, p. 310, 2007.

[88] I. Gorgisyan, private communication, 2017.

[89] E. Hecht, *Optics*, 5th ed. (Pearson Education Limited, Harlow, 2017).

[90] L. Deacon *et al.*, Development of a spectrometer for proton driven plasma wakefield accelerated electrons at awake, in *Proc. 6th International Particle Accelerator Conference*, pp. 2601–2604, 2015.

[91] Y. Glinec *et al.*, Rev. Sci. Instrum. **77**, 103301 (2006).

[92] L. Jensen, private communication, 2019.

[93] D. Gamba *et al.*, Nucl. Instrum. Methods **A909**, 480 (2018), 3rd European Advanced Accelerator Concepts Workshop (EAAC2017).

[94] C. A. Lindstrøm *et al.*, Phys. Rev. Lett. **122**, 129901 (2019).

[95] I. Fujieda *et al.*, IEEE Trans. Nucl. Sci. **38**, 255 (1991).

[96] E. Adli *et al.*, CERN Report No. CERN-SPSC-2011-020. SPSC-I-240, 2011 (unpublished), https://cds.cern.ch/record/1357313.

[97] J. Orear, Am. J. Phys. **50**, 912 (1982).

[98] A. Caldwell *et al.*, (2018), arXiv:1812.11164.

[99] A. Caldwell and M. Wing, Eur. Phys. J. **C76**, 463 (2016), arXiv:1606.00783.

[100] R. K. Ellis, W. J. Stirling, and B. R. Webber, *QCD and Collider Physics* (Cambridge University Press, Cambridge, 1996).

[101] A. De Rujula, J. R. Ellis, R. Petronzio, G. Preparata, and W. Scott, Can one tell QCD from a hole in the ground?, in *Proc. 17th International School of Subnuclear Physics: Pointlike Structures Inside and Outside Hadrons*, pp. 567–673, 1979.

[102] I. Abt *et al.*, Phys. Rev. **D96**, 014001 (2017).

[103] M. Benedikt *et al.*, CERN Report No. CERN-ACC-2018-0058, 2018 (unpublished), http://cds.cern.ch/record/2651300, Submitted for publication to Eur. Phys. J. ST.

[104] A. Caldwell and K. V. Lotov, Phys. Plasmas **18**, 103101 (2011).

[105] A. Accardi *et al.*, Eur. Phys. J. **A52**, 268 (2016), arXiv:1212.1701.

[106] LHeC Study Group, J. L. Abelleira Fernandez *et al.*, J. Phys. **G39**, 075001 (2012), arXiv:1206.2913.

[107] ZEUS Collaboration, J. Breitweg *et al.*, Phys. Lett. **B407**, 432 (1997).

[108] C. F. v. Weizsäcker, Z. Phys. **88**, 612 (1934).

[109] E. J. Williams, Phys. Rev. **45**, 729 (1934).

[110] V. N. Gribov, V. M. Shekhter, V. A. Kolkunov, and L. B. Okun, Sov. Phys. JETP **14**, 1308 (1962).

[111] L. Favart, M. Guidal, T. Horn, and P. Kroll, Eur. Phys. J. **A52**, 158 (2016), arXiv:1511.04535.

[112] E. Sichtermann, Nucl. Phys. **956**, 233 (2016), The XXV International Conference on Ultrarelativistic Nucleus-Nucleus Collisions: Quark Matter 2015.

[113] J. L. Albacete and C. Marquet, Prog. Part. Nucl. Phys. **76**, 1 (2014), arXiv:1401.4866.

[114] L. Portugal and T. Kodama, Nucl. Phys. **A837**, 1 (2010), arXiv:0910.3701.

[115] E. Iancu, Nucl. Phys. **A854**, 18 (2011), arXiv:1009.1278.

[116] ATLAS Collaboration, G. Aad *et al.*, J. Instrum. **3**, S08003 (2008).

[117] M. Riordan, Phys. Perspect. **2**, 411 (2000).

[118] E. Gibney, Nature News (2019), https://www.nature.com/articles/d41586-019-00824-4.

[119] A. Buckley, The hepthesis LaTeX class.